



Hao, Danni (2018) Hybridisation of plasmonic and acoustic biosensing devices. PhD thesis.

<http://theses.gla.ac.uk/8992/>

Copyright and moral rights for this work are retained by the author

A copy can be downloaded for personal non-commercial research or study, without prior permission or charge

This work cannot be reproduced or quoted extensively from without first obtaining permission in writing from the author

The content must not be changed in any way or sold commercially in any format or medium without the formal permission of the author

When referring to this work, full bibliographic details including the author, title, awarding institution and date of the thesis must be given

Enlighten:Theses  
<http://theses.gla.ac.uk/>  
theses@gla.ac.uk



University  
of Glasgow

# Hybridisation of Plasmonic and Acoustic Biosensing Devices

**Danni Hao**

A Thesis submitted to

School of Engineering

University of Glasgow

in fulfilment of the requirements for the degree of

*Doctor of Philosophy*

Sep 2017

# Abstract

Monolithically integrating multiple sensing technologies shows a great potential to perform quantitative measurements for multiple biomarkers of diseases and also provide more insight towards one single biochemical event. The localised surface plasmon resonance spectroscopy measures the change in the refractive index arising from the molecular adsorption on the metallic nanostructures. Acoustic sensors, such as surface acoustic wave sensor and quartz crystal microbalance, measure the variation of its mechanical oscillation caused by the sum of the deposited molecules and the solvent coupled to the adsorbed molecules. Both techniques are known independently as having applications in *in-situ*, label-free sensing and analysis of biological binding reactions. Due to their complementary properties, the integration of both can prove to be a valuable tool for studying biomolecules on sensing surface.

This thesis reports on the development of a hybrid biosensing device that integrates localised surface plasmonic sensing and acoustic sensing technologies. Gold nanodisk arrays as localised surface plasmon resonance sensing device was studied in visible region using three substrates: borosilicate glass, lithium niobate and quartz. The design, simulation, fabrication and characterisation of the gold nanodisk arrays, and the sensing performance optimisation were investigated using glass substrate. Lithium niobate, as a piezoelectric material has surface acoustic wave compatibility and this study can pave the way towards the development of hybrid sensing devices. The study on lithium niobate demonstrated the feasibility of a localised surface plasmon resonance device utilising a high refractive index, birefringent and piezoelectric substrate.

Using quartz as the substrate, the design and fabrication of a hybrid sensor were performed, which integrated localised surface plasmonic resonance into a quartz crystal microbalance for studying biochemical surface binding reactions. The coupling of localised plasmon resonance nanostructures and a quartz crystal microbalance allows optical spectra and quartz crystal microbalance resonant frequency shifts to be recorded simultaneously, and analysed in real time for a given surface adsorption process. This integration has the potential to be miniaturised for application in point-of-care diagnostics.

# Declaration

Unless otherwise acknowledged, the content of this thesis is the result of my own work. None of this material has been submitted for any other degree at the University of Glasgow or any other institution.

Danni Hao

# Acknowledgement

First and foremost, I would like to thank my supervisor Prof. David Cumming. He has been a constant source of inspiration and enthusiasm toward the research. His insightful guidance and continuous support ensured a successful completion of my studies.

Special thanks to Iain McCrindle and Kirsty Rew for their help and guidance at the start of my PhD. I would like to thank them for introducing me to plasmonics and for assisting with my initial clean room training.

I would also like to thank James Grant, his insightful guidance has been invaluable during my PhD. Thanks also go to Abdul Shakoor, Mitchell Guy Kenney, Nadia Pinton and Yash Diptesh Shah for all the helpful discussions we had about plasmonics. Thanks to Stephen Thoms, Kevin Docherty and Iain MacGilp for their assistance and discussions on fabrication.

A special acknowledgement goes to Andrew Glidle, Boon Chong Cheah, Chunxiao Hu for their helpful advices, in particular for their suggestions on the biology experiments. I would like to extend my thanks to all the members of the Microsystem Technology Group. It had been a great pleasure working with you all. I really appreciate your generous help.

I would also like to thank my friends and all the people who has encouraged me during the past 4 years. Thanks to Chengzhi Xie, Jie Ding, and all my lunch buddies for making my life more fun and joyful.

My sincere gratitude also goes to all the staff in the James Watt Nanofabrication Centre. Without their dedications in operating and maintaining the facilities, my research would have been impossible to be completed.

I would also like to acknowledge China scholarship Council for the financial support to my studies.

Finally, I cannot be more grateful for the support from my mum Zhiqin Li and my dad Jianxin Hao. Their continuing love, support and patience has been and will always be the energy and courage that take me forward. I love you two forever!

# Publications

## Journal Papers

**D. Hao**, C. Hu, J. Grant, A. Glidle, and D. R. S. Cumming, "Hybrid localized surface plasmon resonance and quartz crystal microbalance sensor for label free biosensing," *Biosens. Bioelectron.*, vol. 100, no. August 2017, pp. 23–27, Feb. 2018.

**D. Hao**, M. G. Kenney, and D. R. S. Cumming, "Plasmonic gold nanodiscs using piezoelectric substrate birefringence for liquid sensing," *Appl. Phys. Lett.*, vol. 108, no. 25, p. 251601, Jun. 2016.

Y. D. Shah, J. Grant, **D. Hao**, M. Kenney, V. Pusino, and D. R. S. Cumming, "Ultra-narrow Line Width Polarization-Insensitive Filter Using a Symmetry-Breaking Selective Plasmonic Metasurface," *ACS Photonics*, vol. 5, no. 2, pp. 663–669, Feb. 2018.

A. Shakoor, B. C. Cheah, **D. Hao**, M. Al-Rawhani, B. Nagy, J. Grant, C. Dale, N. Keegan, C. McNeil, and D. R. S. Cumming, "Plasmonic Sensor Monolithically Integrated with a CMOS Photodiode," *ACS Photonics*, vol. 3, no. 10, pp. 1926–1933, Oct. 2016.

## Conference Paper

A. Shakoor, B. C. Cheah, **D. Hao**, M. Al-Rawhani, B. Nagy, J. Grant, C. Dale, N. Keegan, C. McNeil, and D. R. S. Cumming, "Monolithic integration of a plasmonic sensor with CMOS technology," in *Proceedings of SPIE - The International Society for Optical Engineering*, 2017, vol. 10107, p. 101070F.

# Contents

Abstract .....	I
Declaration.....	II
Acknowledgement.....	III
Publications.....	IV
Contents .....	V
List of Figures .....	IX
List of Tables.....	XVII
List of Acronyms.....	XVIII
1. Introduction .....	1
1.1 Motivation.....	1
1.2 Aims and Objectives.....	2
1.3 Thesis Outline.....	3
2. Background.....	5
2.1 Light Interaction with Nanoscale Metal Features .....	5
2.1.1 Plasmonics .....	5
2.1.1 Electromagnetics and Dielectric Properties of Metals .....	5
2.1.2 Surface Plasmon Resonance .....	9
2.1.3 Localised Surface Plasmon Resonance.....	12
2.1.3.1 Mie Theory.....	15
2.1.3.1 Background Theory of LSPR Sensing .....	16
2.1.4 Extraordinary Optical Transmission.....	18
2.2 Acoustic Wave Devices .....	20
2.2.1 Acoustic and Piezoelectricity .....	20
2.2.2 Bulk Acoustic Wave and Quartz Crystal Microbalance.....	21
2.2.2.1 Bulk Acoustic Wave.....	22
2.2.2.2 Quartz Crystal Microbalance .....	22

2.2.2.3	QCM working and sensing principle.....	23
2.2.3	Surface Acoustic Wave.....	26
2.3	Biosensing.....	29
2.3.1	Acoustic Biosensing.....	31
2.3.1.1	QCM Biosensor .....	31
2.3.1.2	Surface Acoustic Wave Biosensor.....	33
2.3.2	Optical Sensing.....	34
2.3.2.1	SPR Biosensors .....	34
2.3.2.2	LSPR Biosensors.....	35
2.3.2.3	SPR vs LSPR Measurement Methods.....	36
2.4	Hybridisation of Optical and Acoustic Sensing .....	37
2.5	Summary .....	40
3.	Methods.....	41
3.1	Finite-Difference Time-Domain.....	41
3.1.1	Lumerical FDTD Solutions .....	44
3.2	Micro/nanofabrication.....	46
3.2.1	Metallisation .....	46
3.2.2	Lithography .....	47
3.2.2.1	Photolithography .....	47
3.2.2.2	Electron Beam Lithography.....	49
3.2.3	Lift-off.....	53
3.2.4	Annealing.....	54
3.3	Chemical and Biological Modification of Sensor Surface .....	55
3.4	Spectral Characterisation.....	57
3.5	QCM Characterisation.....	58
3.5.1	VNA Characterisation.....	58
3.5.2	PCB Design for QCM Frequency Measurement.....	59
3.6	Summary .....	62
4.	Localised Surface Plasmon Resonance from Gold Nanodisks on SiO <sub>2</sub> for Biosensing .....	63

4.1	Introduction .....	63
4.1.1	Design and Simulation .....	63
4.1.2	Fabrication .....	67
4.1.2.1	Reducing the Ebeam Time .....	68
4.1.3	Post Fabrication Annealing .....	70
4.1.4	Characterisation Results and Discussion.....	70
4.1.4.1	Effect of the Post Fabrication Annealing .....	71
4.1.4.1	Effect of Array Period ( $P$ ) on the LSPR.....	72
4.1.4.2	Effect of Nanodisk Diameter ( $d$ ) on the Resonance.....	74
4.1.5	Glycerine-Water Solution for Sensitive Calibration.....	78
4.2	Gold Nanodisk Arrays as Biosensor Based on LSPR.....	83
4.3	Summary .....	86
5.	LSPR Sensor on $\text{LiNbO}_3$ .....	87
5.1	Introduction .....	87
5.2	Design and Simulation .....	88
5.3	Fabrication .....	92
5.4	Results and Discussion.....	94
5.4.1	Effect of the Substrate Refractive Index on Resonance.....	94
5.4.2	Effect of Polarisation on the Resonances .....	97
5.4.3	Optimised Structure for Higher Sensitivity .....	100
5.5	Summary .....	102
6.	Hybrid QCM and LSPR Sensor for Label Free Biosensing .....	103
6.1	Introduction .....	103
6.2	QCM Design .....	104
6.3	LSPR Design .....	106
6.4	Fabrication .....	107
6.5	Setup for the Simultaneous Recording .....	109
6.6	Results and Discussion.....	112
6.7	Summary .....	117
7.	Conclusions and Future Work .....	118
7.1	LSPR Biosensor on $\text{SiO}_2$ .....	118

7.2	LSPR Nanodisks on LiNbO <sub>3</sub> .....	119
7.3	Hybrid LSPR and QCM Biosensor .....	120
7.4	Future Work.....	121
	Bibliography .....	123
	Appendix .....	138

# List of Figures

Figure 2.1 Illustration of a surface plasmon (SP) propagating at a metal-dielectric interface. (a) A schematic of a SP propagating in the x direction with electric and magnetic field components shown. (b) Evanescent decay of the field component that is perpendicular to the interface into both the metal and the dielectric [16].....	10
Figure 2.2 Illustrations of the different methods by which incident light can couple with surface plasmons (SP) for SPR generation [18] (a) Grating coupling, (b) prism coupling – Kretschmann configuration and (c) waveguide coupling. ....	11
Figure 2.3 The Lycurgus cup [25] .....	12
Figure 2.4 Schematic of a plasmon oscillation for a metallic sphere, showing the displacement of the electron cloud, positive charge and the fixed atomic nuclei.....	14
Figure 2.5 Setups to measure LSPR spectra. (a) Transmission and (b) reflectance geometries for measuring extinction spectra of nanoparticle arrays. (c) Dark-field scattering experimental setup using a high-numerical aperture dark-field condenser and a high-numerical aperture microscope objective for measuring single-nanoparticle scattering spectra. [29].....	14
Figure 2.6 Illustration of the metal NP used for biosensing. The metal NP is in the center. The blue region is the exponentially decaying electromagnetic field. The purple region is the adsorption layer. The yellow region is the external environment.....	17
Figure 2.7 Different types of acoustic devices characterised by their mode of wave propagation. The molecular displacement is indicated by black arrows. BAW: (a) QCM/TSM: thickness shear mode resonator also known as a bulk acoustic wave transducer or quartz crystal microbalance; (b) SH-APM: shear-horizontal acoustic plate mode resonator. SAW: (c) SV-SAW: shear-vertical surface acoustic wave/ Rayleigh wave resonator; (d) SH-SAW: shear-horizontal wave/ Love wave resonator (e) FPW: flexural-plate wave resonator. [50].....	21
Figure 2.8 AT-cut of a quartz crystal from which the metal coated QCM quartz crystals are produced. [60].....	23
Figure 2.9 A QCM resonates in the thick shear mode where $tq$ is the thickness of the crystal.....	24

Figure 2.10 Surface acoustic wave device. (a) Single surface acoustic wave (SAW) generated by patterned interdigitated transducers (IDTs) on a piezoelectric substrate. The wavelength of SAW is determined by the IDT pitch design, (b) Counter propagating SAWs create the standing surface acoustic wave (SSAW) and are actuated by a pair IDTs on the surface of a piezoelectric substrate. The superposition of two opposing identical SAWs results in the standing surface acoustic wave (SSAW) [67].27

Figure 2.11 Acoustic streaming [81] .....28

Figure 2.12 A schematic representation of biosensors.....30

Figure 2.13 Classification of different biosensor based on their elements.....30

Figure 2.14 Schematic of a QCM biosensing system.....32

Figure 2.15 Schematic of the SPR biosensing method [125] (a): Kretschmann configuration of a commercial SPR biosensor system, analyte-biorecognition elements binding on SPR sensor surface and the effective refractive index changes in the detection area (b) spectrum of reflected light before (I) and after (II) the molecules attachment (refractive index change). (c) Transient response of the binding reaction.35

Figure 3.1 Illustration of the Yee cell geometry and the EM components in the cell....42

Figure 3.2 Simulation mesh in the x-z view. Finer mesh is defined in area of interest around the gold nanodisk to offer higher calculation accuracy.....45

Figure 3.3 Illustration of the positive and negative photoresist profiles after exposure and development. ....49

Figure 3.4 Schematic of the EBL tool. At the top of the figure, the components of the electron gun unit are illustrated inside the yellow square. The subsequent components along the optical axis are also illustrated. ....50

Figure 3.5 The illustration of the variable resolution unit (VRU) and beam step size..52

Figure 3.6, Electrons scattering by the resist. The light blue sector indicates the exposed area in the resist layer and the profile of incident electrons inside the substrate. Generally, the lower incident energy leads to a larger forward scattering area. Such an exposed area ranges from tens of nanometres even up to microns in lateral size, which depends on the beam energy, resist thickness, feature size and so on [167].....53

Figure 3.7 Lift off process flow. After development of the resist bilayer, metal is deposited on the sample surface. The resist and surplus metal is then removed to leave the patterned metal on the substrate.....54

Figure 3.8 Schematic diagram of the Carbolite Gero Limited tube furnace .....55

Figure 3.9 After the first step, amine groups are generated on gold surface. ....56

Figure 3.10 After step3, a carboxylate group is generated.....56

Figure 3.11 After step 4, the functionalised layer on the gold surface is ready for reaction with amines.....57

Figure 3.12 Equivalent circuit model of QCM.  $R$  represents the energy loss mostly arising from viscous effects.  $L$  represents the initial mass/motional inertia of the system,  $C$  represents the mechanical elasticity of the quartz, and  $C_p$  determines the admittance away from resonance and consists of the capacitance of the quartz between the electrodes and the parasitic capacitance of the crystal fixture. The adsorbed load onto the crystal surface, which is described using impedance  $Z_v$ , can be described by the additional elements  $R_1$  and  $L_1$ , a measure of energy dissipation in the film and mass loading, respectively.....59

Figure 3.13 Separate reference and working QCMs with related frequency difference and isolator circuitry: IC<sub>1</sub> = 1/6 7404D Bipolar Hex Inverter; IC<sub>2</sub> = 1/6 7414D Hex Schmitt Trigger Inverter; IC<sub>3</sub> = 1/2 7474D Dual D type Flip-flop; IC<sub>4</sub> = 1/2 HCPL0600R2 Input Logic Gate Output Optocoupler; C<sub>1</sub> = 20 pF silver mica; C<sub>2</sub> = 50 pF silver mica; C<sub>3</sub> = 100pF ceramic; and L = 10 μH. V1 and V2 are separate 5 V power supplies[170]. .....61

Figure 4.1 Schematic of the simulated gold nanodisk array structure. (a) Top-down view of the simulated gold nanodisks. The green region is the simulated region. The red dash line encloses the unit cell of the nanodisk array structure.  $P$  denotes the array period and  $d$  denotes the disk diameter. (b) Cross section of the simulated gold nanodisks. The red dash line encloses the simulated unit cell.....64

Figure 4.2 Real and imaginary parts of the dielectric constant and the material fits generated by the software. (a) gold, Johnson and Christy model (b) SiO<sub>2</sub>, Palik model .....65

Figure 4.3: Simulation results from the 12 nanodisk array designs. The individual transmission spectra are shown in (a)-(d). The legend denotes the nanodisk period, $P$ , and the nanodisk diameter, $d$ . .....	66
Figure 4.4: Illustration of gold nanodisk array fabrication process flow.....	68
Figure 4.5 Illustration of the conventional writing method (left hand side) and the multipixel method (right hand side) for a single nanodot. The red circle and square represent the nanodot designed in L-edit. The conventional writing methods writes the whole nanodots area using a large number of beam points which needs more settle time. The multipixel method only writes a small area in centre of the nanodot and expose the whole area using back scattering effect. ....	69
Figure 4.6 Top-view SEM images of the Au nanodisks in design B3 (a) before and (b) after thermal annealing. The nanodisks exhibit smooth side walls and slightly smaller diameters (~9 nm smaller). ....	70
Figure 4.7 Illustration of how the linewidth of the LSPR transmission peak affects the resolution and the intensity measurement conducted at a fixed wavelength. The resonant wavelength shift is the same and caused by same refractive index change. .	71
Figure 4.8 The experimental extinction spectra corresponding to the designs A2, B2, B3 and C3. The extinction peaks of all the annealed samples exhibit narrower linewidth, larger transmission dip and a blue shift at the resonant wavelength. ....	72
Figure 4.9 SEM images of the gold nanodisk array designs A3, B3, C3, D2. The diameter of the nanodisks were the same as 200 nm (with a standard deviation of 4 nm, 5 nanodisks of each design had been randomly chosen for calculating dimensional errors). ....	73
Figure 4.10 The transmission spectra of the fabricated gold nanodisk array designs that correspond to A3, B3, C3, D2 in Figure 4.9. ....	73
Figure 4.11 Dispersion relationships of plasmonic resonance with array period of four nanodisk designs. The measured and simulated data are drawn with red and black markers respectively. Error bars are added based on the standard deviation of three different measurements on three different samples. The deviations are caused by fabrication imperfection and measurement error. ....	74

Figure 4.12 Transmission spectra of gold nanodisk array. (a) Simulated spectra. (b) Measured spectra. Both simulated and measured wavelengths were in the range 400 nm to 900 nm. ....75

Figure 4.13 Simulated transmission spectra of 200 nm diameter gold nanodisk arrays with varying array periods.....76

Figure 4.14 Summary of the nanodisk diameter effects on the (a) Intensity at the resonant wavelength, (b)FWHM, and (c) resonant wavelength of the LSPR. Error bars are added based on the standard deviation of three different measurements on three different samples. The deviations are caused by fabrication imperfection and measurement error. The twenty percent intensity difference between the simulated and the measured results is likely to be caused by the difference in the optical properties of the evaporated Au and the ones used by the simulation software (see Section 7.4 Future work).....77

Figure 4.15 Resonance wavelength shift (y-axis) as a function of refractive index of glycerine-water solution (x-axis) for different gold nanodisk designs (A2, A3, B2, B3, C2, C3) ( $P$  is the period and  $d$  is the diameter of the nanodisk). Linear fits have been added. In combination with the results shown in Figure 4.3, the designs with resonances at longer wavelengths display greater sensitivity than those with resonances at shorter wavelengths. Error bars are added based on the standard deviation of three different measurements on three different samples. The deviations are caused by fabrication imperfection and measurement error. ....79

Figure 4.16 (a) Simulated and (b) measured transmission spectra for the LSPR sensors in glycerine-water solutions of differing concentrations. (c) LSPR resonance wavelength  $\lambda_{min}$  shift as a function of bulk refractive index change of glycerine-water solution. ....81

Figure 4.17 Electric field intensity distributions represented as  $E^2$  contours at the resonance wavelength  $\lambda_{min}$ . (a), (b), and (c) are the simulated results when the nanodisk is in air; (d), (e), and (f) are the simulated results when the nanodisk array is in water. (a) and (d): Cross-section view of the nanodisk (b) and (e) Top view of the top surface of the nanodisk. (c) and (f) Top view of the bottom surface of the nanodisk. The outline.....83

Figure 4.18 Illustration of Protein A and IgG binding on sample surface.....84

Figure 4.19 LSPR transmission spectra of Protein A attached to gold nanodisk array design B3. The measurement range has been reduced to 500-900 nm in order to discern the change in spectra. Red and blue spectra were obtained after immobilisation of Protein A and IgG on the gold nanodisks, respectively.....84

Figure 5.1 Schematic diagram showing gold nanodisk array and the crystal planes of the LiNbO<sub>3</sub>. The coordinate system in this figure is for showing the different crystal cutting, and is not the same as the one of FDTD simulation.....89

Figure 5.2 Schematic of the simulated gold nanodisk array structure. (a) Top-down view of the simulated gold nanodisks. The green region is the simulated region. The red dash line encloses the unit cell of the nanodisk array structure.  $P$  denotes the array period and  $d$  denotes the disk diameter. (b) Cross section of the simulated gold nanodisks. The red dash line encloses the simulated unit cell.....90

Figure 5.3 (a) Simulated transmission spectra gold nanodisk arrays on LiNbO<sub>3</sub> with different periods,  $P$ , which show a red-shift tendency of resonance wavelength, also occurring among these designs as presented in the last chapter for gold nanodisk arrays on SiO<sub>2</sub>. (b) Cross section view of the electric-field distribution at the resonance wavelength ( $\lambda_0 = 845 \text{ nm}$ ) of nanodisk arrays with  $P=300 \text{ nm}$ ,  $d = 150 \text{ nm}$ .....91

Figure 5.4 Simulated transmission spectra for gold nanodisk arrays with varying disk diameters,  $d$ . The period,  $P$ , has been set as 300 nm for this set of simulation. Larger disks result in a redshift of the resonant wavelength, lower transmission and a larger bandwidth, as has been presented in last chapter. ....91

Figure 5.5 (a), (b) Simulated transmission spectra gold nanodisk arrays in water with different periods,  $P$ , and diameter,  $d$ , respectively. ....92

Figure 5.6 A scanning electron micrograph of gold nanodisks in a square array with a period of 300 nm on Y-cut LiNbO<sub>3</sub>. Inset: a microscope image tilted at 45°, where  $P$  and  $d$  are the periodicity and disk diameter, respectively. ....93

Figure 5.7 (a) Simulated transmission spectrum for LSPR sensors in water, where the two main resonance wavelengths are marked as  $\lambda_T$  and  $\lambda_B$ . (b), (c): Electric field intensity distributions in the xy plane at  $\lambda_T$  and  $\lambda_B$ , respectively. ....95

Figure 5.8. Measured transmission spectra for the LSPR sensors in a glycerine-water solution of differing concentrations. The average refractive index for each solution is given to the right of the concentration percentage. ....96

Figure 5.9 Resonance wavelength (nm, y-axis) versus refractive index of glycerine-water solution (x-axis). The black curve is the resonance wavelength shift at liquid mode  $\lambda_T$ , and the red curve is the resonance wavelength shift at LiNbO<sub>3</sub> mode  $\lambda_B$ .....97

Figure 5.10 Simulated and measured spectra of Au nanodisk arrays on LiNbO<sub>3</sub> surrounded by air. Data is recorded for four different polarisation angles: 0° (x-polarised), 30°, 60°, and 90° (y-polarised). ....98

Figure 5.11 Simulated and measured resonance wavelengths of Au nanodisk arrays on LiNbO<sub>3</sub> for seven different polarisation angles. ....99

Figure 5.12 . (a) Measured transmission spectra for different concentrations of glycerine-water solution using x-polarised light (0°). Inset: Simulated results of the transmission spectra for water (*Black line*: x-polarised light. *Red line*: unpolarised light. *Blue line*: y-polarised light.) (b) Measured transmission spectra for different concentrations of glycerine-water solution using y-polarised light (90°). Inset: Measured  $\lambda_B$  minima of concentration-dependent wavelength shift, for 0° (*hollow data*) and 90° (*solid data*) polarisations.....100

Figure 5.13 Comparison of experimental and simulation results for the LiNbO<sub>3</sub> based LSPR sensor in water.....101

Figure 6.1. Schematic diagram of the modified QCM showing the antibody/antigen binding reaction attached to the Au LSPR nanostructures.....105

Figure 6.2 VNA measured return loss (S11) spectra of the standard QCM and hybrid LSPR and QCM.....105

Figure 6.3 Frequency shift of the hybrid QCM versus increasing concentrations of glycerine-water solutions.....106

Figure 6.4 Simulated and measured transmission spectra of gold nanodisks on borosilicate glass and quartz substrate.....107

Figure 6.5 (a) Design of the pattern with the marker strategy for alignment in EBL. Yellow region is a small hole with a diameter of 400  $\mu\text{m}$  allowing the transmission measurement and (b) enlarged image showing the cross design which is used as the

origin for the global marker group (c) global marker group design: four  $40\ \mu\text{m} \times 40\ \mu\text{m}$  squares in a group. Four marker groups at four corners on the front and back surface. ....108

Figure 6.6 Fabrication process of the hybrid LSPR and QCM device. ....109

Figure 6.7 Schematic diagram of the combined QCM and LSPR instrument setup. ..110

Figure 6.8 Layout of the frequency comparison PCB .....111

Figure 6.9 Photograph of the PET flow cell. Crystal holder model: HC-48/U. Inset image is a close-up photo of the top electrode and the nanodisk array in the centre.....111

Figure 6.10 Changes in QCM frequency (line) and LSPR resonance wavelength (dotted line) versus time. Rabbit IgG was injected at  $t = 100\ \text{s}$ . ....113

Figure 6.11 End point QCM frequency shift versus resonance wavelength shift for different concentrations of IgG, demonstrating the linear relationship between QCM and LSPR in our experiments.....114

Figure 6.12 The endpoint of the (a) QCM frequency shift,  $f$ , and (b) LSPR resonant wavelength shift, as a function of IgG concentration was plotted and fitted to the Hill equation. The calculated dissociation constant of the reaction was  $6.67 \times 10^{-7}\ \text{M}$  for QCM and  $7.62 \times 10^{-7}$  for LSPR. ....115

# List of Tables

Table 4.1: 12 designs are divided into four groups (A-D) with each group having a fixed period $P$ and varying diameter $d$ .....	65
Table 4.2 Calculated Sensitivity, FWHM, FOM of six candidates for sensing application. .....	80
Table 6.1 The standard deviation for each concentration and each sensing techniques. .....	112
Table 6.2 Table for comparing hybrid sensor to other sensing technologies. ....	116

# List of Acronyms

APM	acoustic plate mode
APTES	(3-Aminopropyl)triethoxysilane
BAW	bulk acoustic wave
CAD	computer aided design
CCD	charge-coupled device
CMOS	complementary metal-oxide semiconductor transistor
CSV	comma separated values
DI	de-ionised
DNA	deoxyribonucleic acid
EBL	electron beam lithography
EM	electromagnetic
EMR	electromagnetic radiation
EOT	extraordinary optical transmission
FD	finite-difference
FDTD	finite-difference time-domain
FOM	figure of merit
FPW	flexural-plate wave
FT	Fourier transform

FWHM	full width at half maximum
IDT	interdigitated transducer
IF	intermediate frequency
IgG	immunoglobulin G
IPA	isopropyl alcohol
IR	infrared
ISFET	ion-sensitive field-effect transistor
JWNC	James Watt Nanofabrication Centre
LED	light emitting diode
LOAC	laboratory-on-a-chip
LOD	limit of detection
LOR	lift-off resist
LSP	localised surface plasmon
LSPR	localised surface plasmon resonance
MA6	Suss Microtec Mask Aligner 6
MIBK	methyl isobutyl ketone
NA	numerical aperture
NP	nanoparticle
PBS	phosphate buffered saline

PCB	printed circuit board
PML	perfectly matched layer
PMMA	polymethyl methacrylate
POC	point of care
PSA	prostate specific antigen
PVD	physical-vapour deposition
QCM	quartz crystal microbalance
QCM-D	quartz crystal microbalance with dissipation monitoring
RF	radio frequency
RIU	refractive index unit
RU	response unit
SAM	self-assembled monolayer
SAW	surface acoustic wave
SEM	scanning electron microscope
SERS	surface-enhanced Raman scattering
SH	shear-horizontal
SP	surface plasmon
SPP	surface plasmon polariton
SPR	surface plasmon resonance

SPRi	SPR imaging
SSAW	standing surface acoustic wave
SV	shear-vertical
TE	transverse electric
TM	transverse magnetic
TSM	thickness shear mode
TTL	transistor-transistor logic
UV	ultraviolet
VLSI	very large scale integration
VNA	vector network analyser
VRU	variable resolution unit

# 1. Introduction

## 1.1 Motivation

Many diseases are complex, heterogeneous, and depends on environmental and lifestyle factors, hence this requires new low-cost *in vitro* diagnostic technology to measure multiple biomarkers quantitatively in real time and simultaneously. In order to solve these challenges, many label-free optical based or acoustic transducers have emerged as individual biosensors. However, having a single type of sensor is frequently inadequate to provide sufficient information towards a disease accurately. Acoustic sensing devices use the resonance phenomenon of piezoelectric material, where the frequency of its mechanical oscillation is dependent upon the acoustic mass of the sum of the deposited molecules and the solvent coupled to the adsorbed molecules. Optical sensing techniques measure the change in the refractive index arising from the molecular adsorption on the metal surface, thus determining the molecular mass of thin films [1]. Therefore, in a surface adsorption process, the integration of optical and acoustic sensing can not only give information regarding weight but also detect the film hydration status that provides insights into the conformational properties of the molecules in the formed layer on surface and the biomolecule adsorption characteristics. Due to the complementary characterise of optical and acoustic sensing, a lot of effort have been made to explore the possibilities of integrating these two types of sensing elements on to a single platform.

Over the last two decades, surface plasmon resonance (SPR) has been demonstrated as a potential optical technique to perform label-free and highly sensitive detection, and has been successfully mass-manufactured and commercialised as a reliable platform for biomolecular interactions analysis. In addition, quartz crystal microbalance (QCM), which uses bulk acoustic wave and surface acoustic wave (SAW) sensing devices are also widely used for biomolecular studies. Hence, a lot of work has been focussing on the potential of combining QCM and SPR, or SAW and SPR into one single device and create a hybrid biosensor. However, the SPR sensing technology mostly adopts the prism-based configuration and requires an angular scanning instrument to do precise

measurement, which is bulky and expensive. This restricts the hybrid sensor to be developed into a portable a point-of-care (POC) device.

As opposed to SPR, the collinear excitation/collection coupling scheme of localised surface plasmonic resonance (LSPR) sensors shows great advantages. LSPR biosensing can be achieved using metallic nanoparticles deposited on to a substrate. LSPR can be exploited to create an enhanced electric field at the surface of metallic nanoparticles (boundary between a metal and dielectric). At resonance, the field is strongly localised so that the exact characteristics of the associated spectrum are highly sensitive to the refractive index of any material that is close, or attached, to the surface [2] [3]. By altering a nanoparticle arrays' geometry, it is possible to engineer desirable spectral characteristic for higher sensing performance. Two kinds of substrate were investigated in the course of this work: 1).  $\text{SiO}_2$ , which includes non-piezo active borosilicate glass and piezoelectric material quartz. 2).  $\text{LiNbO}_3$ , which is piezoelectric, birefringent and having a large refractive index.

In this thesis, it will be demonstrated that by ensuring both sensing components share common materials and fabrication processing techniques, it is possible to combine optic sensing element and acoustic sensing element to create a hybrid biosensor. The hybrid biosensor can be used for optical and acoustical sensing simultaneously on the same film.

## 1.2 Aims and Objectives

The main aim of this project is to combine plasmonic sensing and acoustic sensing technique to create a hybrid biosensing device. The objectives of this project can be described as follows:

- Simulation, fabrication and characterisation of LSPR gold nanodisks, which are designed to be integrated with bulk acoustic devices.
- Simulation, fabrication and characterisation of LSPR gold nanodisks on piezoelectric, high refractive index material –  $\text{LiNbO}_3$ , which supports SAW streaming and sensing.
- Integration of LSPR gold nanodisks with QCM to create the hybrid biosensing device.

### 1.3 Thesis Outline

The remainder of this thesis is organised in seven chapters.

**Chapter 2** provides a literature study on the current state of technology with regards to structured photonic materials and their sensing applications. The chapter begins with an introduction to plasmonics, including SPR and LSPR. This section also presents the background theory of the plasmonic nanostructures that the initial discussion is concerned with Maxwell's equations, which underlie the operation of all plasmonic structures that have been designed in the course of this work. Then the chapter continues with an introduction to biosensing technologies and the development of label-free biosensing, specifically with regards to the benefits that they present over labelling technologies. The background of plasmonic biosensing and acoustic biosensing are presented. This is followed by the introduction of the Mie's theory, which is the base of LSPR sensing. Sauerbrey's theory for QCM operation has been given as well. The chapter also includes a discussion on comparing SPR and LSPR technologies.

**Chapter 3** describes the methods used to simulate, fabricate and characterise the structured photonic materials and the acoustic device that will be presented in this work. The first section provides an overview of the finite difference time-domain (FDTD) method, follows by a description of Lumerical FDTD Solutions which has been used to simulate the LSPR nanostructures, which has been designed during the course of this project. The next section provides the micro and nanofabrication processes carried out in the James Watt Nanofabrication Centre to develop the plasmonic nanostructure and the customised QCM. The chapter also includes a description of the characterisation methods: spectrophotometry for LSPR, vector network analysis and frequency comparison circuit for QCM. The surface functionalisation process used in this work is also described in this chapter.

**Chapter 4** presents the design, simulation, fabrication and characterisation of the gold nanodisk arrays and the tunable properties of their plasmon resonance. The purpose of this set of experiments is not only to show that the optical resonances of the LSPR nanostructures can be designed as a sensing device but also to optimise their structure

design for better resolution and higher sensitivity. The sensitivity (resonance wavelength shift per refractive index unit change) and the figure of merit (sensitivity over the linewidth of the LSPR transmission spectrum) of different designs have been compared. An immunoassay was conducted on the nanostructure design that gives the best performance, showing the early results of using LSPR nanostructures as a biosensing tool.

**Chapter 5** investigates the potential for the integration of acoustic and LSPR technologies on a single device, and in particular to study the optical properties of LSPR nanostructures on piezo-active materials - LiNbO<sub>3</sub>. The fabrication process for LiNbO<sub>3</sub>, a pyroelectric material, has been described in this chapter. An in-depth investigation into the optical properties of the LiNbO<sub>3</sub> has been done, including its high refractive index and birefringence. Following this, optimisation has been made to the designed LSPR sensor on LiNbO<sub>3</sub> based on the results from this chapter and Chapter 5.

**Chapter 6** reports on the design and fabrication of a hybrid sensor that integrates transmission-mode LSPR into a QCM for studying biochemical surface binding reactions. The LSPR and QCM design are presented individually in the beginning. Then, the chapter presents the fabrication and characterisation of the hybrid sensor integrating the two technologies, and demonstrates that it is possible for LSPR nanostructures to work with QCM for sensing applications. An immunoassay was conducted on the hybrid sensor and the result shows it can be used as a biosensor. The chapter also compares the hybrid sensor with individual technologies and SPR biosensor in terms of different aspects.

**Chapter 7** summarises the work that has been presented in this thesis and also offers some discussions on future work that could be undertaken as a continuation of this project.

## 2. Background

This chapter presents the overview and the theoretical basis of optical and acoustic technology, from their development to the advancements in plasmonics and acoustics for biosensing applications. This chapter also describes different biosensing methods and presents the advantages of label-free optical and acoustic sensing over labelling technologies. The background of integrating optical and acoustic sensing technologies is presented and an overview of the development of these hybridised devices is included.

### 2.1 Light Interaction with Nanoscale Metal Features

#### 2.1.1 Plasmonics

A plasmon is a collective oscillation of the free electrons in a conductive material, *e.g.* noble metals. For fixed ions in a metal, when an external electric field is introduced, the negative charged electrons move with respect to the positive charged cores. After removal of the electric field, this displacement of electrons causes them to oscillate at the plasma frequency. Plasmons are the quantisation of this oscillation. Plasmons take the form of surface plasmons (SPs) at the interface between a metal and a dielectric. The coupling between electromagnetic radiation (EMR) and SPs happens at the metal surface when excited by EMR. The interaction when the SP is confined to a nanoparticle is defined as a localised surface plasmon (LSP). The study of these light-matter interactions is called “plasmonics” and it has enabled a vast array of applications in the optics area.

#### 2.1.1 Electromagnetics and Dielectric Properties of Metals

The derivation of the equations associated with surface plasmon waves begins with Maxwell’s equations. Maxwell’s equations are the foundation of electromagnetism theory where the creation of electric and magnetic fields is explained. Key equations for understanding plasmon waves theory can be derived from Maxwell’s equations in their classical form:

$$\text{Gauss' law} \quad \nabla \cdot \mathbf{D} = \rho_f \quad 2.1$$

$$\text{Gauss' law for magnetism} \quad \nabla \cdot \mathbf{B} = 0 \quad 2.2$$

$$\text{Faraday's law of induction} \quad \nabla \times \mathbf{E} = -\frac{\partial \mathbf{B}}{\partial t} \quad 2.3$$

$$\text{Ampere's law} \quad \nabla \times \mathbf{H} = \mathbf{J}_f + \frac{\partial \mathbf{D}}{\partial t} \quad 2.4$$

$\mathbf{D}$  is the electric flux density,  $\mathbf{B}$  is the magnetic flux density,  $\mathbf{E}$  is the electric field,  $\mathbf{H}$  is the magnetic field,  $\rho_f$  is the free charge density and  $\mathbf{J}_f$  is the free current density [4]. For homogeneous, isotropic and linear dielectric material,  $\mathbf{D}$  and  $\mathbf{B}$  can be related to  $\mathbf{E}$  and  $\mathbf{H}$  by:

$$\mathbf{D} = \varepsilon_0 \mathbf{E} + \mathbf{P} = \varepsilon_0 \varepsilon_r \mathbf{E} \quad 2.5$$

$$\mathbf{H} = \frac{\mathbf{B}}{\mu_0} - \mathbf{M} = \frac{\mathbf{B}}{\mu_0 \mu_r} \quad 2.6$$

where  $\mathbf{P}$  is the polarisation,  $\mathbf{M}$  is the magnetisation,  $\varepsilon_0$  and  $\mu_0$  are the electric permittivity and magnetic permeability of free space, respectively.  $\varepsilon_r$  and  $\mu_r$  are the relative electric permittivity and relative magnetic permeability of the material, respectively. The material permittivity and permeability are given by:

$$\mu = \mu_0 \mu_r \quad 2.7$$

$$\varepsilon = \varepsilon_0 \varepsilon_r \quad 2.8$$

Deriving from Equation 2.3 and Equation 2.4, the electromagnetic wave equations in free space are given in terms of both the electric field (Equation 2.9) and magnetic field (Equation 2.10):

$$\nabla^2 \mathbf{E} - \frac{\varepsilon_r \mu_r \partial^2 \mathbf{E}}{c^2 \partial t^2} = 0 \quad 2.9$$

$$\nabla^2 \mathbf{B} - \frac{\varepsilon_r \mu_r \partial^2 \mathbf{B}}{c^2 \partial t^2} = 0 \quad 2.10$$

where  $c$  is the speed of light in vacuum,  $c = \frac{1}{\sqrt{\epsilon_0\mu_0}}$ ,  $\mathbf{B}$  is perpendicular to  $\mathbf{E}$ , and both are perpendicular to the direction of propagation [4].

All materials used in this project are non-magnetic with a relative permeability  $\mu_r = 1$ . Their relative permittivities and refractive indices, which are complex quantities, are given by Equation 2.11 and Equation 2.12 respectively:

$$\epsilon_r = \epsilon_1 + i\epsilon_2 \quad 2.11$$

$$n_r = n_1 + in_2 \quad 2.12$$

where  $\epsilon_1$  and  $\epsilon_2$  are the real and imaginary components of the permittivity.  $n_1$  and  $n_2$  are the real and imaginary components of the refractive index. The relationship between permittivity and refractive index can be found in the following equations:

$$n_r = \sqrt{\epsilon_r} \quad 2.13$$

$$\epsilon_1 = n_1^2 + n_2^2 \quad 2.14$$

$$\epsilon_2 = 2n_1n_2 \quad 2.15$$

The Drude model, proposed in 1900 by Paul Drude, assumes that the metal is formed by a lattice of positively charged ionic cores with negatively charged gas. The negatively charged gas is formed by ensemble conduction electrons moving freely inside the metal and is also called plasma. This model is used to describe the optical properties of a metal. If a volume of plasma is displaced by a distance,  $\mathbf{x}$ , it results in a polarisation,  $\mathbf{P}$ . This leads to the formation of an electric field,  $\mathbf{E}$ , with the following relationship:

$$\mathbf{E} = \frac{-\mathbf{P}}{\epsilon_0} = \frac{nex}{\epsilon_0} \quad 2.16$$

where  $n$  is the electron density and  $e$  is the electronic charge. Since the Drude model only considers electron motion damping from collisions, represented by the mean free time between collisions,  $\tau$ , the equation of motion of a free electron can be written as:

$$m \frac{d^2 \mathbf{x}}{dt^2} + m \frac{1}{\tau} \frac{d\mathbf{x}}{dt} = -e\mathbf{E} = -\frac{ne^2 \mathbf{x}}{\varepsilon_0} \quad 2.17$$

where  $m \frac{d^2 \mathbf{x}}{dt^2}$  is the acceleration force;  $m$  is the electron mass.  $m \frac{1}{\tau} \frac{d\mathbf{x}}{dt}$  is the friction force due to collisions and the term  $-e\mathbf{E}$  is the electric force.

A description of the time dependent electric field is given in Equation 2.18, and the oscillation of the electron response as a function of time is given in Equation 2.19:

$$\mathbf{E}(t) = \mathbf{E}_0 e^{-i\omega t} \quad 2.18$$

$$\mathbf{x}(t) = \mathbf{x}_0 e^{-i\omega t} \quad 2.19$$

Substituting into the motion equation presented in Equation 2.17 we obtain:

$$\mathbf{x}_0 = \frac{e}{m(\omega^2 + \frac{1}{\tau}i\omega)} \mathbf{E}_0 \quad 2.20$$

Since  $-\mathbf{P} = ne\mathbf{x}$ , we can rewrite Equation 2.20 as:

$$\mathbf{P} = -\frac{ne^2}{m(\omega^2 + \frac{1}{\tau}i\omega)} \mathbf{E} \quad 2.21$$

Substituting this description of  $\mathbf{P}$  into the relation for  $\mathbf{D}$  in Equation 2.5 we obtain:

$$\mathbf{D} = \varepsilon_0 \left( 1 - \frac{ne^2}{\varepsilon_0 m (\omega^2 + \frac{1}{\tau}i\omega)} \right) \mathbf{E} \quad 2.22$$

The natural frequency of oscillation associated with the plasma is known as the plasma frequency and is defined as:

$$\omega_p = \sqrt{\frac{ne^2}{\varepsilon_0 m}} \quad 2.23$$

Then Equation 2.18 changes into:

$$\mathbf{D} = \varepsilon_0 \left( 1 - \frac{\omega_p^2}{\omega^2 + \frac{1}{\tau}i\omega} \right) \mathbf{E} \quad 2.24$$

From comparison between Equation 2.5 and Equation 2.24, the relative permittivity of a metal can be written in terms of its plasma frequency as follows:

$$\varepsilon_r = 1 - \frac{\omega_p^2}{\omega^2 + \frac{1}{\tau}i\omega} \quad 2.25$$

and the real and imaginary components of  $\varepsilon_r$  are:

$$\varepsilon_1 = 1 - \frac{\omega_p^2 \tau^2}{1 + \omega^2 \tau^2} \quad 2.26$$

$$\varepsilon_2 = \frac{\omega_p^2 \tau}{\omega(1 + \omega^2 \tau^2)} \quad 2.27$$

At frequencies below the plasma frequency ( $\omega < \omega_p$ ), the permittivity is negative and the metal is reflective in nature. At frequencies above the plasma frequency ( $\omega > \omega_p$ ), the permittivity is positive and the metal becomes mainly absorbing.

### 2.1.2 Surface Plasmon Resonance

In 1902, R. W. Wood, when observing the spectrum of a continuous light source reflected by a periodic array of tiny grooves, noticed that the spectrum exhibited an unusual large drop in intensity when the incident wave was polarised with its magnetic vector parallel to the metallic gratings, *i.e.* transverse-magnetic (TM) polarisation. This phenomenon discovered by Wood soon drew the attention of other optical specialists and was termed as the “Wood’s anomaly” [5]. In 1907, Lord Rayleigh proposed the first explanation of the anomalies in the transmission dips by defining the grating equation where he assumed that the metal was a perfect conducting material [6]. However in 1936, Strong’s study into various metallic gratings with the same periodicity showed that the anomalies occurred at longer wavelengths than that predicted by the Rayleigh grating equation [7]. Finally in 1941, Fano introduced a surface mode into the explanation of Wood’s anomaly, *i.e.* the SP was linked with the Wood’s anomaly [8]. After 17 years, Ritchie *et. al.* used the SP instead of the surface mode to describe the phenomenon and experimentally verified Fano’s theory [9].

SPs, also known as surface plasmons polaritons (SPPs), are coherent oscillations of free electrons at the boundaries between a metal and dielectric. Under certain resonant conditions, it is possible for light that is incident on a metal surface to couple with the SPs at the metal-dielectric interface in a process known as surface plasmon resonance (SPR). SPs are tightly confined to the metal surface and propagate in the  $x$ - and  $y$ -

directions along the metal-dielectric interface [10] [11] [12], for distances on the order of tens to hundreds of microns, and decay evanescently in the  $z$ -direction with  $1/e$  decay lengths on the order of 200 nm [13] [14] [15]. A schematic of the propagating SP at a metal-dielectric interface is shown in Figure 2.1 [16]. The field components are illustrated in Figure 2.1(a), where it can be observed that the electric field is normal to the interface and the magnetic field is perpendicular to the direction of propagation. The evanescent decay of the fields that are perpendicular to the interface are illustrated in Figure 2.1(b), where  $\delta_d$  and  $\delta_m$  denote the decay length into the dielectric and metal, respectively. This shows how the SPs are bound to the surface of the metal-dielectric interface. The high confinement, which is typically subwavelength in scale, leads to a large field enhancement close to the surface. The SP is therefore very sensitive to changes in the local dielectric environment close to the metal surface, making it well suited for chemical and biological sensing applications [17].

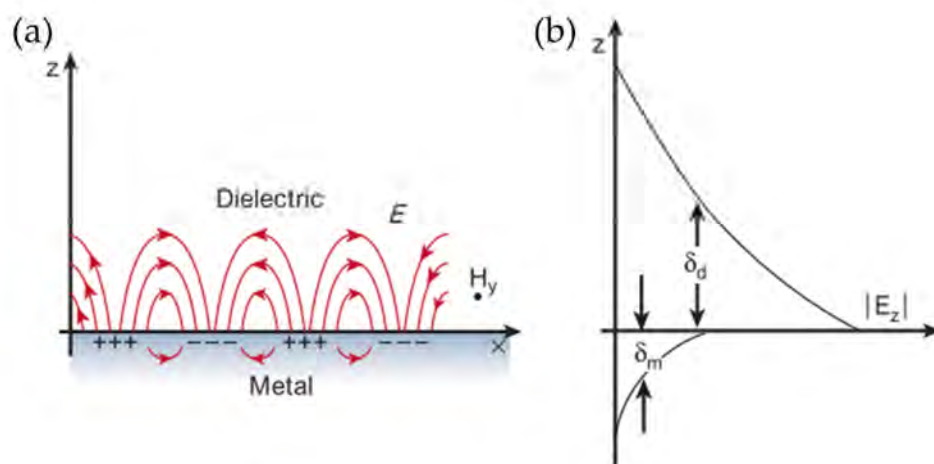


Figure 2.1 Illustration of a surface plasmon (SP) propagating at a metal-dielectric interface. (a) A schematic of a SP propagating in the  $x$  direction with electric and magnetic field components shown. (b) Evanescent decay of the field component that is perpendicular to the interface into both the metal and the dielectric [16].

There is a momentum mismatch between the incident light and SPs that must be overcome before SPs can be excited. The first method to provide the incident light photons with additional momentum has already been described in the discussion of Wood's anomaly; a periodic corrugation in a metal surface can diffract incident light into the plane of the metal-dielectric interface, resulting in resonant coupling of light

with SPs [5]. A schematic illustrating the excitation of SPs via grating coupling is shown in Figure 2.2(a). The second and the most conventional approach is called prism coupling or Kretschmann configuration based coupling as shown in Figure 2.2(b). At a particular angle of incidence, the SPs are excited at the interface of the metal and dielectric layer showing a sudden dip in the light reflectance. The third method is waveguide-based coupling showing in Figure 2.2(c). Light is injected into the wave guiding layer and propagates along through total internal reflection. An evanescent field is generated in the vicinity of the waveguide boundary, which induces a SPR at the interface between metal and dielectric layer.

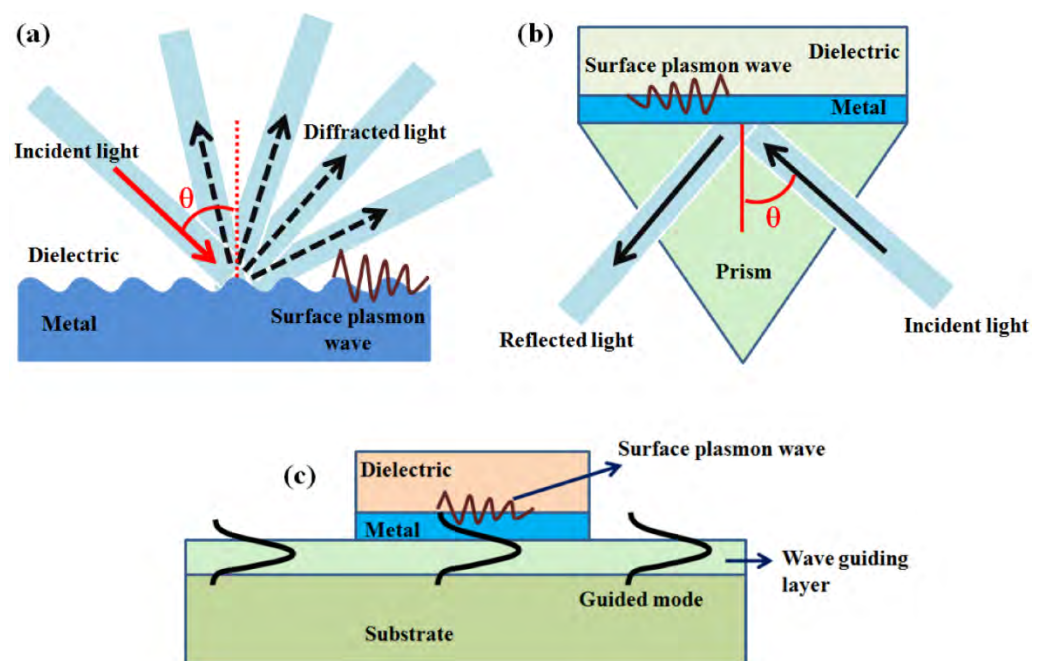


Figure 2.2 Illustrations of the different methods by which incident light can couple with surface plasmons (SP) for SPR generation [18] (a) Grating coupling, (b) prism coupling – Kretschmann configuration and (c) waveguide coupling.

Although prism coupling is the most commonly used technique for SPR sensing, the basic principle is the same as grating coupling where the propagating SPs at the interface of metal and dielectric react to changes in the dielectric environment and result in detectable changes in the reflected light for a given angle as adsorption occurs on the metal surface. This results in a shift in the effective refractive index of the surface. The first application of the SPR phenomenon was for gas detection in 1982 [19] and it was not long until it was developed as a biosensing tool for measuring antibody

adsorption [20]. The highly-confined nature of SPs means that they can also be used for a range of applications overcoming the diffraction limit, such as subwavelength focussing through plasmonic lenses [21] [22] and subwavelength lithography [23] [24].

### 2.1.3 Localised Surface Plasmon Resonance

Ruby glass was used as an optical metamaterial by the Romans in the 4<sup>th</sup> century for making the Lycurgus cup shown in Figure 2.3. Under daylight, the cup appears as green colour, but when a light source is placed inside the cup the transmitted colour will make it look like the glass glows in red [25] [26]. This phenomenon also happens to stained glass in the Sinte Chapelle, the transmitted light from outside not only shows exquisite colour but also exhibits varying colour based on the time of the day and the viewing point. Due to the changing solar incident angles, the different colour patches on the window show an intensity change and colour variation. These astonishing optical effects are due to the plasmonic resonance and the secret ingredient embedded in the glass - metallic nanoparticles (NPs).



Figure 2.3 The Lycurgus cup [25]

The embedded metallic NPs in the ruby glass are typically 5-60 nm in size, which are much smaller than the incident wavelength. Light interacts with these sub-wavelength NPs and leads to a plasmon that oscillates locally around the NP with a frequency known as the localised surface plasmon resonance (LSPR) [27] [28] [29]. The Romans made the Lycurgus Cup, but they did not know the theory behind the phenomenon due to the lack of necessary physics, specifically Maxwell's equations. A millennium

after the creation of the ruby glass, Faraday fabricated gold nanoparticles (GNPs) and systematically described the unusual optical properties of gold colloid solution [30]. Inspired by Faraday, Gustav Mie developed an analytical solution to Maxwell's equations that describes the extinction spectra of spherical NPs of arbitrary size in 1908 [31] [32]. In 1970, the colours associated with glasses embedded with metallic NPs were attributed to the interaction of light with SPs [33].

When metal nanostructures interact with a light beam, part of the incident photons are absorbed and part are scattered in different directions. Both absorption and scattering are greatly enhanced when the LSPR is excited. Figure 2.4 is an illustration of the interaction between light with metallic NPs. When a small spherical metallic NP is irradiated by light, the oscillating electric field causes the conduction electrons to oscillate coherently. When the electron cloud is displaced relative to the atom nuclei, the Coulomb force between the nuclei and electrons generates a restoring force and results in a collective oscillation of the electron cloud regarding the fixed nuclear array known as LSP. The LSP has two important effects: first, electric fields near the NP's surface are greatly enhanced and rapidly falling off with distance; second, the particle's optical extinction has a maximum at the plasmon resonant frequency LSPR, which occurs at visible wavelengths for noble metal nanoparticles. The LSPR is determined by: the metal properties, the shape and size of the metal, and, similar to SPR, the refractive index of the surrounding medium which is the basis for the LSPR sensing applications.

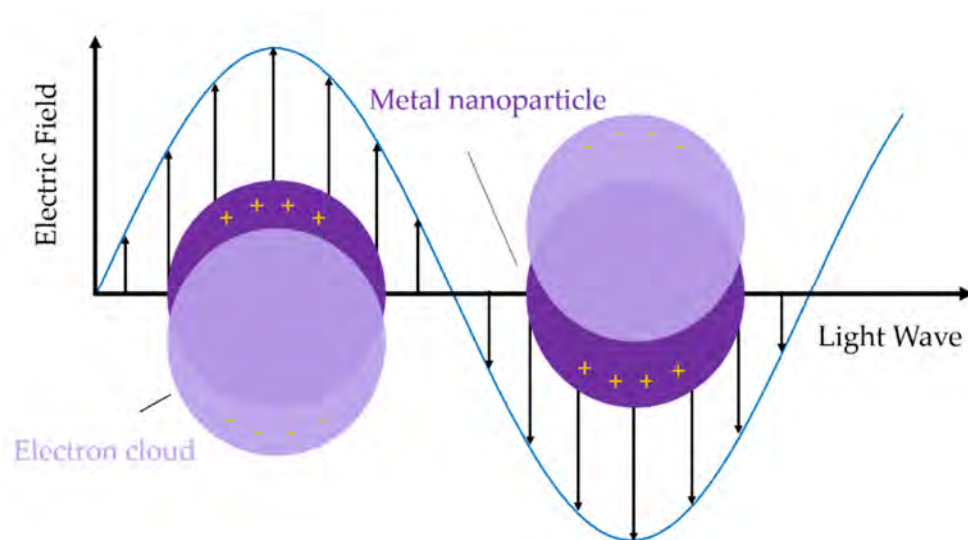


Figure 2.4 Schematic of a plasmon oscillation for a metallic sphere, showing the displacement of the electron cloud, positive charge and the fixed atomic nuclei.

Figure 2.5 shows several approaches to the measurement of LSPR spectra. The most straightforward is transmission spectroscopy (Figure 2.5(a)). The set-up can measure the transmission spectrum of the LSPR nanostructures by recording the wavelength dependence of the light passing through the sample. The second approach adopts the reflective geometry. The probe fibre is used both to direct the incident light (centre of the fibre) and also to collect the light reflected from the sample surface (radial array of fibres). This method is essential to non-transparent samples. For samples with a small region or even single nanoparticles, dark-field light-scattering measurement can be conducted with a dark-field microscope objective whereby a high-numerical aperture condenser brings light to the sample and a high-numerical aperture objective collects the scattered light at a low angle as shown in Figure 2.5(c).

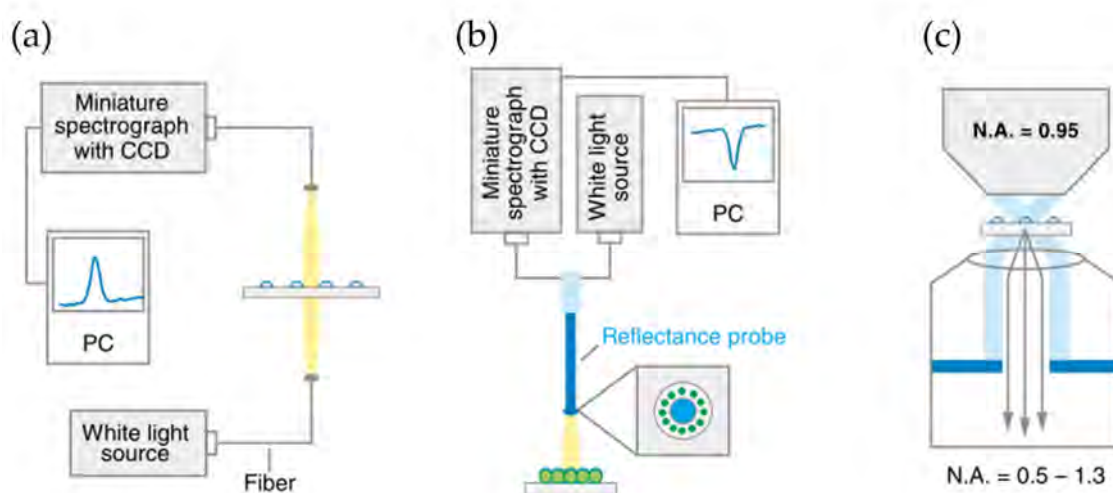


Figure 2.5 Setups to measure LSPR spectra. (a) Transmission and (b) reflectance geometries for measuring extinction spectra of nanoparticle arrays. (c) Dark-field scattering experimental setup using a high-numerical aperture dark-field condenser and a high-numerical aperture microscope objective for measuring single-nanoparticle scattering spectra.[34].

Due to the properties of the LSPR, in addition to its appliance in artwork, LSPR spectroscopy has been exploited as a powerful technique for chemical and biological sensing experiments [34] [35]. The nature of the NPs, the potential of miniaturising the setup and the diversity of available platforms, both in solution and on a surface, make LSPR sensing capable of developing label-free, multiplexed, and on-chip portable

devices [36]. Moreover, the LSPR is responsible for the electromagnetic-field enhancement that leads to surface-enhanced Raman scattering (SERS) [37].

### 2.1.3.1 Mie Theory

In order to understand the factors that affect the large increase in absorption and scattering when LSPR occurs, in the early 20<sup>th</sup> century, Gustav Mie developed an analytical solution to Maxwell's equations for spherical particles [31]. He considered a spherical NP of radius  $a$  that is irradiated by  $z$ -polarised light of wavelength  $\lambda$  (where  $a$  is much smaller than the wavelength of light  $\lambda$ ; *i.e.*  $a/\lambda < 0.1$ ). In this limit, the magnitude of the electric field appears static around the NPs (as seen in Figure 2.4), and Maxwell's equations can be solved using a quasi-static approximation. The electromagnetic field outside the NP is given by [34]:

$$E_{out}(x, y, z) = E_0 \hat{z} - \alpha E_0 \left[ \frac{\hat{z}}{r^3} - \frac{3z}{r^5} (x\hat{x} + y\hat{y} + z\hat{z}) \right] \quad 2.28$$

where,  $x$ ,  $y$ , and  $z$  are the usual Cartesian coordinates;  $\hat{x}$ ,  $\hat{y}$ , and  $\hat{z}$  are the Cartesian unit vectors;  $r$  is the radial distance; and  $\alpha$  is the metal polarisability expressed as:

$$\alpha = ga^3 \quad 2.29$$

where  $a$  is the radius of the sphere and  $g$  is defined as:

$$g = \frac{\epsilon_{in} - \epsilon_{out}}{(\epsilon_{in} + 2\epsilon_{out})} \quad 2.30$$

where  $\epsilon_{in}$  is the dielectric constant (*i.e.* permittivity) of the metal NP, and  $\epsilon_{out}$  is the dielectric constant of the external environment. Because  $\epsilon_{in}$  is strongly dependent on the wavelength according to the description of Equation 2.25, the magnitude of the NP electromagnetic enhancement is in consequence wavelength dependent. When the dielectric constant of the metal is roughly equal to  $-2\epsilon_{out}$ , the maximum electromagnetic field enhancement occurs. In the case of silver and gold, this condition is met in the visible region of the spectrum. The radius ( $a$ ) and external dielectric constant ( $\epsilon_{out}$ ) also play key roles in determining the electromagnetic field outside the particle. This effect will be shown experimentally in Chapter 4. Examining Equation 2.28, it can be seen that the electromagnetic field enhancement decays with  $r^{-3}$ ,

implying a finite sensing volume around the NP as mentioned in Section 2.1.2 when comparing SPR and LSPR sensing technology.

According to Mie theory, the extinction spectrum of an arbitrary shaped NP is described as follows:

$$E(\lambda) = \frac{24\pi^2 N a^3 \varepsilon_{out}^{3/2}}{\lambda \ln(10)} \left[ \frac{\varepsilon_i(\lambda)}{(\varepsilon_r(\lambda) + \chi \varepsilon_{out})^2 + \varepsilon_i(\lambda)^2} \right] \quad 2.31$$

where  $\varepsilon_r$  and  $\varepsilon_i$  are the real and imaginary components of the metal dielectric function  $\varepsilon_{in}$ , respectively. Again, wavelength dependency of the metal dielectric function needs to be noted.  $N$  is the electron density. The factor of  $\chi$  that appears in front of  $\varepsilon_{out}$  is the shape factor that accounts for deviation from spherical particle geometries into higher aspect ratio structures [38]. For the case of a sphere, the value of  $\chi$  is 2. The assumption is made because Mie's theory can only solve analytically for spheres and spheroids, and it can only be an approximation for all other geometries. Due to this fact, researchers have developed additional numerical methods aimed at other structures, including the discrete dipole approximation [39] and the finite difference time-domain methods which will be discussed in Section 3.1 in the simulation method section [40].

### 2.1.3.1 Background Theory of LSPR Sensing

In addition to modelling the extinction of particles, several equations are used to describe how LSPR is used for sensing experiments.

For example, the LSPR extinction wavelength maximum,  $\lambda_{max}$ , is sensitive to the dielectric constant  $\varepsilon$ . Thus, changes in the local environment, such as the adsorption process of biomolecules, should cause a shift in  $\lambda_{max}$ . The wavelength shift can be expressed as follows:

$$\Delta\lambda = m \cdot (n_{final} - n_{initial}) \quad 2.32$$

where  $m$  is the bulk refractive index sensitivity of the NP in units of RIU<sup>-1</sup>.  $n_{initial}$  and  $n_{final}$  are the refractive indices of the external environment in the initial and final state. For adsorption processes,  $n_{initial}$  can be defined as the external environment in the absence of the adsorption layer. The refractive index of the final state is more complex because it involves the combination of the refractive index of both the adsorbed layer

at the metal surface as well as the external environment at longer distance. Here, this distance-dependent refractive index can be defined as:

$$n(z) = \begin{cases} n_A, & 0 \leq z \leq d \\ n_E, & d < z < \infty \end{cases} \quad 2.33$$

where  $d$  is the thickness of the adsorption layer,  $n_A$  is the refractive index of the adsorption layer and  $n_E$  is the refractive index of the external environment (see Figure 2.6).

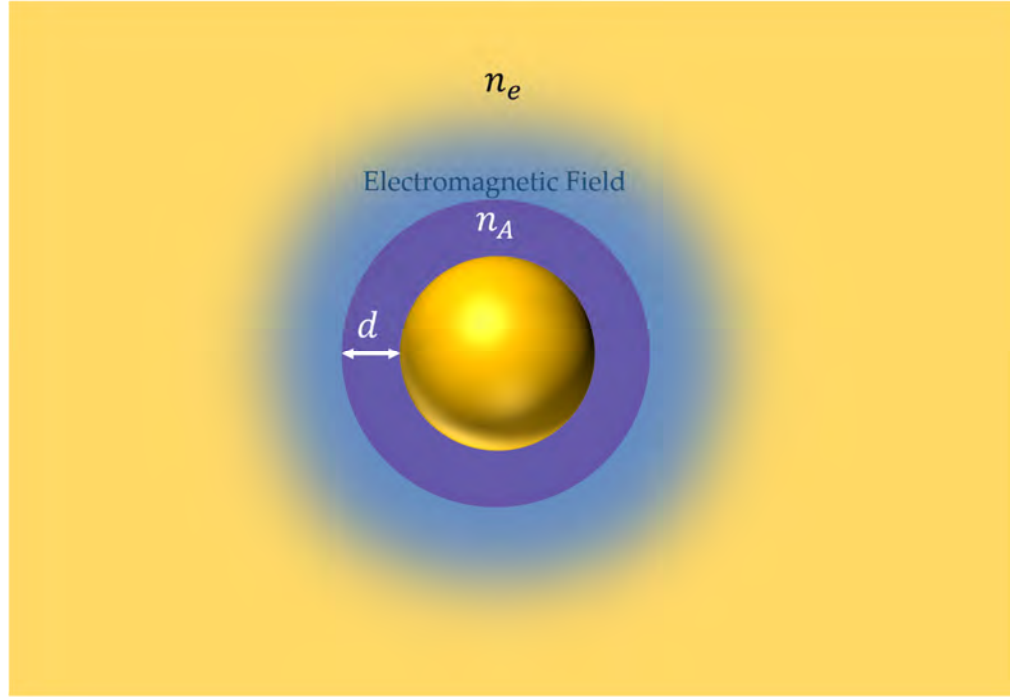


Figure 2.6 Illustration of the metal NP used for biosensing. The metal NP is in the centre. The blue region is the exponentially decaying electromagnetic field. The purple region is the adsorption layer. The yellow region is the external environment.

Moreover, this refractive index should be weighted by the distance dependent intensity of the electromagnetic field since the field is more intense closer to the NP surface. The electromagnetic field can be approximated as decaying exponentially with a characteristic length  $l_d$ :

$$E(z) = E_0 \exp\left(\frac{-z}{l_d}\right) \quad 2.34$$

To normalise the refractive index by the relative field intensity ( $I \propto nE^2$ ), it is necessary to use the electromagnetic field squared and the normalisation factor becomes:

$$\left[ \exp\left(\frac{-z}{l_d}\right) \right]^2 = \exp\left(\frac{-2z}{l_d}\right) \quad 2.35$$

Now, the effective refractive index,  $n_{eff}$ , which normalises the z-dependent refractive index by the intensity factor is defined in Equation 2.35:

$$n_{eff} = \frac{2}{l_d} \int_0^\infty n(z) \exp\left(\frac{-2z}{l_d}\right) dz \quad 2.36$$

The factor of  $\frac{2}{l_d}$  normalises the integral such that  $n_{eff} = n_E$  in the absence of an adsorption layer.

Combining Equation 2.36 with Equation 2.33, the integral becomes:

$$n_{eff} = \frac{2}{l_d} \left[ \int_0^d n(z) \exp\left(\frac{-2z}{l_d}\right) dz + \int_d^\infty n(z) \exp\left(\frac{-2z}{l_d}\right) dz \right] \quad 2.37$$

Evaluating the integral yields the following expression:

$$n_{eff} = n_A \left[ 1 - \exp\left(\frac{-2d}{l_d}\right) \right] + n_E \exp\left(\frac{-2d}{l_d}\right) \quad 2.38$$

Substituting  $n_{eff}$  for  $n_{final}$  and  $n_E$  for  $n_{initial}$ , Equation 2.32 becomes:

$$\Delta\lambda = m \cdot (n_{eff} - n_E) = m \cdot \left\{ n_A \left[ 1 - \exp\left(\frac{-2d}{l_d}\right) \right] + n_E \exp\left(\frac{-2d}{l_d}\right) - n_E \right\} \quad 2.39$$

Grouping the  $n_E$  terms and rearranging the equation, it becomes:

$$\Delta\lambda = m \cdot (n_A - n_E) \left[ 1 - \exp\left(\frac{-2d}{l_d}\right) \right] \quad 2.40$$

This equation is the basis of LSPR wavelength-shift sensing experiments. This equation can be simply reduced to  $\Delta\lambda = m \cdot (n_A - n_E)$  in bulk solvents since  $d$  goes to infinity. In this case,  $n_A$  is the refractive index of the new solvent and  $n_E$  is the refractive index of the original bulk solvent.

#### 2.1.4 Extraordinary Optical Transmission

Extraordinary optical transmission (EOT) was first reported by Ebbesen *et al.* in 1998 by detailing a crucial experimental result on the transmission of light through nanohole arrays in thin Ag films on a quartz substrate [41]. Their experiment indicated that the transmitted light through nanohole arrays at certain wavelengths had a much higher intensity than estimated by the classical theory of Bethe [42]. In Bethe's theory, the

transmission efficiency through a single hole of radius,  $r$ , is proportional to  $(\frac{r}{\lambda})^4$ , where  $\lambda$  is the wavelength of the incidence. According to Bethe's theory, for subwavelength apertures, when  $r$  is smaller than  $\lambda$ , the resulting transmission intensity should be very low. Furthermore, if one considers the fill factor of the metal film, the transmission intensity should also be lower than that reported in [41].

The cause of the EOT phenomena was attributed to SPs due to its absence when the metal layer was replaced by a non-metallic material. In 1998, Ghaemi *et al.* presented an equation to predict the SP transmission maximum for a square lattice hole array:

$$\lambda_{max} = \frac{a}{\sqrt{i^2 + j^2}} \sqrt{\frac{\epsilon_m \epsilon_d}{\epsilon_m + \epsilon_d}} \quad 2.41$$

where  $a$  is the distance between the holes.  $\lambda_{max}$  is the wavelength of the transmission peak,  $i$  and  $j$  are integers denoting the scattering orders, with  $i \geq 0, j > 0$ .  $\epsilon_m$  and  $\epsilon_d$  are dielectric constants of the metal and the surrounding dielectric, respectively. For a hole array with a triangular lattice arrangement, this equation becomes:

$$\lambda_{max} = \frac{a\sqrt{3}}{2\sqrt{i^2 + j^2 + ij}} \sqrt{\frac{\epsilon_m \epsilon_d}{\epsilon_m + \epsilon_d}} \quad 2.42$$

Even though it was later shown that the prediction made by these equations is more accurate towards the minimum on the lower wavelength side of the transmission maximum, it is still a good approximation for the initial design.

The revelation of EOT also led to various applications as with SPR and LSPR. By altering the periodicity, the lattice arrangement, the geometry of holes and the materials, extensive simulation and experiments have been done to exploit EOT phenomenon for designing low cross-talk, high transmission optical colour filters [43].

Since EOT is caused by SPs modes coupled on both sides of the noble metal film, the resultant far-field transmission peak wavelength is determined by the refractive index  $n_d (= \sqrt{\epsilon_d})$  of the surrounding dielectric. Under this condition, the EOT phenomenon was also investigated to develop a biosensing system. An EOT-based sensing platform was presented by A. De Leebeek *et al.* which was used to monitor a protein binding event [44].

## 2.2 Acoustic Wave Devices

### 2.2.1 Acoustic and Piezoelectricity

Since the 18<sup>th</sup> century, due to the emergence of Bach, Haydn, and Mozart, and the development and improvement of musical instruments at that time, scientific endeavour has been made for the development of sound and acoustics. The concept of frequency was first given by Marin Mersenne [45]. The conductivity and intensity of sound, diffraction, reflection, and echoes were well understood according to Chladni's text published in 1807. By the 1800s, the speed of sound propagating in air measured by Parisian academics yielded values that were within 1% of the most accurate current measurements. Lord Rayleigh, the famous Nobel prize winner, made many contributions in nearly all aspects of acoustics.

In 1880, Pierre and Paul-Jacques Curie discovered the *direct piezoelectric effect*: certain materials produce electric charges on their surfaces as a consequence of applying mechanical stress. The induced charges are proportional to the mechanical stress. The root of the word 'piezo' means 'pressure' in Greek. The name 'piezoelectricity' means 'electricity by pressure' and was proposed by Hankel in 1881 [46]. In the following year, the Curie brothers verified the existence of the reverse process, which was earlier predicted by Lippmann[47]. That is, the materials showing the direct piezoelectric effect also conversely have a geometric strain proportional to an applied electric field known as the *converse piezoelectric effect* [48]. The materials showing these phenomena are called *piezoelectric material*.

Piezoelectric materials did not have widespread applications until quartz was used as a resonator in SONAR during World War I. Following the discovery of the phenomenon of ferroelectricity by Valasek [49], (Ferroelectric materials exhibit one or more phases and have domain structure in which the individual polarisation can be changed by an applied electric field. All ferroelectric materials exhibit piezoelectric effect because their lack of symmetry in crystal structure.) many successful results were obtained in the investigation and manufacture of piezoelectric materials. More man-made piezoelectric materials such as lithium niobate ( $\text{LiNbO}_3$ ), lithium tantalate ( $\text{LiTaO}_3$ ), and lead zirconate titanate (PZT) have been developed and utilised in

piezoelectric devices. Naturally, these successful creations resulted in a revival of the research and development of piezoelectric devices. Piezoelectricity, one branch of crystal physics, soon became the base of many applications: frequency filters in communication devices, actuators and motors for fine positioning, detectors for pressure variations in the form of sound such as piezoelectric microphones or guitars, etc. [46].

In the piezoelectric material of acoustic wave devices, the waves can propagate on the surface, i.e. surface acoustic wave (SAW) or in the bulk of the resonator, i.e. bulk acoustic wave (BAW). The wave type and the phase velocity depend on the piezoelectric material crystal structure.

Figure 2.7 shows different types of acoustic devices characterised by their mode of wave propagation.

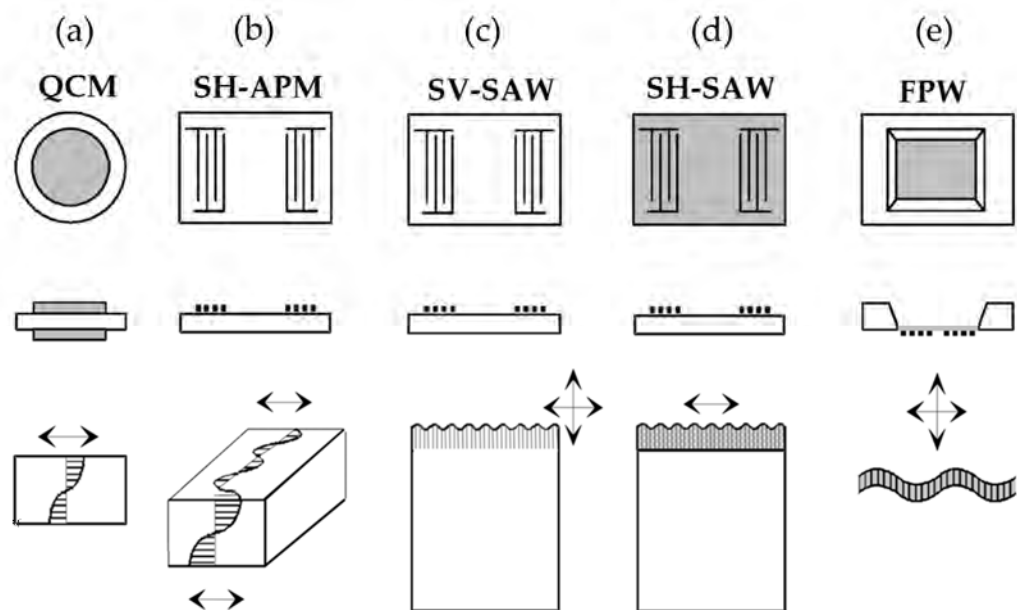


Figure 2.7 Different types of acoustic devices characterised by their mode of wave propagation. The molecular displacement is indicated by black arrows. BAW: (a) QCM/TSM: thickness shear mode resonator also known as a bulk acoustic wave transducer or quartz crystal microbalance; (b) SH-APM: shear-horizontal acoustic plate mode resonator. SAW: (c) SV-SAW: shear-vertical surface acoustic wave/Rayleigh wave resonator; (d) SH-SAW: shear-horizontal wave/ Love wave resonator (e) FPW: flexural-plate wave resonator. [50]

### 2.2.2 Bulk Acoustic Wave and Quartz Crystal Microbalance

### 2.2.2.1 Bulk Acoustic Wave

In the bulk of an ideally infinite unbounded solid, two types of BAW can propagate. They are the longitudinal waves, also called compressional/extensional waves, and the transverse waves, also called shear waves, which identify vibrations where particle motion is parallel and perpendicular to the direction of wave propagation respectively. Longitudinal waves have higher velocity than shear waves. Acoustic plate modes (APM), although generated at the device surface, belong to BAWs.

### 2.2.2.2 Quartz Crystal Microbalance

Quartz, as a piezoelectric material, is commonly used as a crystal oscillator in digital devices. W. Cady first used it as a frequency-reference element in time-keeping applications in 1921 [50]. The oldest application of quartz crystal resonators as sensors is the quartz crystal microbalance (QCM). A QCM typically consists of a thin AT-cut quartz plate with circular electrodes on both parallel main surfaces of the crystal. By applying an alternating electric field across the quartz crystal through the upper and lower metal electrodes covering the quartz surface, shear-mode BAWs are generated. AT-cut is  $35^{\circ} 10'$  from the  $z$  axis of the quartz crystal (Figure 2.8). The temperature dependence of the resonant frequency of AT-cut crystal is essentially zero at  $25^{\circ}\text{C}$  since it has a low temperature coefficient at room temperature [51]. The mass sensitivity of a QCM is dependent on the thickness of the crystal, which determines its resonant frequency. The thinner the QCM is, the higher its resonance frequency and sensitivity. However, thin QCMs are very fragile. Most applications have used commercial QCM devices operating in the 5-10 MHz range. QCMs are mostly operated as resonators in pure thickness-shear mode, hence the sensors are also called TSM sensors.

The theoretical foundation for the use of quartz crystals as a microbalance or detector can be traced to Lord Rayleigh, who showed that small changes in the inertia of a mechanically vibrating system perturbed the resonant frequency of the system [52]. The suggestion to make QCM as transducers for chemical analysis was first made by Sauerbrey in 1959 [53]. The demonstration was made by King in 1964 by applying a sensing film coating on the crystal surface to enable the adsorption of gas molecules, which in turn, induced a shift in the oscillation frequency that is directly related to the

mass of the adsorbed compounds [54]. QCMs early applications were in the chemistry area where the QCM was used to measure mass binding from the gas-phase species to the quartz surface. These represented some of the earliest chemical sensors for moisture and volatile organic compounds [54] [55], environmental pollutants [56], and gas-phase chromatography detectors [57]. In the 1980s, a liquid based QCM was developed as a new technology to measure changes in frequency that related to the changes in viscosity and density in highly damping liquid media by immersing one face into the solution [58]. This work paved the way for applications in electrochemistry and biology. The recent success of the QCM technique is due to its ability to measure mass changes associated with liquid-solid interface phenomena, as well as to characterise energy dissipation or viscoelastic behaviour of the mass deposited upon the metal electrode surface of the quartz crystal [59]. To give a better understanding of the QCM and QCM sensing technology, the theoretical background of QCM and QCM sensing are discussed in the following section.

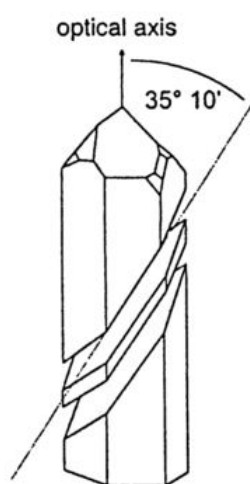


Figure 2.8 AT-cut of a quartz crystal from which the metal coated QCM quartz crystals are produced. [60]

### 2.2.2.3 QCM working and sensing principle

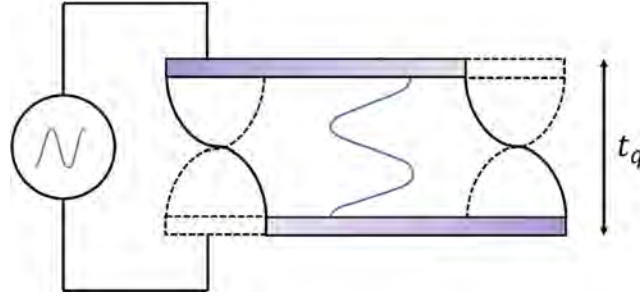


Figure 2.9 A QCM resonates in the thick shear mode where  $t_q$  is the thickness of the crystal.

With an AT-cut quartz crystal and an appropriate alternating potential, a standing shear wave can be formed at the resonant frequency of quartz characterised by the following equations:

$$f_0 = \frac{v}{2t_q} \quad 2.43$$

$$v = \sqrt{\frac{\mu_q}{\rho_q}} \quad 2.44$$

where  $v$  is the velocity of sound in the quartz crystal,  $\mu_q = 2.947 \times 10^{11} \text{ g/cm} \cdot \text{s}^2$  is the shear modulus of AT-cut quartz crystal,  $\rho_q = 2.647 \text{ g/cm}^3$  is the density of quartz crystal and  $t_q$  is the crystal thickness. For a commercial quartz crystal working at 5 MHz the crystal thickness is  $\sim 330 \mu\text{m}$ .

The quality factor (Q) is defined as the ratio of resonant frequency and full-width-half-maximum bandwidth (FWHM):

$$Q = \frac{\text{Frequency}}{\text{Bandwidth}} = \frac{f_0}{\Delta f_{FWHM}} \quad 2.45$$

For a QCM, the Q-factor can easily achieve more than  $10^5$ . The higher the Q-factor, the easier it is to determine the resonance frequency with good precision. The inverse Q-factor is called 'dissipation factor' ( $D$ ) which is related to the viscoelastic properties of the adsorbate. QCM with dissipation analysis is called QCM-D technique.

Sauerbrey used the quartz crystal as an ultrasensitive weighting device and proposed that the mass per unit area loaded on a quartz crystal surface was proportional to the resonance frequency shift:

$$\Delta f_m = -\frac{2nf_0^2}{\sqrt{\rho_q\mu_q}} \frac{\Delta m}{A} \quad 2.46$$

where  $n$  is the overtone or harmonic number ( $= 1, 3, 5, \dots$ ),  $\Delta f$  is the frequency shift occurring on mass loading,  $f_0$  is the crystal frequency under no load and  $A$  is the electrode surface area. This equation is only valid for a rigid film distributed uniformly on the surface with thickness thinner than the quartz crystal plate.

For liquid contact measurements, in 1985, Kanazawa and Gordon derived the following relationship between the frequency shift and the liquid's viscous load:

$$\Delta f_L = -n^{1/2} f_0^{3/2} \sqrt{\frac{\eta_l \rho_l}{\pi \rho_q \mu_q}} \quad 2.47$$

where  $\Delta f$  is the frequency shift occurring on mass loading,  $f_0$  is the crystal frequency under no load,  $\rho_l$  and  $\eta_l$  represent the liquid density and viscosity, respectively.

If the film is not rigid or uniform, the Sauerbrey equation is expanded to incorporate film elasticity [61]. The change in frequency ( $\Delta f$ ) for QCM in a liquid phase system can be expressed as the frequency change due to the mass load ( $\Delta f_m$ ) and the viscous load ( $\Delta f_L$ ) as follows:

$$\Delta f = \Delta f_m + \Delta f_L = -\frac{2nf_0^2}{\sqrt{\rho_q\mu_q}} \frac{\Delta m}{A} - n^{1/2} f_0^{3/2} \sqrt{\frac{\eta_l \rho_l}{\pi \rho_q \mu_q}} \quad 2.48$$

By inspecting the above equations, it can be seen that the sensitivity of a QCM is increased with increasing the fundamental (operating) resonant frequency  $f_0$ , which can be increased by either reducing the crystal thickness or operating the crystal at its higher overtone.

In case that the analysed films are sufficiently rigid, the linear relationship between changes in frequency and coupled mass is a safe assumption even in the case with coupled solvents [62]. Therefore, using the analysis with QCM alone is feasible in this case. However, in most biosensing scenarios, the ideal cases are too rare. Important information, in particular with respect to coupled solvents, can only be achieved by operating the QCM technique in parallel with complementary methods such as SPR and LSPR sensing as discussed previously.

### 2.2.3 Surface Acoustic Wave

The most important aspect of SAWs is their relatively slow speed compared to the bulk wave speed of sound in the medium itself, causing the wave and its energy to be trapped on the surface within a very few wavelengths [63]. The most common type of SAWs are the Rayleigh waves, which were mathematically predicted by Lord Rayleigh in 1884 [64]. Rayleigh waves/shear-vertical surface acoustic waves (SV-SAW) are two-dimensional waves given by the combination of longitudinal and transverse waves and are confined at the surface down to a penetration depth in the order of the wavelength. One of the disadvantages of Rayleigh waves is that they are not suited for most liquid applications because of radiation losses [65]. In contrast, Shear-horizontal (SH) SAWs have only a very low penetration depth into a liquid, hence a device with pure or predominant SH modes can operate in liquids without significant radiation losses in the device. Other SAWs, such as Love waves, flexural plate wave (FPW), leaky SAW *etc.* can also be found in acoustic devices.

A SAW device, schematically show in Figure 2.10(a), consists of one or more sets of metallic interdigital transducers (IDTs) built on a piezoelectric substrate, such as quartz, lithium niobate ( $\text{LiNbO}_3$ ), or lithium tantalate ( $\text{LiTaO}_3$ ). The earliest example of an IDT design is found in the patent of N. Tesla issued in 1891[66].

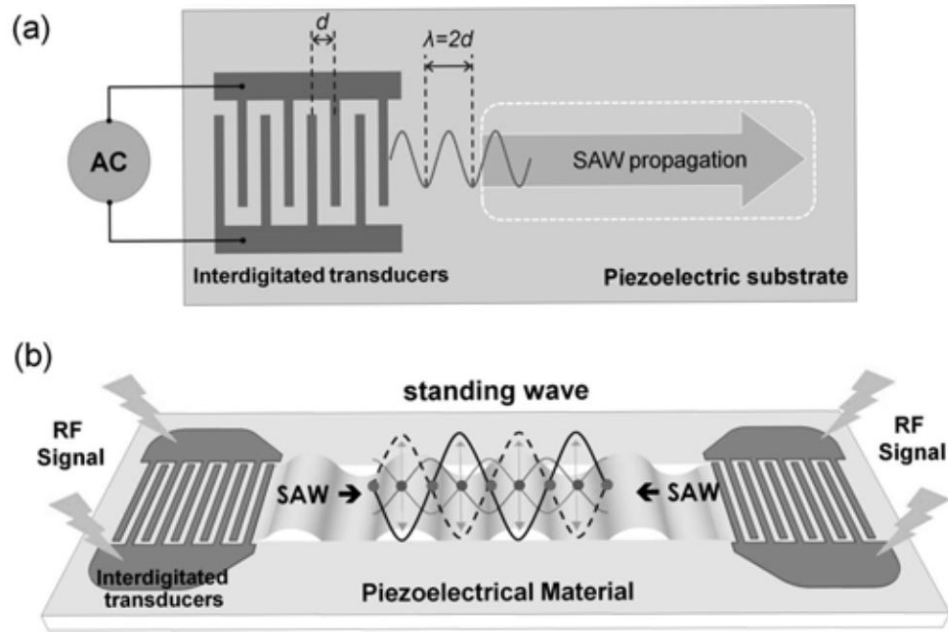


Figure 2.10 Surface acoustic wave device. (a) Single surface acoustic wave (SAW) generated by patterned interdigitated transducers (IDTs) on a piezoelectric substrate. The wavelength of SAW is determined by the IDT pitch design, (b) Counter propagating SAWs create the standing surface acoustic wave (SSAW) and are actuated by a pair IDTs on the surface of a piezoelectric substrate. The superposition of two opposing identical SAWs results in the standing surface acoustic wave (SSAW) [67].

To operate the surface acoustic wave device, a sinusoidal electrical alternating current (AC) signal with frequency  $f_0$  is sent through the first interdigitated transducer. This array of interdigitated electrodes will alternate polarity according to the electrical signal, creating alternating regions of electric fields between fingers as seen in Figure 2.10. Due to the piezoelectric effect, these electric fields will cause alternating regions of tensile and compressive strain between fingers of the electrodes, producing a mechanical wave at the surface. Since the mechanical wave will propagate in both directions from the input IDT, half of the energy of the waveform will propagate across the delay line (Figure 2.10(b)) in the direction of the output IDT. In some devices, a mechanical absorber or reflector is added between the IDTs and the edges of the substrate to prevent interference patterns or reduce insertion losses respectively.

The frequency of the SAW,  $f_s$ , can be calculated according to the equation:

$$f_s = \frac{C_s}{\lambda_s} \quad 2.49$$

where  $C_s$  is the phase velocity of the travelling acoustic wave which is dependent on the substrate material, crystal cut angle and SAW propagation direction.  $\lambda_s$  is the wavelength of the SAW and is determined by the IDT pitch design,  $\lambda_s = 2d$ .

Until 1980s, SAW technology had been mainly used for military applications. Starting from 1980s, the telecommunications industry has been the largest user of SAW devices, consuming approximately three billion SAW filters are used for the RF (radio frequency) and IF (intermediate frequency) sections of the transceiver electronics [68] [69]. SAW also offers a solid-state actuation mechanism. When the SAW comes in contact with a liquid, the acoustic energy diffracts into the liquid due to the difference between the wave propagation speed in the piezoelectric substrate, and that in the liquid,  $C_l$  (~1485 m/s for water), launching a leaky SAW with decaying amplitude. The refraction angle  $\theta_R$ , which is referred to as the Rayleigh angle, can be calculated by the ratio of the sound velocity in the piezoelectric substrate to the sound velocity in the liquid,  $\theta_R = \sin^{-1}\left(\frac{C_l}{C_s}\right)$ . The pressure wave results in fluid flow and the process is known as SAW streaming (see Figure 2.11). SAW streaming is typically used in microfluidic mixing [70] [71], pumping [72] [73], concentration [74] [75] [76] microparticle patterning [77] [78], and microparticle directing [79] [80].

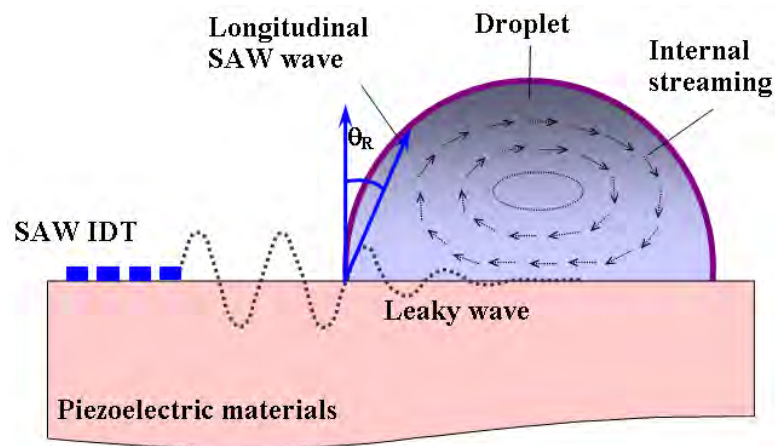


Figure 2.11 Acoustic streaming [81]

SAW streaming was also integrated with an SPR sensing platform to accelerate the binding reaction [82]. The shear stresses imposed by the SAW streaming was employed to stretch and unfold protein fibres [83].

On the other hand, a standing surface acoustic wave (SSAW) can be formed of two series of SAWs generated from two pairs of IDTs and propagate in opposite directions to the microchannel. The superposition of two opposing, identical SAWs give rise to constructive and destructive interference, which results in a SSAW with pressure nodes (minimum pressure amplitude) and anti-pressure nodes (maximum pressure amplitude), as shown in Figure 2.10(b). These pressure fluctuations make microparticles in a liquid migrate to either the pressure nodes or the anti-pressure nodes. By altering the applied frequency and utilising complex device resonance architectures, particles can be rapidly and precisely manipulated. There are many microparticle manipulation techniques in the field of microfluidics such as microparticle tweezing [84], microparticle focussing [85], and microparticle separation [86]. These microfluidic devices have great potential for biological, chemical and medical applications [87].

There are also many established or developing applications of SAW sensing technologies including biological/chemical sensing [88] [89]; vapour, humidity, temperature, and mass sensing for industrial and commercial applications [90] [91] [92] as well as acoustic microscopy [93]; *etc.*

### 2.3 Biosensing

Biosensors were first demonstrated in 1962 by the pioneers Clark and Lyons. Since then, research communities from various fields such as very large scale integration (VLSI), physics, chemistry, and material science have come together to develop more sophisticated, reliable, and mature biosensing devices. Applications for these devices are in the fields of medicine, agriculture, biotechnology, as well as the military and bioterrorism detection and prevention.

Biosensors are known as other names such as immunosensors, chemical canaries, resonant mirrors, glucometers, biochips, and biocomputers. Two commonly cited definitions by S.P.J. Higson and D.M. Frazer, respectively, are “a biosensor is a chemical sensing device in which a biologically derived recognition entity is coupled to a transducer, to allow the quantitative development of some complex biochemical parameter” and “a biosensor is an analytical device incorporating a deliberate and

intimate combination of a specific biological element (that creates a recognition event) and a physical element (that transduces the recognition event)" [94].

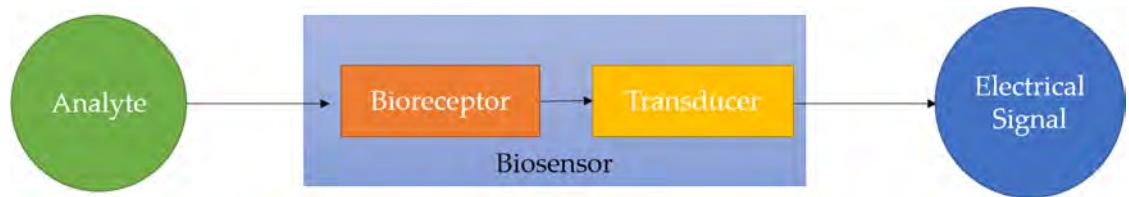


Figure 2.12 A schematic representation of biosensors

A biosensor consists of two main components: a bioelement, *i.e.* a bioreceptor, which recognises the sensing target, and a sensor element, *i.e.* a transducer, which converts this recognition into an electrical signal (Figure 2.12). Biosensors can be classified by their bioreceptor recognition target or transducer mechanism (

Figure 2.13). Depending on the recognition target, biosensors can be categorised into three groups: biocatalytic group comprising enzymes, bio-affinity group including antibodies and nucleic acids, and microbe based containing microorganisms such as bacteria and phage. Depending on the transducing mechanism used, the biosensors can be of many types such as: acoustic biosensors, optical biosensors, thermal biosensors, ion-sensitive field-effect transistor (ISFET) biosensors, or electrochemical biosensors.

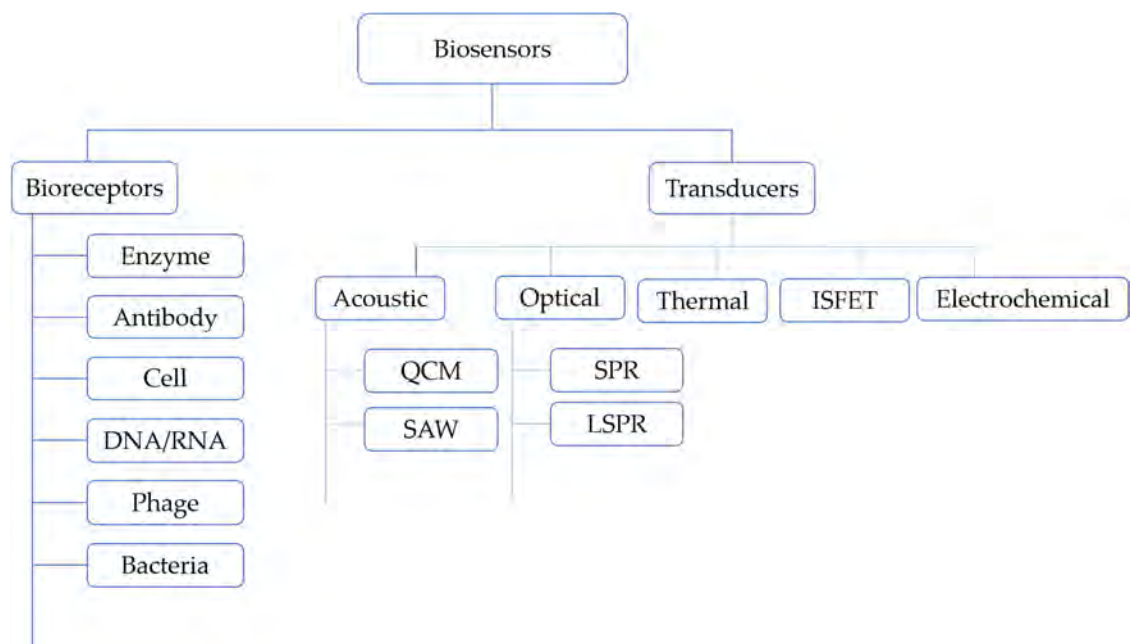


Figure 2.13 Classification of different biosensor based on their elements

Biosensors can also be classified into label-free and label-based. Label-based techniques rely on the specific properties of labels like fluorescence, chemiluminescence, *etc.* for detecting a particular target. However, the process of labelling and purification is associated with sample losses, which is critical when sample quantity is limited. Labelling processes can also have a detrimental effect on the functionality and stability of molecules like proteins. Mass spectrometry, acoustic biosensing, SPR, and LSPR are label-free techniques, which can conquer these disadvantages. Moreover, for various diseases including Alzheimer's disease and cancer, certain proteins' expression can be used as biomarkers. Due to the requirement of early detection, there is a strong need for affordable and high throughput screening technologies that can monitor and diagnose various medical conditions. Innovative solutions toward cost-effective and portable biosensor devices are highly desirable. Acoustic and optical biosensing shows great potential towards these requirements and are promising candidates for point-of-care (POC) applications.

### 2.3.1 Acoustic Biosensing

Acoustic wave sensors measure the changes in acoustic wave physical properties that are caused by the interaction of an acoustic wave with the binding reaction between the bioreceptor and the analyte [95]. These changes contain information such as the amount and the conformation of adsorbed molecules. Acoustic biosensors are of two types depending on the acoustic wave type: the quartz crystal microbalance which utilise BAW and the SAW biosensors.

#### 2.3.1.1 QCM Biosensor

The schematic of a traditional QCM biosensor can be found in Figure 2.14. The crystal is housed in a flow cell where only one side of the crystal is set into contact with the solution of the analyte injected into the cell. The QCM is connected to an interface electronic system including an oscillator, frequency counter or vector network analyser.

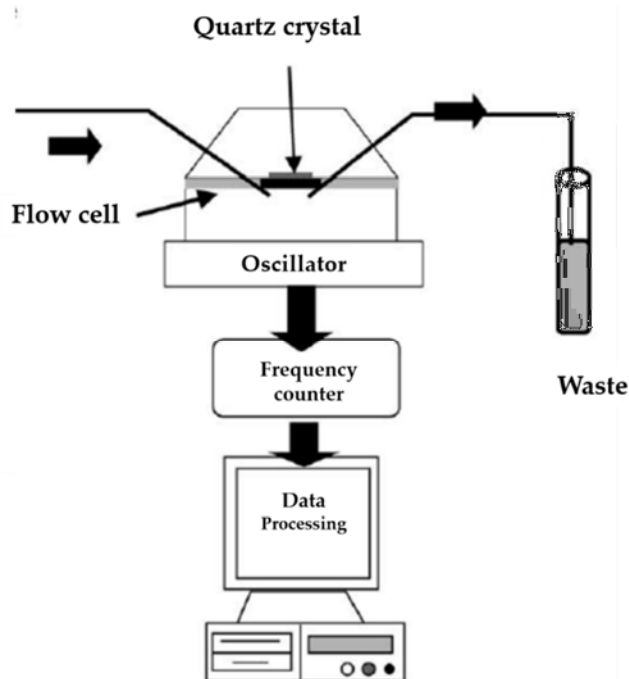


Figure 2.14 Schematic of a QCM biosensing system.

The QCM has a limit of detection (LOD) lower than  $1\text{ng}/\text{cm}^2$  and can be used for adsorbents of several hundreds of nanometre thickness. Due to this high dynamic range, the QCM is used in a broad application field, from small molecules and biological macromolecules [96] to whole virus cells [97] [98]. The sensor resonant frequency is related to the sensitivity and is inversely proportional to the crystal thickness. For the fundamental mode, resonance frequencies of 5 to 30 MHz are typical. For higher frequencies, the crystals can be operated at a higher order harmonic resonance frequency.

QCM is widely used as an immunosensor to detect the formation of antigen-antibody complexes and has applications such as the detection of *Listeria monocytogenes* [99] and immunoglobulin G (IgG) [100]. It can also be used as nucleic acid sensor [101] and cell sensor [102].

More recently, attention is not only drawn to measuring the adsorbed mass but also to investigate the viscoelastic properties of the adsorbent. This can be done by not only reading out the resonance frequency, but also the energy dissipation. The latter system is named quartz crystal microbalance with dissipation monitoring (QCM-D). With this technique, novel types of investigations such as changes of the viscoelastic properties

of polymers, vesicle adsorption and lipid bilayer formation, and cross-linking of protein layers are performed.

### 2.3.1.2 Surface Acoustic Wave Biosensor

As mentioned before, due to the high attenuation of the SV-SAW devices in a liquid environment, early studies in the 1980s that attempted to transfer the simple method of gas sensing into a biosensor were not successful. After years of research [103] [104] [106] [107], the Love wave, which is a type of SH-SAW was adopted in the design of SAW biosensor. A biosensor based on the Love wave was first developed by Gizeli and co-workers using a quartz substrate and a polymethyl methacrylate (PMMA) waveguiding layer. IgG was adsorbed at the sensor surface, and anti-IgG and protein A were used as the analyte [108] [109] [110].

There were also some developments based on commercially available SAW devices. Rapp *et.al.* presented the SH-SAW immunosensor based on LiTaO<sub>3</sub> in 1993. Anti-glucose oxidase was immobilised on the commercially available SAW device to detect glucose oxidase in the sample. Later, similar devices with aluminium IDTs were covered by polymer film such as PMMA for protection purposes and to provide a chemically homogeneous surface for further biochemical modifications [111] [112] [113] [114] [115] [116] [117]. SiO<sub>2</sub> is also frequently used as the waveguiding layer on SH-SAW sensors [118].

The high sensitivity makes the SAW biosensor a perfect device for protein molecules, ultra-small cells or DNA detection, and more researchers have been doing experiments using SAW biosensors. A third order harmonic mode SAW that had a frequency of 6.4 GHz has been achieved using LiNbO<sub>3</sub>, and the device has been used to detect DNA sequences and cells [119]. Zhang *et al.* have reported a prostate specific antigen (PSA) sensor based on the Love wave biosensor [120]. They also adopted the 'dual delay line configuration' using one channel acting as a reference, and a detection limit of 10mg/mL was obtained. Love mode SAW for microorganism detection has also been studied [88]. The sensitivity of anti-IpaB antibody can be 3 µg/mL [121]. A biological warfare agent (BWA) sensor was studied as well and has a fast response to target the antigen [122].

Lab-on-a-chip devices have gained popularity in recent years. Acoustic sensors have great potential due to their portability, high sensitivity, cost efficiency and ease of fabrication [123]. More work needs to be done to transform these biological sensing applications into portable biosensors such as simplifying the signal processing circuit and solving the compatibility problem with CMOS technology to implement mass-production devices

### 2.3.2 Optical Sensing

#### 2.3.2.1 SPR Biosensors

SPR-based biosensors measure the refractive index near a sensor surface through the SPR phenomenon. They have a number of significant advantages over conventional sensors, including ultra-high refractive index sensitivity, fast sensor response, real-time detection, and a label-free technique. In addition, the advanced nature of SPR imaging (SPRi) technology not only retains the advantages of classical SPR sensing, but also allows the detection of target molecules on a biosensor chip to be visualised in real-time by using a charge-coupled devices (CCD) camera [124].

Many researchers have worked on developing SPR biosensors for studying various kinds of biological reactions and a number of successful reports have been published. The first application of a SPR biosensor was demonstrated in 1982 and the first commercial SPR sensor was introduced in 1990s [20] [19]. A schematic of a SPR sensing system is illustrated in Figure 2.15. In the widely used Kretschmann configuration, a monochromatic beam is focused onto the metal film with an incident angle  $\theta$ . At a certain  $\theta$ , where the SPs are excited, the reflected light intensity has a minimum. When analyte biomolecules bind to the sensing surface and thus change the effective refractive index of the detection area, the SPR angle will shift. This change in resonant angle can be monitored non-invasively in real-time by measuring the resonance signal against time. The signal is proportional to mass change on the metal surface.

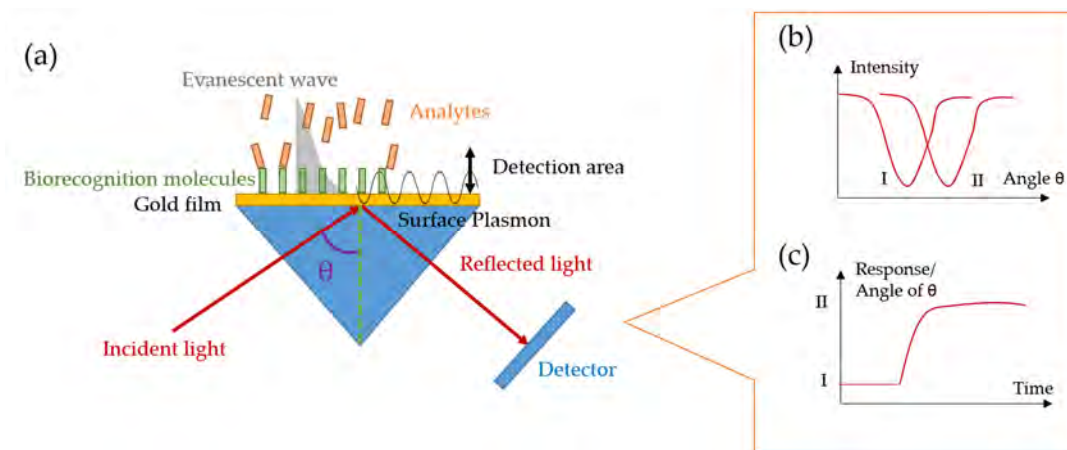


Figure 2.15 Schematic of the SPR biosensing method [125] (a): Kretschmann configuration of a commercial SPR biosensor system, analyte-biorecognition elements binding on SPR sensor surface and the effective refractive index changes in the detection area (b) spectrum of reflected light before (I) and after (II) the molecules attachment (refractive index change). (c) Transient response of the binding reaction.

SPR has been used as a powerful tool to study interactions between biomolecules based on affinity binding analysis of a variety of bonds, including antibody-antigen [126], ligand-receptor kinetics [127], enzyme-substrate reaction [128] and epitope mapping [129]. In SPR experiments, resonance or response units (RU) are used to describe the signal change, where 1 RU is equivalent to an angle shift of  $10^{-4}$  degree. The sensitivity unit can be presented as  $^{\circ}\text{RIU}^{-1}$ , RIU stands for refractive index unit.

### 2.3.2.2 LSPR Biosensors

While SPR biosensors use SPs excited at the interface between a dielectric and a gold film, LSPR biosensors take advantage of the LSPs excited in noble metal NPs.

The most common method for LSPR biosensing is the wavelength-shift measurement. As biological molecules are adsorbed on the sensing area, the LSPR extinction wavelength maximum,  $\lambda_{max}$ , is monitored as a function of change in the refractive index. Initial demonstrations were performed using streptavidin for antibiotin to biotin-functionalised nanoparticle arrays. A. Haes *et.al* conducted an experiment, where biotin was attached through a linker to the triangular silver nanoparticles on a borosilicate glass substrate. Transmission mode LSPR measurements were performed on streptavidin over a large concentration range [35]. Other biomolecule reactions such as antibody-antigen, nucleic acid hybridisation and protein-carbohydrate have been

detected using LSPR biosensing. It has also been used for biomedical applications, such as the detection of a biomarker for Alzheimer's disease [130].

Another method of LSPR biosensing utilises NP aggregation which often can be visualised with the naked eye. Single stranded DNA are modified with metal NPs that will accumulate during matching process and cause a colour change in the colloidal solution, by which this can detect the interaction between different DNA strands [131]. NP aggregation had also been demonstrated for protein recognition [132].

LSPR biosensors have also been integrated with multiplexing, microfluidic and optic fibre techniques to become more suitable for laboratory and clinical tools. Yu, Wang *et al.* and Yonzon *et al.* integrated different designs of metal NPs on chip and simultaneously monitored the LSPR peak shifts from multiple extinction spectra. The combination of LSPR and microfluidics enable the detection of very small sample volumes. Cheng *et al.* reported on the design of a fibre-based LSPR biosensor with gold nanospheres adsorbed to the end of the fibre [133]. K.Mitsui developed a fibre-based LSPR biosensor using a red light-emitting diode (LED) as the light source instead of a white light source. The reflection from the Au NPs on the fibre end-face was recorded by a photomultiplier tube [134] instead of a spectrometer. These approaches enable the LSPR measurement to be carried out in small sample volumes and even *in vivo*.

### 2.3.2.3 SPR vs LSPR Measurement Methods

Both SPR and LSPR spectroscopy can provide label-free and real-time kinetic data for binding processes. The first commercial SPR biosensor was launched by Biacore International AB in 1990 [135] and SPR biosensors have been widely used for almost two decades. Since the topic of LSPR has not been studied for as long as SPR, few LSPR biosensor devices have reached the commercial implementation stage. SPR and LSPR were compared by Svedendahl *et al.* using biotin-streptavidin binding [39]. SPR sensors exhibited large bulk refractive index sensitivities (3300 nm/RIU) while LSPR has a smaller bulk refractive index sensitivity (178 nm/RIU). However, since the electromagnetic field decay length of LSPR is 40-50 times shorter than that of the SPR sensor, the actual sensing volume of LSPR is very small. As a result, the response of the two techniques becomes comparable in biological applications when measuring short-

range changes in the refractive index owing to a biomolecular adsorption layer [34] [38]. Moreover, the gold covered area on the LSPR sensing surface is one-fourth of that on the SPR sensing surface, the sensitivity in ng/cm<sup>2</sup> is actually better in the LSPR case. Apart from the sensitivity similarity, LSPR holds more advantages compared to SPR. For LSPR sensors, the small size of the particles and the ability to be integrated with microfluidics allow detection of very low amounts of adsorbents. For SPR, a thick polymer capture layer or matrix is normally required and it needs to be suffused with the analyte to generate a detectable signal.

The required set-up for LSPR is simpler than the one for SPR as it does not need a prism for coupling. This makes LSPR sensors capable of miniaturisation. A home-built LSPR based system costs less than \$25,000, while a commercial SPR instrument costs ~\$200,000 [136]. The cost for LSPR spectroscopy equipment is likely to be reduced with further development of the technique and instrumentation. For example, replacing the white-light spectrometer with an LEDs plus a simple photodetector would dramatically reduce system cost [38].

## 2.4 Hybridisation of Optical and Acoustic Sensing

Optical and acoustic sensing techniques have applications in *in-situ*, label-free sensing and analysis of chemical and biological binding reactions [38] [137]. Both of them have applications leading to POC diagnosis techniques. As mentioned before, optical sensing techniques, such as SPR and LSPR, typically measure the change in the refractive index arising from the molecular adsorption on the metal surface thus measures the molecular mass (optical masses) of thin films adsorbed onto the noble metal [138]. Currently available optical technology does not generally allow for the detection of the conformation of an adsorbed analyte and the way it is bound to a surface.

In contrast, acoustic sensors record the acoustic mass, *i.e.* the sum of the mass of the deposited molecules and the mass of the solvent molecules trapped in the matrix of these deposited molecules [139]. For a given surface adsorption process, the comparison between the optical and acoustic mass can give, among other parameters, the degree of hydration (for aqueous solutions) of the adsorbed layer that often relates

well to the conformational properties such as size, shape, and elastic constants of the molecules in the formed layer [140] [140] [141] [142]. Consequently, valuable information can potentially be extracted from a measurement using this type of sensor. However, in cases when optical and acoustic experiments are conducted separately, the reliability of the extracted information (hydration degree or conformation information) heavily depends on the extent of the similarity of the experimental conditions (sample concentration, temperature, liquid flow, surface conditions, *etc.*) of the two sets of experiments [143].

Therefore, many attempts were made to combine optical and acoustic sensors. Rishpon *et al.* used a combination of ellipsometric, acoustic and electrochemical detection on a single surface to study the growth of a polyaniline film [144]. Kößlinger *et al.* combined a QCM with SPR and detected the binding of bovine serum albumin and antibodies to the sensor surface [145]. Studies had also taken advantage of both modalities to evaluate the thickness of polymer films [146] and biomolecule adsorption [147]. However, the optical and acoustic responses were measured sequentially on different devices, not at the same time on the same film. To eliminate the variations of the experimental conditions, a sensor that can record both the optical and acoustic signal simultaneously is essential.

Laschitsch *et. al* used a QCM with a corrugated gold electrode, which served as the optical coupling of a light beam in a SPR grating configuration set-up [148]. Such a technique was also used for studying interfacial behaviour of thin films formed either by solution adsorption [149] [150] or via an electrochemical polymerisation process [151] [1]. A hybridised sensor using a continuous thin film gold electrode on one side of a QCM sensor was also reported [143] [152]. Using the conventional Kretschmann configuration, SPR detection was performed by monitoring the variation in the angle of the reflected light from the electrode. This work was extended and used to determine the water content and thickness of protein layers, the lipid layer and DNA upon hybridisation [143] [153] [101], as well as protein-DNA binding and DNA replication [154]. A waveguide-coupled SPR integrated with a QCM sensor was reported by Shinbo *et. al.* [155]. The quartz substrate was acting as the waveguide core. This sensor

was used to study the thickness of different polymer films and the moisture absorption in PVA films.

Another approach was taken by combining a SH-SAW sensor with SPR in the Kretschmann configuration. The set-up used a smooth metal surface for simultaneous optical and acoustic detection [156]. This set-up was used to determine the water content and *in situ* thickness of human IgG upon adsorption onto a hydrophobically modified surface [147].

Due to the development of the LSPR technique and the advantages compared to SPR, high surface-sensitive nanoplasmonic sensors had been integrated with QCM sensors in order to investigate biomolecular adsorption processes. Dahlin *et al.* reported a synchronised nanoplasmonic and QCM sensing experiments, and highlighted the advantages of interpreting measurement data collected simultaneously by both measurement techniques in order to reveal conformational changes in polymers [62]. Jonsson *et al.* also conducted simultaneous nanoplasmonic and QCM-D sensing experiments in order to investigate vesicle adsorption and rupture on silica-coated surfaces as well as quantification of subsequent protein binding [157]. In addition, Larsson *et al.* reported combined LSPR and QCM-D measurements on silica-coated nanodisk arrays in order to also investigate vesicle adsorption and rupture to form silica-supported lipid bilayers (SLBs) as well as protein binding [158]. Ferhan *et al.* demonstrated the integration of QCM-D and a TiO<sub>2</sub> coated reflection-mode LSPR sensor. They used the device to study  $\alpha$ -helical peptide-mediated structural transformation of adsorbed vesicles into a supported lipid bilayer [159]. These investigations have demonstrated that quantitative extraction of physical parameters other than the amount of analyte proving that it is indeed possible to obtain with suitable combinations of acoustic and optical biosensor elements.

## 2.5 Summary

This chapter has introduced and discussed the background and previous work relevant to optical and acoustic technology with a particular emphasis on the field of biosensing. Both SAW streaming and SAW sensing have been presented. The developing trend of plasmonic sensing and acoustic sensing applications in POC testing has been demonstrated and the challenges have been discussed. Conventional commercial SPR and LSPR sensing have also been compared showing the advancement and promising future of LSPR sensors. Finally, the foundation work of the hybridisation of optical and acoustic technologies has been introduced presenting the developing trends and current challenges.

# 3. Methods

This chapter briefly describes the simulation, fabrication and characterisation methods used to design and engineer the plasmonic nanostructures and the quartz crystal microbalance (QCM). An overview of the finite-difference time-domain (FDTD) method is provided in the first section, followed by further discussion on Lumerical FDTD solutions simulation software, which was used to design and optimise the plasmonic structures prior to fabrication. This chapter also includes the micro- and nanofabrication techniques used for fabricating the devices. The fourth section outlines the spectroscopic measurement techniques that were used to characterise the fabricated device. The final part presents two QCM characterisation methods used in the thesis.

## 3.1 Finite-Difference Time-Domain

Finite-difference time-domain (FDTD) is a numerical calculation method widely used in modelling the interactions of electromagnetic (EM) waves with objects and the surrounding environment. In the Cartesian coordinate system, the whole computation space is divided into numerous cubic grids or meshes. The algorithm of FDTD uses the finite-difference (FD) approximations to calculate the fields in incremental steps through these grids [160]. The FDTD method is employed in this thesis to simulate the optical properties of plasmonic nanostructures. It is useful in designing and optimising structures prior to fabrication.

The FDTD algorithm was first proposed by Yee [160] in 1966, and employs the second-order central difference. The FDTD is applied to so-called Yee lattice as shown in Figure 3.1. The lattice space increments in the  $x$ -,  $y$ - and  $z$ -directions are given by  $\Delta x$ ,  $\Delta y$ ,  $\Delta z$ , respectively. The electric field components are assigned in the centre of each grid edge and their vector directions parallel with each edge. This corresponds to half integer separation between the different components. The magnetic field components are assigned at the centre of each grid face and their vector directions perpendicular to each face. In this staggered grid, every  $\vec{E}$  component is surrounded by four circulating  $\vec{H}$  component and every  $\vec{H}$  component is surrounded by four circulating  $\vec{E}$  components. The time increment is given by  $\Delta t$ .

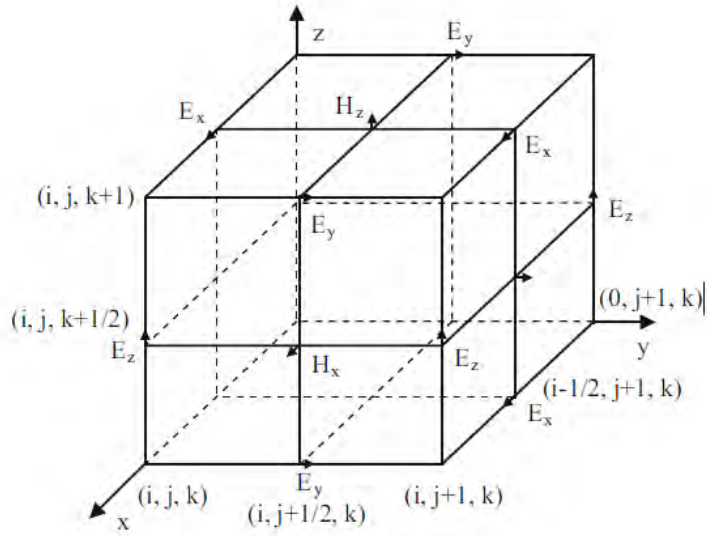


Figure 3.1 Illustration of the Yee cell geometry and the EM components in the cell.

The FDTD formulation initiates from the time domain Maxwell's curl equations. The curl equations can be rewritten as six coupled partial differential equations in the Cartesian coordinate system  $(x, y, z)$  as:

$$\frac{\partial H_x}{\partial t} = \frac{1}{\mu} \left[ \frac{\partial E_y}{\partial z} - \frac{\partial E_z}{\partial y} - \delta H_x \right] \quad 3.1$$

$$\frac{\partial H_y}{\partial t} = \frac{1}{\mu} \left[ \frac{\partial E_z}{\partial x} - \frac{\partial E_x}{\partial z} - \delta H_y \right] \quad 3.2$$

$$\frac{\partial H_z}{\partial t} = \frac{1}{\mu} \left[ \frac{\partial E_x}{\partial y} - \frac{\partial E_y}{\partial x} - \delta H_z \right] \quad 3.3$$

$$\frac{\partial E_x}{\partial t} = \frac{1}{\varepsilon} \left[ \frac{\partial H_z}{\partial y} - \frac{\partial H_y}{\partial z} - \delta E_x \right] \quad 3.4$$

$$\frac{\partial E_y}{\partial t} = \frac{1}{\varepsilon} \left[ \frac{\partial H_x}{\partial z} - \frac{\partial H_z}{\partial x} - \delta E_y \right] \quad 3.5$$

$$\frac{\partial E_z}{\partial t} = \frac{1}{\varepsilon} \left[ \frac{\partial H_y}{\partial x} - \frac{\partial H_x}{\partial y} - \delta E_z \right] \quad 3.6$$

where all symbols have their usual meanings as stated in Chapter 2. They are the basis of the FDTD algorithm for EM radiation, inference, and interaction with three-dimensional (3D) objects.

The space point in the coordinate system in Figure 3.1 is denoted as

$$(i, j, k) = (i\Delta x, j\Delta y, k\Delta z) \quad 3.7$$

and a function of space and time in the grid is defined as

$$F^n(i, j, k) = (i\Delta x, j\Delta y, k\Delta z, n\Delta t) \quad 3.8$$

where  $i, j, k$ , and  $n$  are integers. The space and time derivative can be expressed as:

$$\frac{\partial F^n(i, j, k)}{\partial x} = \frac{F^n(i, j, k) - F^n(i - \frac{1}{2}, j, k)}{\Delta x} \quad 3.9$$

$$\frac{\partial F^n(i, j, k)}{\partial t} = \frac{F^{n+\frac{1}{2}}(i, j, k) - F^{n-\frac{1}{2}}(i, j, k)}{\Delta t} \quad 3.10$$

In this manner, the electric field and the magnetic field values on the two grids are evaluated at alternate half time steps. Substituting these expressions into Equations 3.1-3.6, the sample of FDTD expression for EM field component can be expressed as:

$$\begin{aligned} & \frac{E_x^{n+\frac{1}{2}}(i, j, k) - E_x^{n-\frac{1}{2}}(i, j, k)}{\Delta t} \\ &= \frac{1}{\varepsilon(i, j, k)} \left( \frac{H_z^n(i, j + \frac{1}{2}, k) - H_z^n(i, j - \frac{1}{2}, k)}{\Delta y} \right. \\ & \quad \left. - \frac{H_y^n(i, j, k + \frac{1}{2}) - H_y^n(i, j, k - \frac{1}{2})}{\Delta z} \right) \end{aligned} \quad 3.11$$

$$\begin{aligned} & \frac{H_x^{n+1}(i, j, k + \frac{1}{2}) - H_x^n(i, j, k + \frac{1}{2})}{\Delta t} \\ &= \frac{1}{\mu(i, j, k + \frac{1}{2})} \left( \frac{E_y^{n+\frac{1}{2}}(i, j + \frac{1}{2}, k + \frac{1}{2}) - E_z^{n+\frac{1}{2}}(i, j - \frac{1}{2}, k + \frac{1}{2})}{\Delta y} \right. \\ & \quad \left. - \frac{E_y^{n+\frac{1}{2}}(i, j, k + 1) - E_y^{n+\frac{1}{2}}(i, j, k)}{\Delta z} \right) \end{aligned} \quad 3.12$$

After rearrangement, the  $E_x$  component at spatial position  $(i, j, k)$  and  $H_x$  component at spatial position  $(i, j, k + \frac{1}{2})$  are:

$$\begin{aligned}
E_x^{n+\frac{1}{2}}(i, j, k) = & E_x^{n-\frac{1}{2}}(i, j, k) \\
& + \frac{\Delta t}{\varepsilon(i, j, k)} \left( \frac{H_z^n(i, j + \frac{1}{2}, k) - H_z^n(i, j - \frac{1}{2}, k)}{\Delta y} \right. \\
& \left. - \frac{H_y^n(i, j, k + \frac{1}{2}) - H_y^n(i, j, k - \frac{1}{2})}{\Delta z} \right)
\end{aligned} \tag{3.13}$$

$$\begin{aligned}
H_x^{n+1}\left(i, j, k + \frac{1}{2}\right) = & H_x^n\left(i, j, k + \frac{1}{2}\right) \\
& + \frac{\Delta t}{\mu(i, j, k + \frac{1}{2})} \left( \frac{E_y^{n+\frac{1}{2}}\left(i, j + \frac{1}{2}, k + \frac{1}{2}\right) - E_z^{n+\frac{1}{2}}\left(i, j - \frac{1}{2}, k + \frac{1}{2}\right)}{\Delta y} \right. \\
& \left. - \frac{E_y^{n+\frac{1}{2}}(i, j, k + 1) - E_y^{n+\frac{1}{2}}(i, j, k)}{\Delta z} \right)
\end{aligned} \tag{3.14}$$

As shown above, it can be seen that the  $E_x$  component for any position at time step  $n + \frac{1}{2}$  can be calculated from  $E_x$  at time step  $n - \frac{1}{2}$  and the magnetic components of the neighbouring cells at time step  $n$ . These calculated  $E_x$  components at time step  $n + \frac{1}{2}$  can then be used to calculate the  $H_x$  at time step  $n + 1$ . Applying the leap-frog manner [161] calculation into the meshed region, the electric and magnetic field values on the two grids are evaluated at alternate half time steps. The EM field components at each point are calculated from previous stored data in an iterative way until the fields in the whole space are solved.

### 3.1.1 Lumerical FDTD Solutions

Lumerical FDTD Solutions software was used for the optical simulations in this thesis [162]. The 3D structures of the simulated target were modelled in a graphical computer aided design (CAD) environment. Using the software, simulations were executed and simulated data can be exported and analysed.

First, the simulation model is built and can consist of different materials. The dielectric properties of these materials can be defined in the material database, either selecting the predefined ones inside the simulation package or importing user-defined data. The materials can be defined using complex refractive index or complex permittivity data. This data can be defined over a specific wavelength range in order to incorporate

dispersive materials into the simulation. Some materials, such as lithium niobate in this thesis, whose refractive indices are not included in the software need to be defined manually in the material database.

Secondly, after building the simulation model and defining materials, a 3D simulation region with specific dimensions needs to be defined which is called the FDTD region. Its background index, meshing accuracy and boundary conditions need to be specified as follows:

- The mesh set in the FDTD region divides it into numerous finite volume cells corresponding to the Yee lattice. A finer mesh setting can offer higher calculation accuracy but also requires more memory and requires more computer resources, thus taking longer to process the calculation. If a finer meshing is needed for a certain layer or region, especially for structure variation within the mesh cells, a finer mesh region can be added which gives overriding meshing values in each axis (see Figure 3.2). This can give higher accuracy and with a smaller increase in memory consumption.

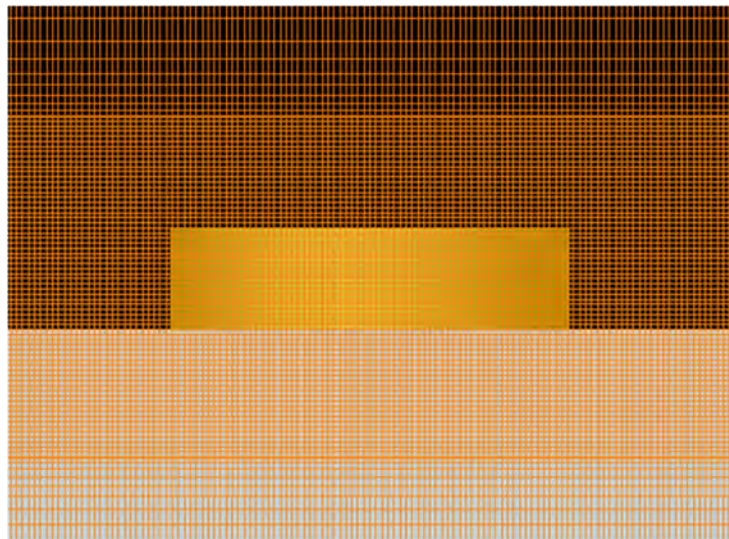


Figure 3.2 Simulation mesh in the x-z view. Finer mesh is defined in area of interest around the gold nanodisk to offer higher calculation accuracy.

- The boundary conditions depend on the features of the structure to be simulated and the type of simulation to be performed. Perfectly matched layers (PML) are designed to perfectly absorb scattered light so that no light is reflected back into the simulation region and cause erroneous simulation results. Since the

computation time will increase for a larger sized simulation regions, to minimise the simulation region, periodic boundary conditions can be used for large structures consisting of repeated unit cells. The computation time could be further reduced by using symmetric and anti-symmetric conditions at x- and y-axis when the simulated structure exhibits symmetry in xy-plane.

- The third step is the addition of the source and monitors. A broadband plane wave source is positioned inside the substrate to simulate light incident on the sample and to investigate the characteristics of the optical structures over a range of wavelengths. The polarisation of the wave source can also be modified. The outputs of the simulations are recorded by 2D frequency-domain field monitors. The field monitor is positioned on the opposite side of the optical structure (to the light source) to collect transmission spectra. As the FDTD method is used to calculate field data in the time domain, the field data was first recorded at each time step and then converted into the frequency domain using Fourier transform (FT). A field monitor can also be placed at the xz-plane to visualise the electric distribution around the plasmonic nanostructure at its cross section.

The script interface of Lumerical FDTD Solutions can be used for visualising the data. More complex analysis can also be done using the in-built scripting language. The software offers various analysis packages which can be added into the calculation process. Data can be extracted and transferred into other data processing software such as Matlab and Microsoft Office Excel for analysis and plotting. Simulation results can also be plotted inside the software and saved as JPEG images. The calculated data are exported and saved in a comma separated values (CSV) format.

## 3.2 Micro/nanofabrication

All devices presented in this Thesis were fabricated using the equipment available in the James Watt Nanofabrication Centre (JWNC). Detailed fabrication process flows will be described in the following chapters, with process-flow diagrams (Section 6.4). Here, some key techniques used to fabricate the devices are presented.

### 3.2.1 Metallisation

Thin metal film deposition was required for device fabrication and performed using physical-vapour deposition (PVD) by electron beam evaporation. Sputter-coating was occasionally used to deposit a thin layer of metal on structures and improve the contrast for scanning electron microscopy (SEM) by conducting away the accumulating charge in the dielectric layer.

Metal evaporation was mainly undertaken using a Plassys MEB 550S Electron Beam Evaporator, however a Plassys MEB 400S Electron Beam Evaporator was used when the former machine was unavailable [163]. In the vacuum chamber, an electron beam is used to heat metal to the point where it melts and evaporation occurs. The evaporated metal then passes through the chamber and reaches the substrate surface where it condenses and gradually builds up a film to the required thickness. In this thesis, the devices are typically composed of gold structures. Due to the poor adhesion of gold to substrate surface, a thin layer of titanium was required as an intermediate layer to improve adhesion.

An ion beam sputtering tool was occasionally used prior to imaging in the SEM [164]. In the argon gas filled chamber, ionised plasma is formed between two electrodes. Argon ions then strike a palladium/gold target and the metal atoms are ejected and coat the sample. As this technique is destructive, it was used infrequently.

### 3.2.2 Lithography

Lithography is the branch of techniques used to define structures in the fabrication process. The lithographic method employed to fabricate the devices in this thesis are electron beam lithography (EBL) and photolithography. EBL was used for small features where a higher resolution is required ( $<1 \mu\text{m}$  feature size) and photolithography was used for large patterns that don't require a high resolution and alignment accuracy ( $>1 \mu\text{m}$  feature size). The throughput of photolithography is higher than EBL in most cases which was also considered when determining the appropriate method.

#### 3.2.2.1 Photolithography

Photolithography uses light at ultraviolet (UV) wavelengths to expose a light sensitive resist, known as a photoresist. A Suss Microtec Mask Aligner 6 (MA6) photolithography tool was used for the photolithography process presented in this thesis [165]. The 350 W mercury vapour lamp in the MA6 exhibits well-defined spectral peaks at UV wavelengths (~365nm). The photolithography process using the MA6 tool uses a shadow printing technique and is described as follows.

First, a sample is spin coated with photoresist. Secondly, the photomask with the pattern to be transferred is loaded in to the MA6 along with the sample. The photomask pattern is composed of transparent and opaque regions so that UV light can pass through the transparent regions and expose the photoresist beneath that area. Finally, the sample and photomask are positioned close to each other and the photoresist is exposed under UV light, thereby transferring the pattern on the photomask into the resist. A 50  $\mu\text{m}$  gap was set between the mask and the resist during exposure, which could avoid issues of dust damaging the mask when brought into contact with the photoresist at the expense of a decreased resolution due to diffraction effects.

For positive resists, such as Microposit S1818 photoresist used in this thesis, the exposed regions change chemical structure and become soluble to a solution known as a developer. The unexposed regions remain insoluble such that after development the leftover resist forms the pattern. For negative resists, the exposed region becomes less soluble, and the unexposed region is removed during developing process. The resist profiles for both positive and negative resists after exposure and development are illustrated in Figure 3.3.

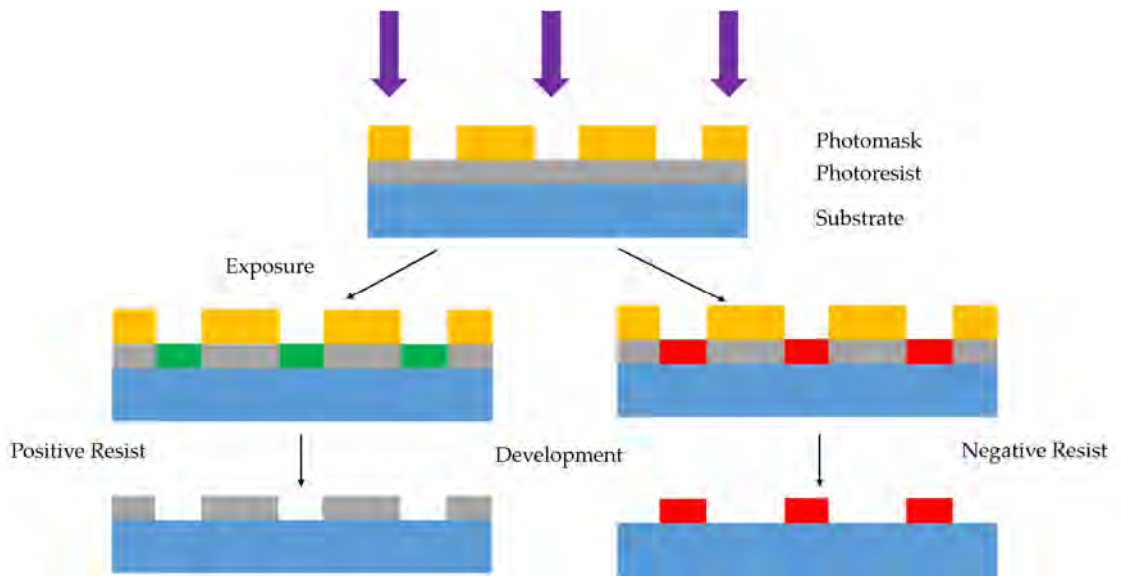


Figure 3.3 Illustration of the positive and negative photoresist profiles after exposure and development.

Photomasks were fabricated by Compugraphics [166] using EBL and subsequent processing. The custom designed pattern features are fabricated in a chromium film on a fused silica substrate. Photomasks can be reused, therefore making photolithography a low cost and high throughput technology. The resolution of a photolithography system is limited by the wavelength of light and therefore it is challenging to create features on a scale that is less than  $1\ \mu\text{m}$  without using resolution enhancement methods or considering different lithographic techniques. The requirement to fabricate new photomasks for any new patterns also means that it is not simple to frequently change patterns between samples, as was required for the development of the optical devices presented in this thesis.

### 3.2.2.2 Electron Beam Lithography

The tool used for EBL was the JWNC's Vistec VB6 Ultra High Resolution Extra Wide Field (UHR EWF). It uses a direct write method, where an electron beam is focussed on to the electron sensitive resist and traces out the required patterns. Similar to the photoresists described previously, electron beam resists are polymers that are sensitive to the electrons radiation and can be removed by a specific chemical solvent (developer) after exposure. The electron beam resist used to fabricate the devices presented in this thesis is poly methyl methacrylate (PMMA). A schematic of the EBL system is shown in Figure 3.4 [163].

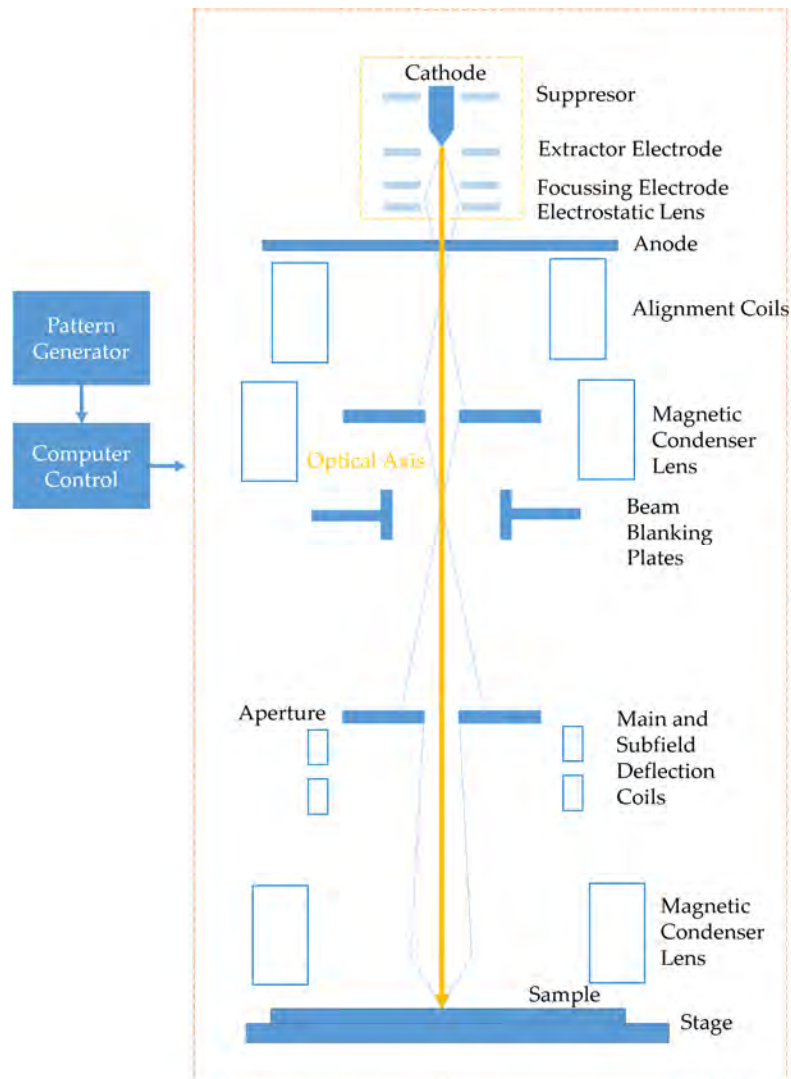


Figure 3.4 Schematic of the EBL tool. At the top of the figure, the components of the electron gun unit are illustrated inside the yellow square. The subsequent components along the optical axis are also illustrated.

The EBL tool consists of an electron gun, beam focusing components, sample stage, vacuum and pumping system. In the Vistec VB6, the electron beam is generated in the electron gun using thermal field emission. The suppressor is an electron lens used to prevent thermionic emission from the tip shank and ensure that only electrons generated at the cathode tip are emitted. A large electric field is formed between the extractor and the tip, and electrons are accelerated from the cathode surface. The focussing electrode is used to control beam focussing. The beam is then controlled using magnetic fields generated by the alignment coils so that it is central and remains on-axis with the optical axis. The electrostatic lens and the first magnetic condenser lens are used to maintain a constant current density and beam focus at the sample surface

whilst the diameter of the beam can be controlled. Beam blanking plates are used to turn the beam off by deflecting it away from the optical axis. Apertures are used to limit the divergence of the electron beam throughout the column. Beneath it, a series of lenses are used to focus the beam on the substrate. The second magnetic condenser lens focusses the electron beam on to the sample at the bottom of the column. The Vistec VB6 uses the vector scanning method, which only rasters the beam over regions where the resist is to be exposed and therefore can save a significant amount of processing time.

First, Mentor Graphics L-Edit CAD software was used to draw the patterns to be exposure on to the resist. The completed design file was exported in the GDSII file format.

Secondly, the GDSII file was imported into the Beamer software and the patterns were ‘fractured’ into rectangles and trapezoids, which are the unit blocks for patterning with the EBL tool. Fracturing also separates the pattern into main fields and sub fields. Main fields are accessed by mechanical movement of the sample stage. Smaller subfields in each main field are accessed using the main deflection coils and the beam is controlled within each subfield using the subfield deflection coils to expose the resist and write the rectangle and trapezoid shapes that compose the pattern.

Thirdly, using Belle software, the layout of fractured patterns on the substrate is set and some crucial parameters are defined to control the EBL process. These include beam spot size, resolution and variable resolution unit (VRU). To write the pattern, the electron beam exposes a spot on a grid, then moves on to the next spot, until the shape is completed. The beam step size, is illustrated in Figure 3.5 and is given by Equation 3.15.

$$\text{Beam Step Size} = \text{VRU} \times \text{resolution} \quad 3.15$$

A larger beam step size means that the distance between the exposure points (blue dots in Figure 3.5) are larger. To ensure that the resist is fully exposed, in most cases the VRU needs to be set so that the beam step size is smaller than the beam spot size.

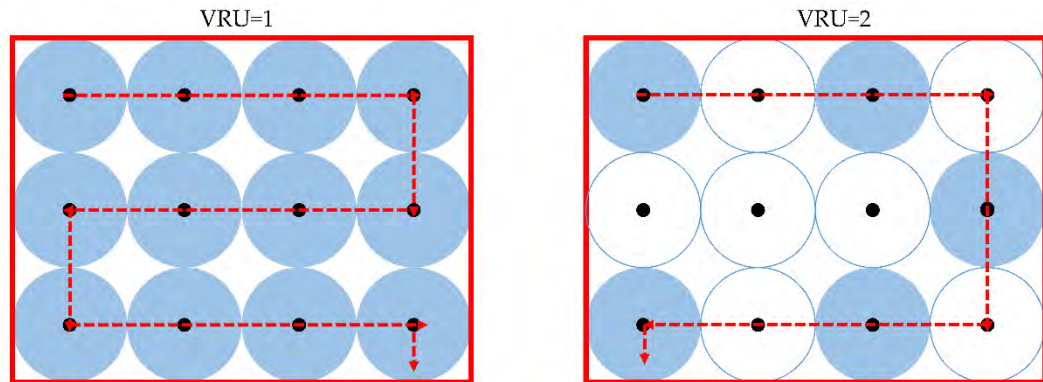


Figure 3.5 The illustration of the variable resolution unit (VRU) and beam step size.

It is also important to control the dose of the electron beam incident on the resist surface. Dose is given in terms of micro Coulombs per square centimetre ( $\mu\text{C}/\text{cm}^2$ ). It is necessary to perform a dose test before fabricating new structures as various aspects such as feature size and substrate type can impact the exposure result. On a dose test sample, small test patterns are fabricated over a range of different doses. After inspection under SEM, the required dose can be selected for fabricating large patterns.

Electrons are scattered by the molecules inside the resist and substrate, including both forward in the resist layer and backward scattering from the substrate. Those scattered electrons travel through the resist laterally and expose the adjacent area, thus effectively enlarging the exposed pattern size, which give rise to the so-called “proximity effect”. To avoid the consequence of this effect, relevant corrections need to be carried out.

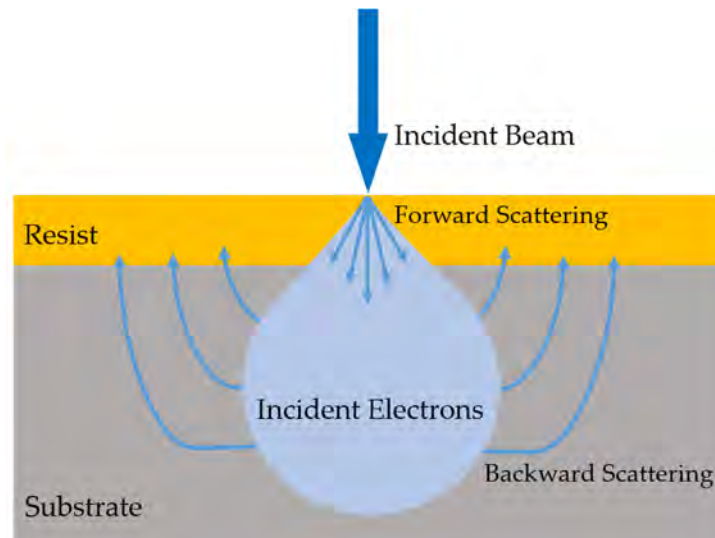


Figure 3.6, Electrons scattering by the resist. The light blue sector indicates the exposed area in the resist layer and the profile of incident electrons inside the substrate. Generally, the lower incident energy leads to a larger forward scattering area. Such an exposed area ranges from tens of nanometres even up to microns in lateral size, which depends on the beam energy, resist thickness, feature size and so on [167].

EBL offers improvement in resolution compared with photolithography, which is essential for the fabrication of plasmonic nanostructures in this thesis. It is also simple to redesign structures between different samples without fabricating new photomasks. However, EBL can be significantly slower than photolithography and much more expensive when considering mass production. It is therefore often necessary to compromise on certain features, such as total surface area to be patterned, to ensure writing can be completed in a reasonable time. In this thesis, the 'proximity effect' is used to reduce the patterning time, which will be described in Chapter 4.

### 3.2.3 Lift-off

Lift-off is a method of pattern transfer. During the process, the metal is deposited over the surface of developed resist, and then the remaining resist along with the surplus metal are removed to leave the desired pattern on the substrate. It is commonplace to use a bilayer of resist for lift-off. For EBL, a more electron-beam-sensitive PMMA with lower molecular weight is used as bottom layer while a PMMA with higher molecular weight and lower sensitive serves as top resist. After development, there will be an undercut in the bottom resist, which ensures discontinuity between the metal deposited on the resist and on the substrate. This can overcome problems associated with a non-

vertical resist profile, or metal being deposited on the resist sidewalls. The lift off process using a bilayer of resist is illustrated in Figure 3.7.

For photolithography, the top layer resist used in this thesis is a positive photoresist Microposit S1818 which is used to define the pattern. The bottom layer resist is MicroChem lift-off resist (LOR) which is not sensitive to the light. LOR has a higher dissolution rate than the exposed photoresist in Microposit MF-319 developer and gives the undercut for lift-off process.



Figure 3.7 Lift off process flow. After development of the resist bilayer, metal is deposited on the sample surface. The resist and surplus metal is then removed to leave the patterned metal on the substrate.

#### 3.2.4 Annealing

Post deposition annealing method was adopted for LSPR gold nanostructures on  $\text{SiO}_2$  samples. Melting of the metal nanostructures at high temperature will remove the fabrication imperfections to obtain better performance. For this purpose, a furnace tool (as seen in Figure 3.8) was used. The furnace consists of a temperature control unit and a tube oven which allows nitrogen to flow from one end to the other, forming an inert atmosphere. The fabricated sample was fixed by a quartz boat and placed inside the nitrogen flowing tube. In this thesis, a thermal annealing at  $600\text{ }^\circ\text{C}$  for 3 hrs was performed [168] on the fabricated sample, with detailed results presented in Section 4.1.3.

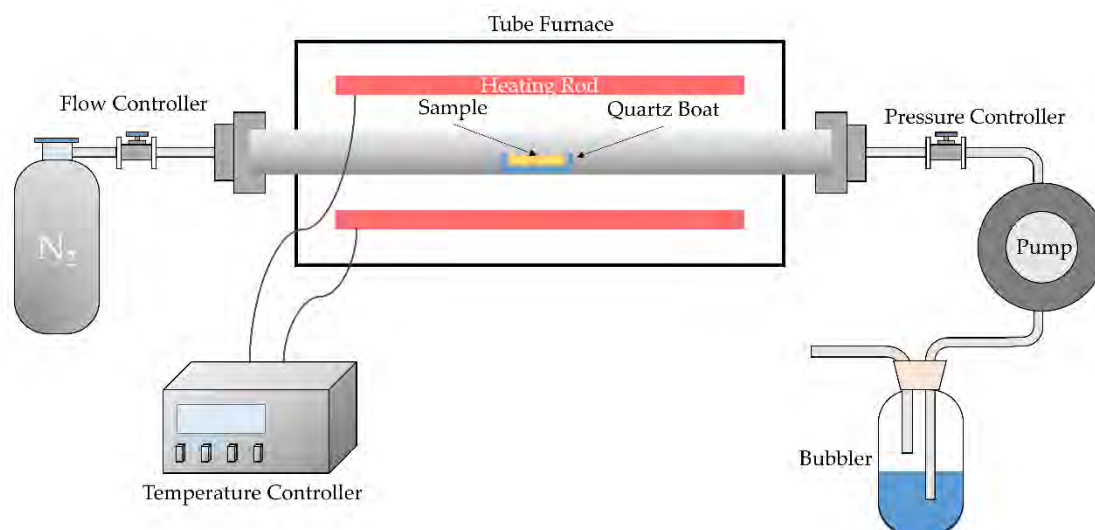


Figure 3.8 Schematic diagram of the Carbolite Gero Limited tube furnace

### 3.3 Chemical and Biological Modification of Sensor Surface

To carry out the immunoassay, a self-assembled monolayer (SAM) of 3-aminopropyltriethoxysilane (APTES) was functionalised on sample surface. Then a carboxylate group is functionalised and activated ready for coupling to antibodies. HCl and NaOH was used to adjust the pH value of the solutions during the surface functionalisation process.

1. First the sample needs to be clean and activated by 150 W oxygen plasma for 1min. This oxidises the gold surface and generates hydroxyl groups. As soon as the plasma activation is finished, 1mL of 10% in ethanol APTES was pipetted onto the sample surface and incubated at room temperature overnight in a fume hood. During this step, a monolayer of APTES develops over the chip (Figure 3.9). The chip surface is then cleaned with ethanol several times to remove any non-specific binding molecules. Non-specific binding refers to the molecules binding to sites other than the target of interest. It can easily lead to misinterpretation of results, and should therefore be avoided in any immunoassay.

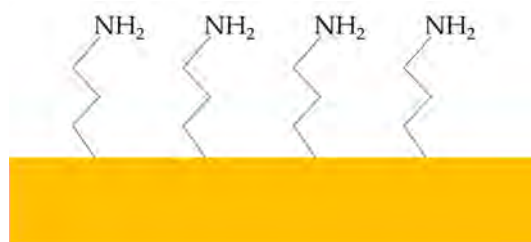


Figure 3.9 After the first step, amine groups are generated on gold surface.

2. One end of succinic acid is activated in solution to form the carboxylic acid group that is ready to react with the amine group on the sample surface. Sulfo-NHS (10.6 mM), EDC-HCl (40.7 mM), Succinic acid (400mM) were mixed in phosphate buffer (PBS) with a pH value of 7.4. The pH value of the mixture should be 4~5.
3. Take 100  $\mu$ l of the solution prepared in last step and dilute with 900  $\mu$ l of PBS (pH 9), the pH of the solution should be just above 7. Then 10  $\mu$ l aliquots of this solution were taken, placed on the sample surface and left for 2 hrs at room temperature. The reaction mixture was then removed and the sample surface is washed with PBS. After this step, the sensor surface is functionalised with a carboxylate groups as shown in Figure 3.10.

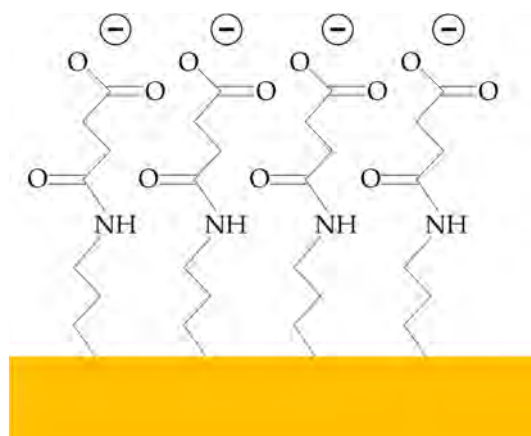


Figure 3.10 After step3, a carboxylate group is generated.

4. 10  $\mu$ l aliquots of a solution of EDC-HCl (40.7mM) and Sulfo-NHS (10.6mM) in PBS buffer (pH 6) is place on the sample surface and left at room temperature for 2 hours. This is the solution used to activate a carboxylic acid group. The sample is then washed with PBS buffer and the surface is now ready for reaction

with amines. Antibodies usually have a number of amine groups that can be attached to the functionalised layer as seen in Figure 3.11.

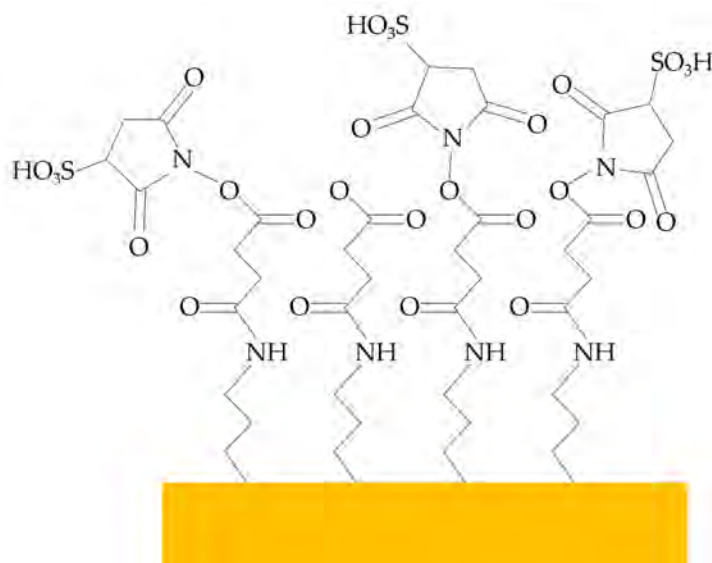


Figure 3.11 After step 4, the functionalised layer on the gold surface is ready for reaction with amines.

### 3.4 Spectral Characterisation

The transmission spectra of the optical devices were measured by microspectrophotometers in the spectral region from 400 nm to 1  $\mu\text{m}$ . The Angstrom Sun Technologies TFProbe MSP300 microspectrophotometer was used for the measurements in Chapter 4 and Chapter 5 and Foster & Freeman ffTA microspectrophotometer was used for the measurements in Chapter 6. The microspectrophotometers consist of a microscope, capable of operation in transmission or reflection mode, combined with dispersive optics and a charge-coupled device (CCD) detector for spectral measurement. The measurements were conducted in transmission mode, where the optical devices are illuminated from beneath using an unpolarised white light halogen lamp source. The transmitted light is collected through the objective lens and then detected by the sensor. In the Angstrom Sun Technologies TFProbe MSP300 microspectrophotometer, a polarisation analyser is embedded and placed after the microscope objectives.

The operation for both tools are basically the same. First, a baseline (reference) measurement was carried out to calibrate the sensor. Transmission measurements were performed to acquire the spectrum from the white light source. Another measurement

was performed when the light source was shut off to acquire a measure of the dark current. When these initial calibration steps were completed, the optical device was placed on the microscope stage and aligned. The transmission spectrum from the plasmonic nanostructures can then be acquired, and the dark background elimination and white light normalisation steps are carried out using software. The normalised transmission spectrum is displayed after acquisition and can be exported for further analysis, as can be found in Chapter 4, 5 and 6.

### 3.5 QCM Characterisation

QCM characterisation in this thesis was undertaken using two different techniques: vector network analyser (VNA) characterisation and frequency comparing circuit.

#### 3.5.1 VNA Characterisation

The acoustic phenomena can be described by electrical circuits by means of the electromechanical analogy. The electromechanical analogy maps forces onto voltages, and speeds onto currents. Electrical engineers have designed the “equivalent circuit” model for QCM (Figure 3.12). The properties of this equivalent circuit can be characterised by a vector network analyser (VNA) so that the QCM can be completely characterised. For the case of a two-terminal device such as a QCM sensor, the voltage incident on and reflected from the load can be measured by the vector network analyser (VNA) as a function of frequency. From these basic measurements, all electrical quantities that characterise the load can be found including impedance and the quality factor. [169] The impedance of the QCM is related to the electrical energy dissipation which is useful information in liquid phase measurements. The quality factor (Q-factor) can be expressed as a ratio of the resonance frequency and the full width at half maximum of the quadrature component of the resonance spectrum of quartz (see Figure 6.2 in Section 6.2). It is the ratio of energy input into the resonator divided by energy lost in the resonator per oscillation cycle.

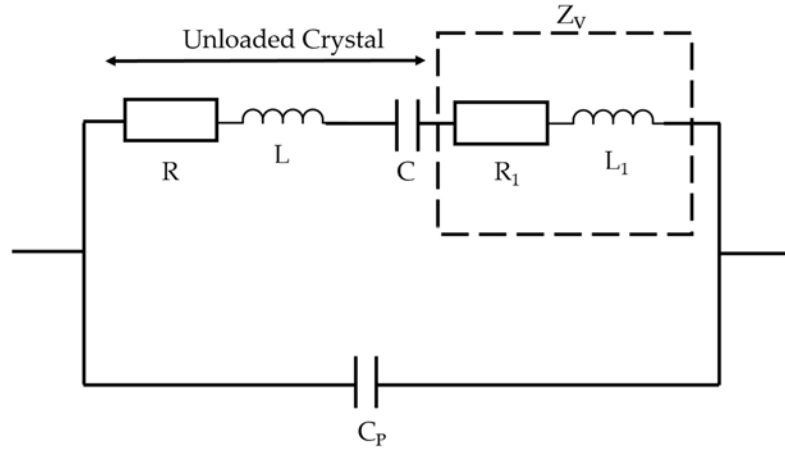


Figure 3.12 Equivalent circuit model of QCM.  $R$  represents the energy loss mostly arising from viscous effects.  $L$  represents the initial mass/motional inertia of the system,  $C$  represents the mechanical elasticity of the quartz, and  $C_p$  determines the admittance away from resonance and consists of the capacitance of the quartz between the electrodes and the parasitic capacitance of the crystal fixture. The adsorbed load onto the crystal surface, which is described using impedance  $Z_v$ , can be described by the additional elements  $R_1$  and  $L_1$ , a measure of energy dissipation in the film and mass loading, respectively.

The VNA used in this thesis is Agilent E5072B which is costly and sophisticated. For the frequency measurements, it was replaced by an in-house made circuit which is low-cost and has the potential of miniaturisation.

### 3.5.2 PCB Design for QCM Frequency Measurement

A printed circuit board (PCB), Figure 3.13, was made in-house and used to measure the frequency decrease of the working QCM in the surface binding process. It consists of (1) two crystal oscillator circuits, each of whose outputs go to separate Schmitt trigger inverters; (2) a dual D flip-flop which accepts the output of the Schmitt trigger inverters. These flip-flops are connected to measure the frequency difference between the two oscillators and output this difference to (3) an optical isolator whose purpose is to isolate the frequency-difference circuitry from the external interference [170].

The crystal oscillator circuits are labelled as “Reference” and “Working”. The working crystal oscillator was tuned to 5MHz with an LC-network since it often oscillates in a different mode than the desired fundamental mode. The frequency  $f_0$  of a LC resonant circuit is

$$f_0 = \frac{1}{2\pi\sqrt{LC}} \quad 3.16$$

The aforementioned problem did not occur with the reference circuit.

The six oscillator circuit inverters were in the same transistor-transistor logic (TTL) 7404 HEX inverter package. The TTL 7414 Schmitt trigger inverters, inserted before the 7474 dual D edge-triggered flip-flop are used for stabilising the frequency differentiating performance.

The reference crystal output was used as the clock pulse of the first flip-flop while the working crystal was sent into the data channel. Both pre-set (PR) and clear (CLR) inputs of the package were disabled. The second flip-flop served as an output buffer. This configuration yields the absolute value of the difference in frequency between the reference and working crystal. To better understand the working principle of the TTL circuitry, a simulated waveform can be found in Appendix. The TTL circuitry and the optical isolator were powered by four 1.5 V batteries joint in series. LM1117MP Voltage Regulator was used to convert and stabilise the batteries voltage from ~6V to 5V. The output side of the optically isolated gate was powered by a supply separate from that of the main circuit. The output was sent to an oscilloscope (Tektronix TDS2000C) for frequency measurements. A schematic of the detail PCB design can be found in Appendix.

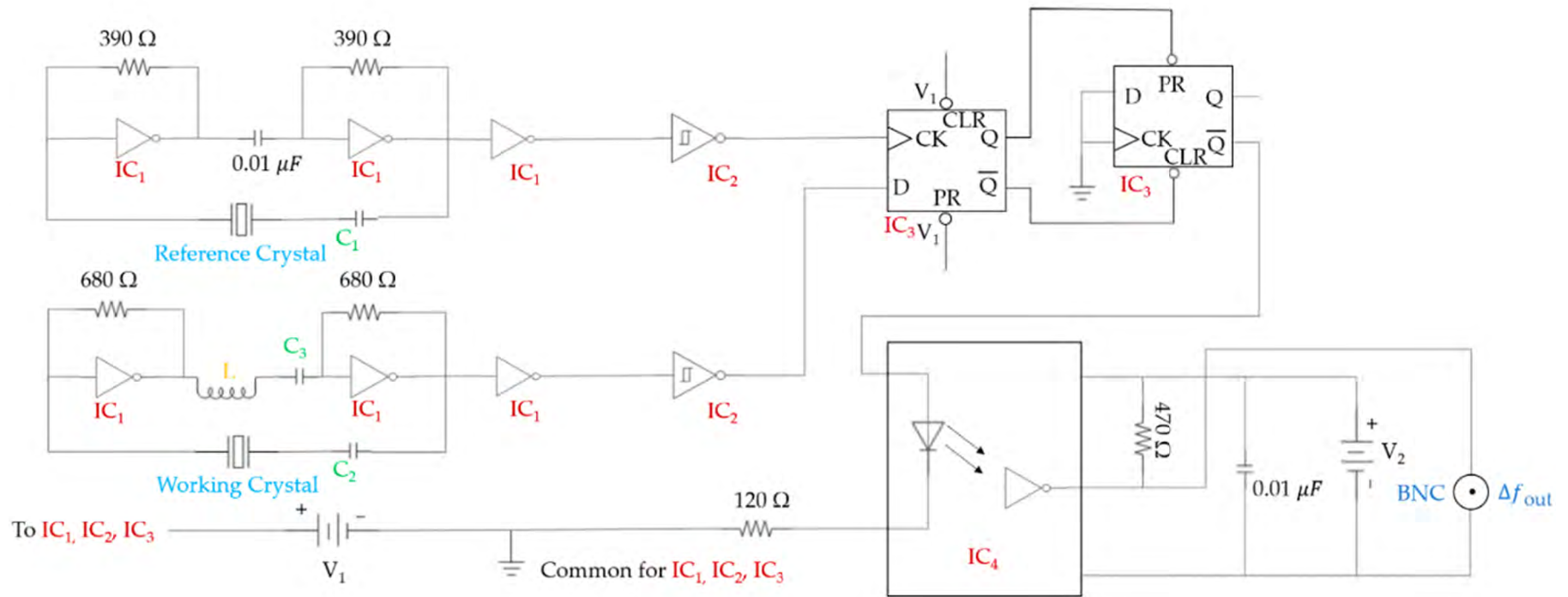


Figure 3.13 Separate reference and working QCMs with related frequency difference and isolator circuitry: IC<sub>1</sub> = 1/6 7404D Bipolar Hex Inverter; IC<sub>2</sub> = 1/6 7414D Hex Schmitt Trigger Inverter; IC<sub>3</sub> = 1/2 7474D Dual D type Flip-flop; IC<sub>4</sub> = 1/2 HCPL0600R2 Input Logic Gate Output Optocoupler; C<sub>1</sub> = 20 pF silver mica; C<sub>2</sub> = 50 pF silver mica; C<sub>3</sub> = 100pF ceramic; and L = 10 μH. V<sub>1</sub> and V<sub>2</sub> are separate 5 V power supplies[170].

### 3.6 Summary

This chapter has provided an overview of the techniques underlying the design, fabrication and characterisation of the plasmonic nanostructures and QCM that are presented in this thesis. A brief description of the FDTD technique has been outlined with a focus on the simulation software Lumerical FDTD Solutions. All of the optical devices presented in this thesis have been simulated using Lumerical FDTD Solutions and it has been an essential tool in the design and optimisation of the optical materials. The fabrication techniques employed to make the devices presented in this work have also been outlined in this chapter. Similar processing steps were used for plasmonic nanostructures on SiO<sub>2</sub> and LiNbO<sub>3</sub>. However, there are some variations in processing, which are due to the relative size scales of the nanostructures and the different material properties of the substrate. Further detail on the specifics of the fabrication processes for the individual devices will be explored in subsequent chapters. The procedures of molecular surface modification have been presented. Two microspectrophotometry tools used in this thesis have been described. Finally, two measurement methods for QCM were presented. The following chapters will demonstrate how these tools and techniques have been used to produce and characterise the optic and acoustic devices.

# 4. Localised Surface Plasmon Resonance from Gold Nanodisks on SiO<sub>2</sub> for Biosensing

## 4.1 Introduction

The previous chapters have covered the theory of plasmonics, localised surface plasmon polariton resonance (LSPR) and the advantage of using this sharp resonance for biosensing. Theoretically, LSPR is possible in any metal, alloy or semiconductor with a large negative real dielectric constant ( $\epsilon_1$ ) and small imaginary dielectric constant ( $\epsilon_2$ ). Since the application targets for the plasmonic nanodisks described in this thesis are for biosensing, gold was chosen due to its biocompatibility.

In this chapter, the design, simulation, fabrication and characterisation of the gold nanodisk arrays and the tunable properties of their plasmon resonance are presented. The purpose of this set of experiments is not only to show the optical resonances of the LSPR nanostructures can be designed as but also to optimise the nanostructure for better resolution and large sensitivity. A study has also been done to investigate the effect of post fabrication annealing to the nanostructures. The bulk refractive index sensitivity of different nanodisk array designs have been characterised using varying concentration of glycerine-water solution. By comparing the sensing performance, one of twelve designs shows the best performance according to simulation and experimental results. Following the above explorations, biomolecule binding experiment was performed regarding the use of LSPR nanodisks for biomolecular sensing.

### 4.1.1 Design and Simulation

The simulation setup for the gold nanodisk array is as follows: a broadband plane wave source spanning from 400 nm – 1  $\mu$ m was incident on the 60 nm thick gold nanodisk array, which was on top of a semi-infinite SiO<sub>2</sub> substrate as shown in Figure 4.1(b). A transmission monitor was placed inside the dielectric material which was above the gold

nanodisk array. A mesh override region (placed inside the simulation region) was inserted near the gold nanodisk to set a maximum mesh size of 5 nm in the  $x$ ,  $y$ , and  $z$  directions, highlighted by the purple box in Figure 4.1(b). A frequency-domain field profile monitor was placed in the same region to monitor the field power distribution near the metal. Anti-symmetric and symmetric boundary conditions were used in  $x$  and  $y$ , respectively, to form the periodic array. Perfectly matched layer (PML) boundaries were used in the  $z$  direction. The Johnson and Christy's gold [171] and Palik's  $\text{SiO}_2$  [172] models were used to define the optical properties of the materials in the wavelength range of 300 nm to 1000 nm. The dataset for both models were included in the software (Figure 4.2).

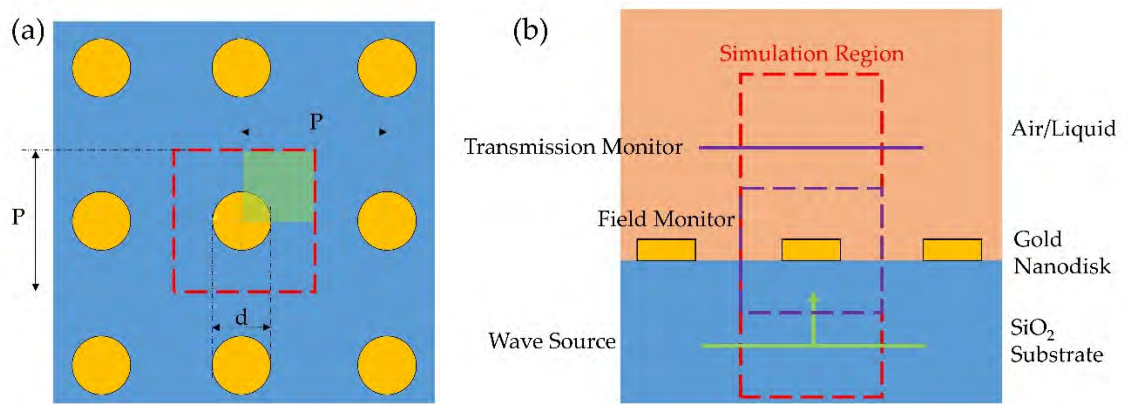


Figure 4.1 Schematic of the simulated gold nanodisk array structure. (a) Top-down view of the simulated gold nanodisks. The green region is the simulated region. The red dash line encloses the unit cell of the nanodisk array structure.  $P$  denotes the array period and  $d$  denotes the disk diameter. (b) Cross section of the simulated gold nanodisks. The red dash line encloses the simulated unit cell.

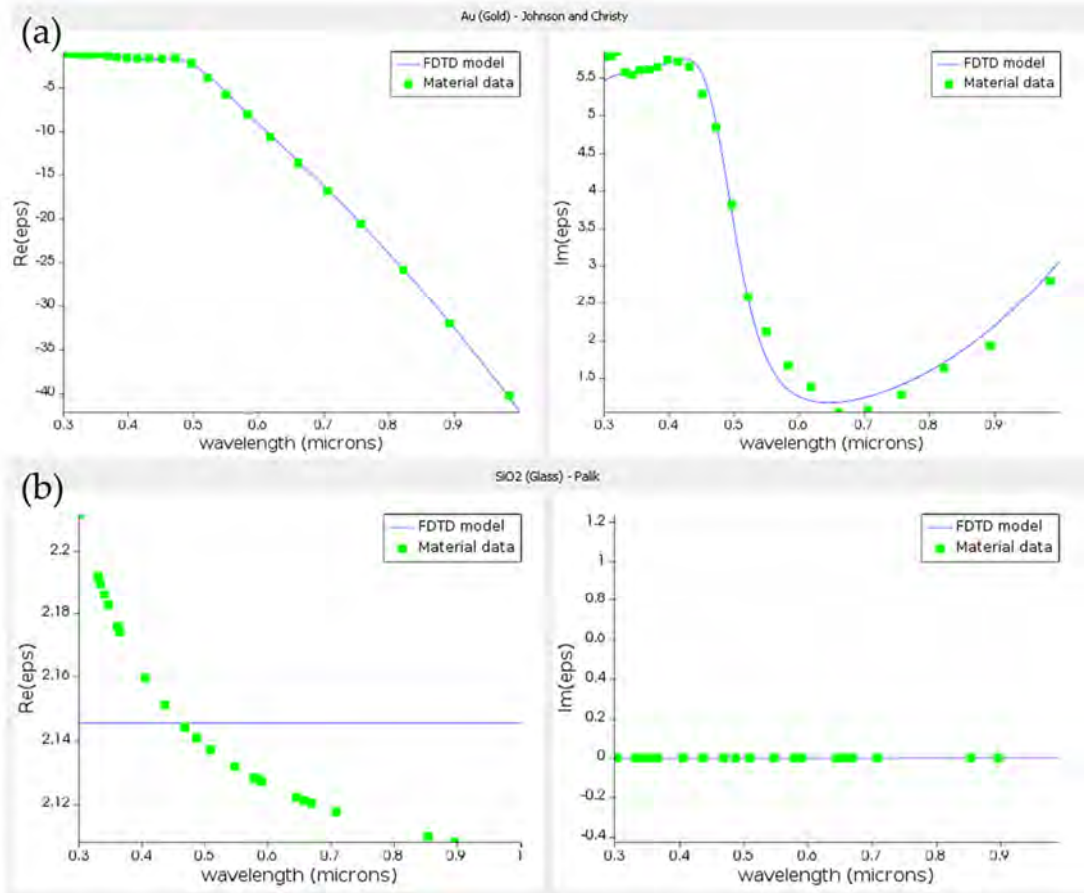


Figure 4.2 Real and imaginary parts of the dielectric constant and the material fits generated by the software. (a) gold, Johnson and Christy model (b) SiO<sub>2</sub> Palik model

Schematic of the top-down view of gold nanodisks on SiO<sub>2</sub> simulation model is shown in Figure 4.1 (a). The nanodisk period is given by  $P$  and the nanodisk diameter is given by  $d$ . Table 4.1 assigns the various combinations of  $P$  and  $d$ . The simulated transmission spectra from the 12 nanodisk array designs groups A-D are shown in Figure 4.3 (a-d).

Design group	Period, $P$ (nm)	Diameter, $d$ (nm)	Design group	Period, $P$ (nm)	Diameter, $d$ (nm)
A1	300	100	C1	500	100
A2	300	150	C2	500	150
A3	300	200	C3	500	200
B1	450	100	D1	600	150
B2	450	150	D2	600	200
B3	450	200	D3	600	300

Table 4.1: 12 designs are divided into four groups (A-D) with each group having a fixed period  $P$  and varying diameter  $d$ .

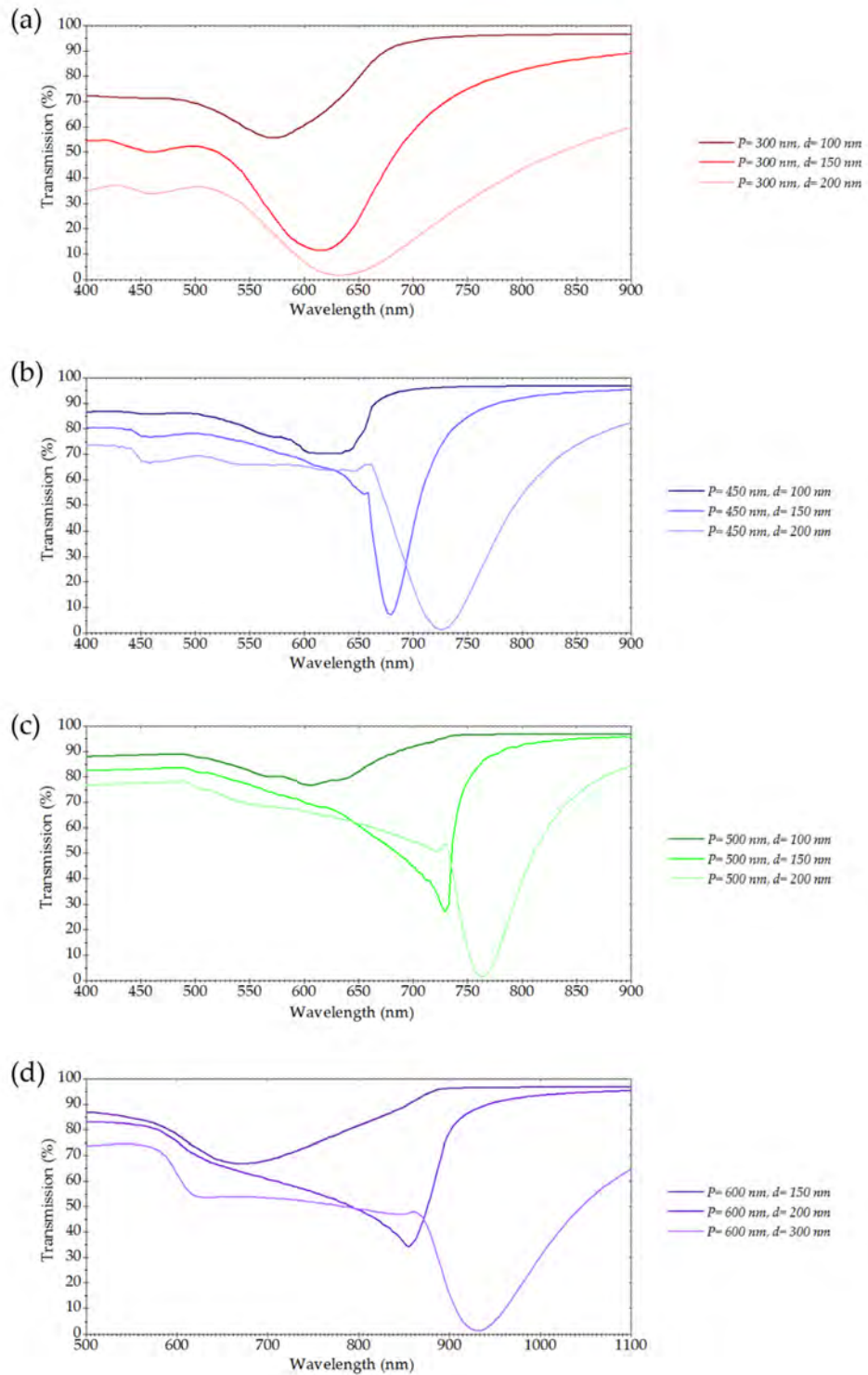


Figure 4.3: Simulation results from the 12 nanodisk array designs. The individual transmission spectra are shown in (a)-(d). The legend denotes the nanodisk period,  $P$ , and the nanodisk diameter,  $d$ .

From the simulation results presented in Figure 4.3, it is observed that scaling the array period from 300 nm to 600 nm yields a resonance wavelength shift from ~600 nm to

~900 nm. With  $P$  remaining constant, an increase in  $d$  resulted in a stronger resonance but at the expense of lower transmission at the wavelength other than the resonant wavelength and a red shift at the transmission peak. The spectrum also broadens as  $d$  increases.

#### 4.1.2 Fabrication

Gold nanodisks were fabricated on the surface of a 500  $\mu\text{m}$  thick, 20 mm  $\times$  20 mm borosilicate glass slide. The sample was cleaned by sequentially immersing into OptiClear, acetone, and isopropyl alcohol (IPA) for 5mins (each time) with ultrasonic agitation. The substrate was then rinsed thoroughly with deionised (DI) water and dried using a nitrogen gun. The sample was then spin coated with 12% diluted PMMA 2010 at 5000 rpm spinning speed, and hotplate baked at 156°C to yield a ~550 nm, thickness. Another layer of 4% PMMA 2041 was spin coated on top at 5000 rpm spinning speed, after 6min of hotplate baking at 156°C, it yields a ~115 nm thickness as shown in Figure 4.4. A 20 nm Aluminium (Al) charge conduction layer was deposited on top of the resist layer before the e-beam exposure to conduct away the redundant electrons. The nanodisk array pattern was transferred on the resist layer using EBL with a 1 nm resolution, a beam spot size of 4 nm and the VRU was set at 5.

The nanodisk array was fabricated over a square area of 1 mm by 1 mm in order to obtain accurate alignment using the microspectrophotometer for measurement. For the 12 different designs, this needs a lengthy EBL patterning process. Therefore, the nanodisk array fabrication was optimised prior to fabrication of the final sample for measurement. This was carried out by performing dose tests, to determine the optimum dose for the final fabricated device. The dose test consisted of a smaller nanodisk array pattern within a square region, typically of side length 100  $\mu\text{m}$ , repeated 9 times for a range of electron beam doses (200  $\mu\text{C}/\text{cm}^2$  to 600  $\mu\text{C}/\text{cm}^2$ ). The best dose could be determined by acquiring scanning electron microscope (SEM) images after fabrication, and by observing the transmission spectra from the different designs using the transmission microspectrophotometer.

After the EBL patterning, the sample was first immersed into MF-CD26 developer for ~2 minutes until the Al conduction layer was removed and the sample was transparent.

The sample was placed in a beaker of IPA for 30 seconds before drying with the nitrogen gun. The sample was developed in solution of 2:1- MIBK (Methyl isobutyl ketone): IPA, at 23 °C for 45 seconds and then rinsed in IPA for 30 seconds.

After drying the sample with the nitrogen gun, any residual resist left in the developed area was removed by using oxygen (O<sub>2</sub>) plasma etch in PlasmaFab 505 Barrel Asher at 80 W for 30 seconds and was immediately transferred to Plassys for metal evaporation. A 3 nm adhesion layer of titanium (Ti) followed by a 60 nm Au layer was then evaporated on to the sample surface. The Ti layer is important for adhesion of the Au film. A lift-off procedure was carried out immediately after the metal evaporation. The resist and surplus metal was removed by placing the sample in 50°C hot acetone for more than 2 hours before rinsed by IPA. A schematic illustrating the complete fabrication procedure is shown in Figure 4.4.

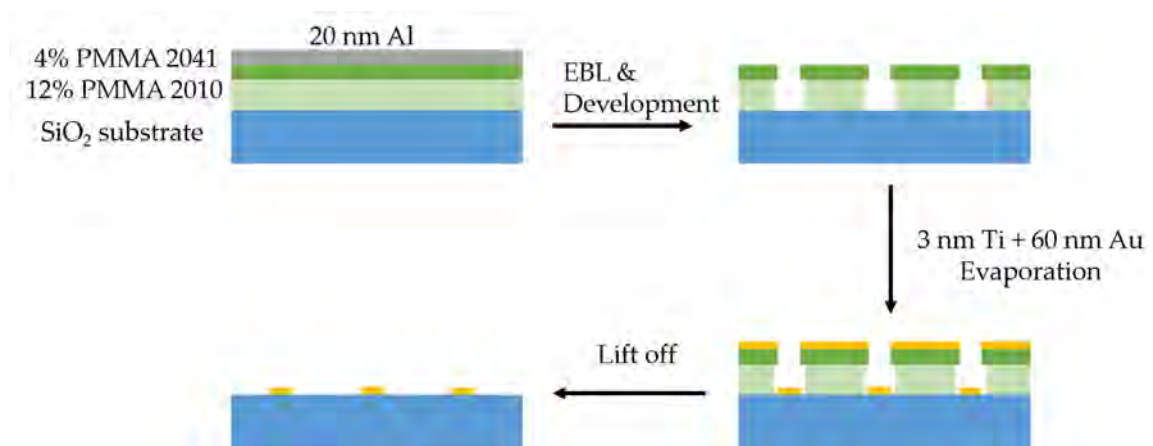


Figure 4.4: Illustration of gold nanodisk array fabrication process flow.

At the end of the fabrication run, the nanodisks are then inspected in the Scanning Electron Microscope (SEM). SEM images can yield valuable information about the fabrication quality along with the highlighting the accuracy of fabricated geometries to the simulated ones. Since the glass substrate is non-conductive, a ~9 nm metal layer is sputtered over the dose test sample surface to reduce the charging effect before SEM imaging.

#### 4.1.2.1 Reducing the Ebeam Time

A large array of gold nanodisks is needed for accurate alignment for measurement and the EBL time is normally ~ 1.1 hours for the 1 mm ×1 mm area. As EBL is a costly technique, some optimisation has been done to reduce the e-beam time for writing nanodisks. A

method proposed by Iain Macgilp from Kelvin Nanotechnology Limited was tested and significantly reduced the e-beam time for writing the nanodisks.

The VB6 writes the pattern at a certain frequency. The beam moves from point to point and to generate small pixels. The size of a pixel depends on both the beam current and how long the exposure-time is. One pixel is written in every clock cycle, so a high operating frequency will lead to dots being written faster. A settle time is added after exposing every pixel to ensure the beam is steady and in the correct position before exposing. The settle time is equivalent to the exposure-time of 3 pixels when writing nano disks.

Writing an array of nano-dots can take a lot of time due to the settle time of VB6 since for every dot it needs a larger number of pixels. By using a combination of smaller pixels in the centre of the dots (Figure 4.5), the 3 pixels' worth of delay time becomes less significant. The overlapping between each pixel means the beam step sized is reduced compared to the conventional method and therefore invariably will increase the operating frequency of the e-beam, reducing the writing time.

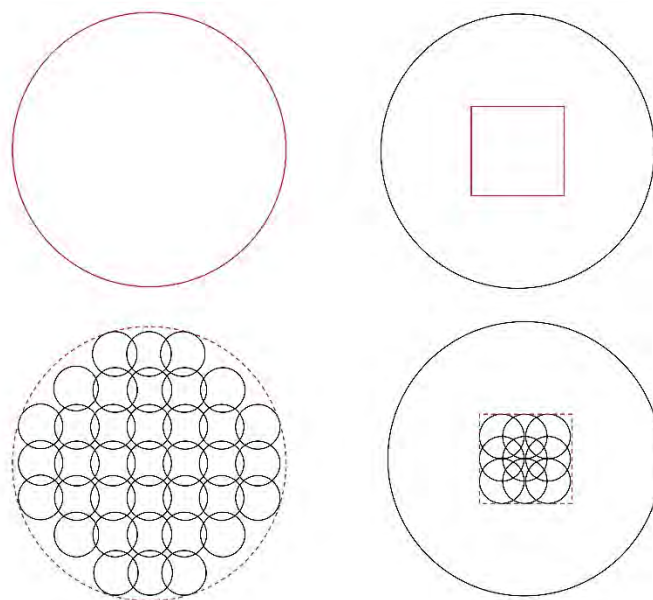


Figure 4.5 Illustration of the conventional writing method (left hand side) and the multipixel method (right hand side) for a single nanodot. The red circle and square represent the nanodot designed in L-edit. The conventional writing methods writes the whole nanodots area using a large number of beam points which needs more settle time. The multipixel method only writes a small area in centre of the nanodot and expose the whole area using back scattering effect.

The time reduction makes the multi-pixel approach an attractive method for writing arrays of nanodisks. This approach was tested on designs with  $P$  of 300nm, 450 nm and 500 nm, instead of disks with different values of  $d$ . The pattern was designed as 10 nm\*10 nm square arrays in the Mentor Graphics mask designing software: L-edit. A beam current of 64 nA was used as it shows a better dot circularity compared to 128 nA. The VRU was set as 2 to reduce the beam step size. A rather large dose ranging from 200000 to 600000  $\mu\text{C}/\text{cm}^2$  was used for the dose test. For the 1 mm  $\times$ 1 mm nanodisk array, dose 480000  $\mu\text{C}/\text{cm}^2$  was selected for writing the design B3 and the e-beam time reduced significantly from 1.1 hour to 0.5 hour.

#### 4.1.3 Post Fabrication Annealing

The nanodisks are fabricated by the lift-off process. Due to the nature of this process, it leads to a bumpy surface and a rough side-wall profile as seen in Figure 4.6(a). In order to smoothen the disks, post fabrication annealing was done for these devices. By annealing these devices for three hours at 600 °C [168] in an atmosphere of  $\text{N}_2$ , improvements were observed in both, structure roughness and transmission response, which will be described in next section.

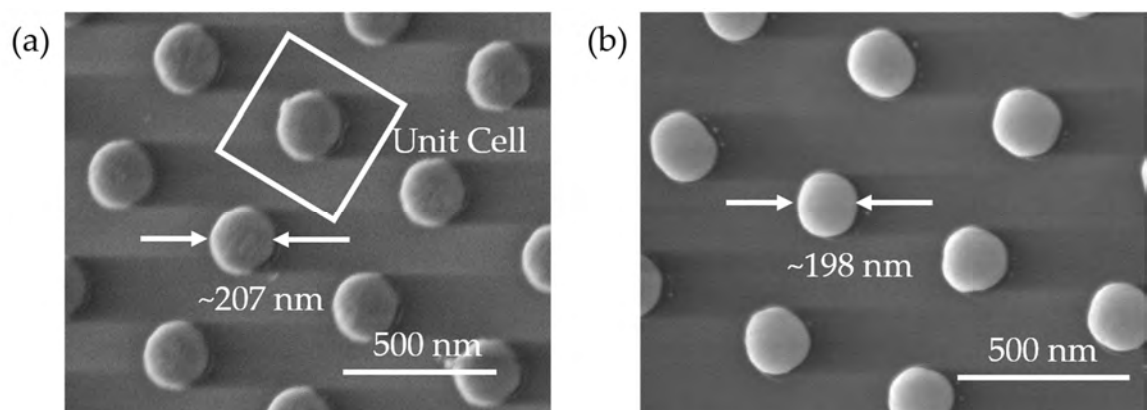


Figure 4.6 Top-view SEM images of the Au nanodisks in design B3 (a) before and (b) after thermal annealing. The nanodisks exhibit smooth side walls and slightly smaller diameters (~9 nm smaller).

#### 4.1.4 Characterisation Results and Discussion

Optical characterisation was performed by using the TFProbe MSP 300 microspectrophotometer. The objective has a numerical aperture (NA) of 0.1 and magnification of 4 $\times$ . The measurement area is 100  $\mu\text{m}$  in diameter.

#### 4.1.4.1 Effect of the Post Fabrication Annealing

The sensing performance of the plasmonic nanostructure sensors is usually judged by a figure of merit (FOM) defined as the shift of resonance wavelength per RIU (sensitivity) divided by the full-width at half-maximum (FWHM,  $\Gamma$ ) of the LSPR resonance peak [29]. The FOM strongly influences the performance of using the plasmonic LSPR filters for sensing applications as it depends on the ability with which the spectral shifts can be differentiated [173]. To optimise this FOM, the FWHM of the LSPR transmission dip (extinction peak) should be as narrow as possible. This also benefits the transmission measurement carried out using a fixed wavelength light source [174], as it can improve the intensity variation thus improve the resolution as seen in Figure 4.7.

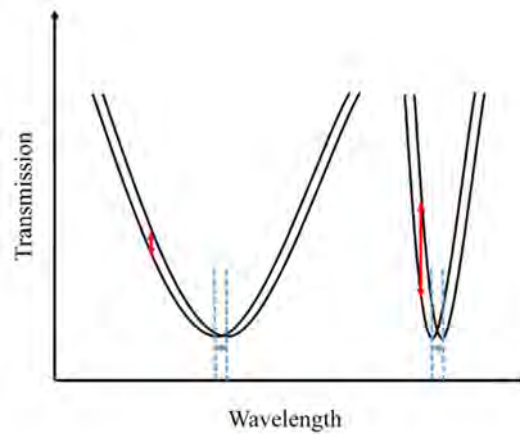


Figure 4.7 Illustration of how the linewidth of the LSPR transmission peak affects the resolution and the intensity measurement conducted at a fixed wavelength. The resonant wavelength shift is the same and caused by same refractive index change.

The fabrication imperfections broaden the FWHM of the LSPR spectra of the nanodisk arrays. As illustrated in Figure 4.6 (a), an SEM image reveals that the fabricated nanodisks of design B3 exhibit imperfection around the edge and on the disk surface. These attributed to a larger scattering causing broadening in the transmission dip (extinction peak). After annealing, the LSPR transmission dip of the nanodisk arrays becomes much narrower compared to the unannealed fabricated nanodisk arrays, as is demonstrated in Figure 4.8. Also, the size of the nanodisk reduced slightly ( $\sim 9$  nm) which results in the resonant dip position shifted blue shifted to lower wavelengths.

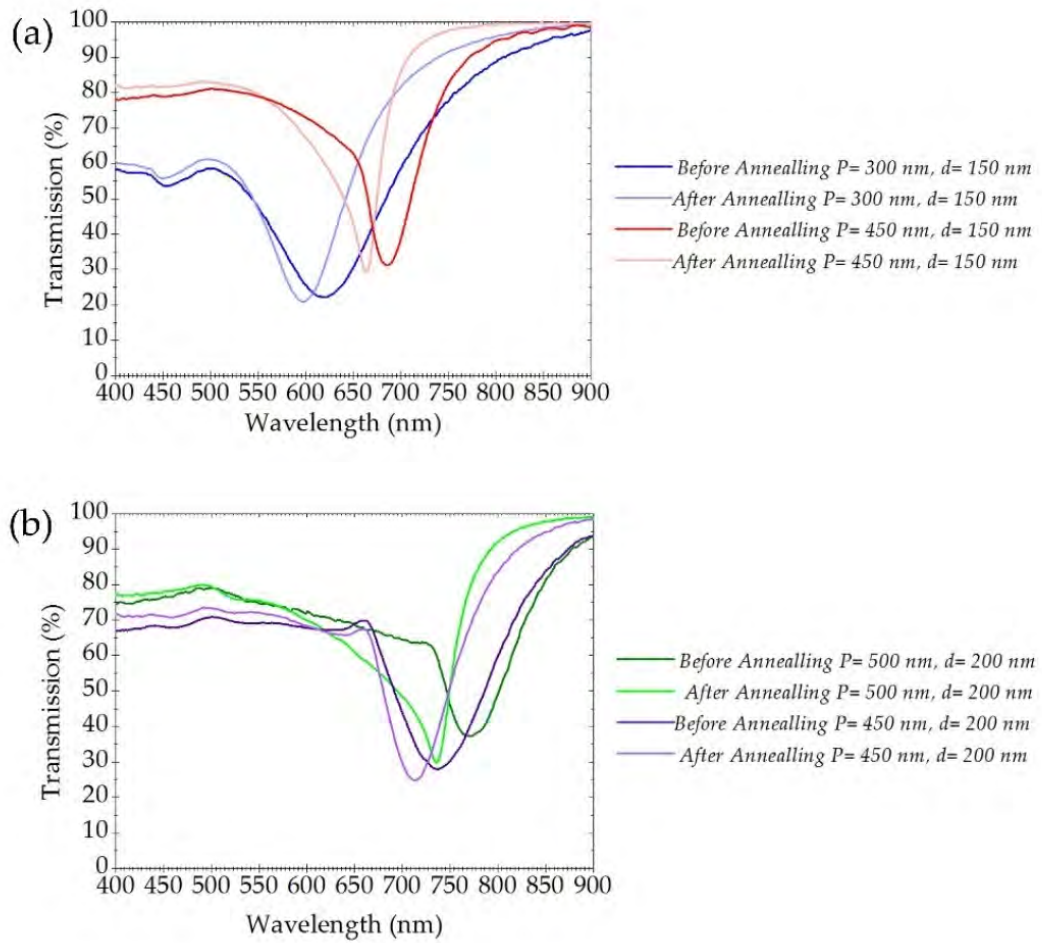


Figure 4.8 The experimental extinction spectra corresponding to the designs A2, B2, B3 and C3. The extinction peaks of all the annealed samples exhibit narrower linewidth, larger transmission dip and a blue shift at the resonant wavelength.

#### 4.1.4.1 Effect of Array Period ( $P$ ) on the LSPR

Figure 4.9 (a-d) shows the SEM images of the nanodisk array designs: A3, B3, C3 and D2, respectively. These four arrays maintain the same  $d$  of 200 nm, but  $P$  were varied 300 nm (A3), 450 nm (B3), 500 nm (C3), and 600 nm (D2).

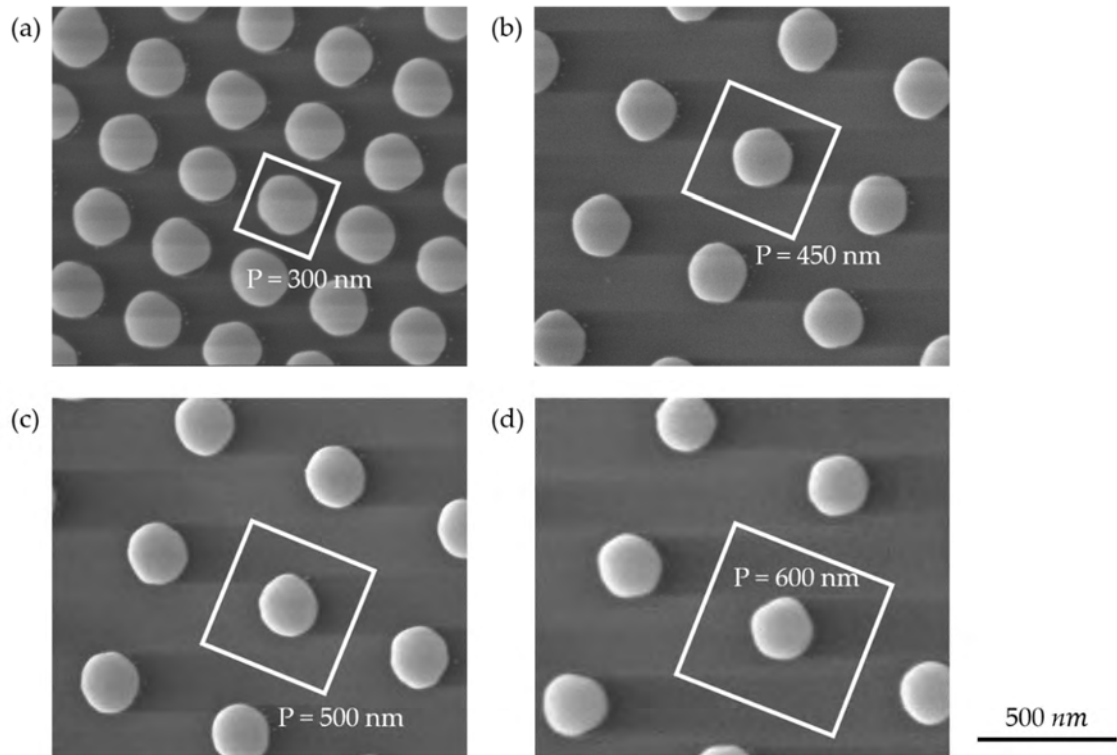


Figure 4.9 SEM images of the gold nanodisk array designs A3, B3, C3, D2. The diameter of the nanodisks were the same as 200 nm (with a standard deviation of 4 nm, 5 nanodisks of each design had been randomly chosen for calculating dimensional errors).

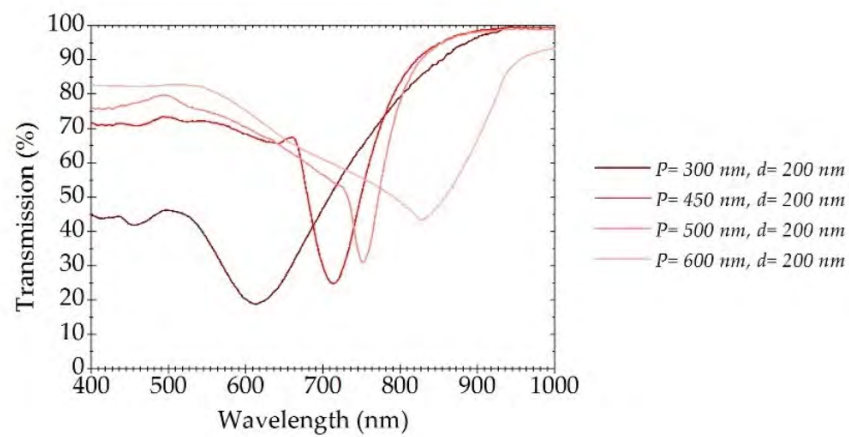


Figure 4.10 The transmission spectra of the fabricated gold nanodisk array designs that correspond to A3, B3, C3, D2 in Figure 4.9.

Figure 4.10 shows the corresponding experimentally measured plots of the normalised transmission spectra of gold nanodisk arrays (design A3, B3, C3, D2). The characterisation range was in the visible from 400 nm to 1000 nm. The measured resonance wavelength of design A3 was at 613 nm, of array design B3 was at 714 nm, of design C3 was at 752 nm,

and for design D2 was at 838 nm, respectively. The corresponding simulated resonance peaks of arrays A3, B3, C3 and D2 were 634 nm, 726 nm, 764 nm and 869 nm respectively. Figure 4.11 shows the dispersion relationship of resonance wavelength with respect to  $P$  for designs A3, B3, C3 and D2 obtained from simulations and experiments. The transmission spectra are due to the LSPR excitation *i.e.* dependent on the geometry of the nanodisks as well as interference from adjacent nanodisks. In this set of experiments, the diameters of the nanodisks were identical, therefore, plasmonic resonances from such nanodisk arrays can be attributed to the change of array period, thus altering the optical interference condition. Similar theory has been proposed by Haynes et al. wherein the spectral red shift was attributed to radiative dipole interaction between the nanoparticles and retardation effects [175].

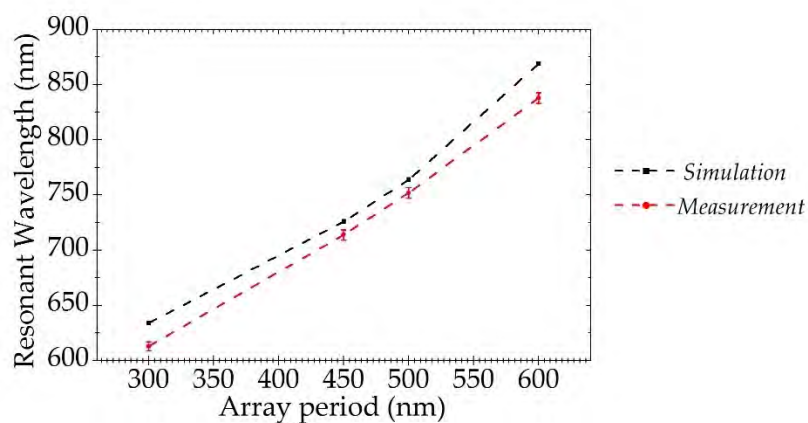


Figure 4.11 Dispersion relationships of plasmonic resonance with array period of four nanodisk designs. The measured and simulated data are drawn with red and black markers respectively. Error bars are added based on the standard deviation of three different measurements on three different samples. The deviations are caused by fabrication imperfection and measurement error.

#### 4.1.4.2 Effect of Nanodisk Diameter ( $d$ ) on the Resonance

Although plasmonic resonance of nanodisk arrays can be manipulated by changing period, the diameter of the nanodisks also affect the resonant wavelength due to LSPR. As seen in the previous section, there is often a slight variation in the fabricated nanodisks size when compared to those designed using L-edit for EBL. This can result from several factors such as variations in development temperature or time and electron beam dose. To investigate this effect, six designs of nanodisk arrays were simulated, fabricated and characterised. The array period was set as 450 nm for this set of experiments whereas  $d$

was varied from 150 nm to 240 nm. The simulated and experimental transmission spectra are shown in Figure 4.12(a) and (b), respectively.

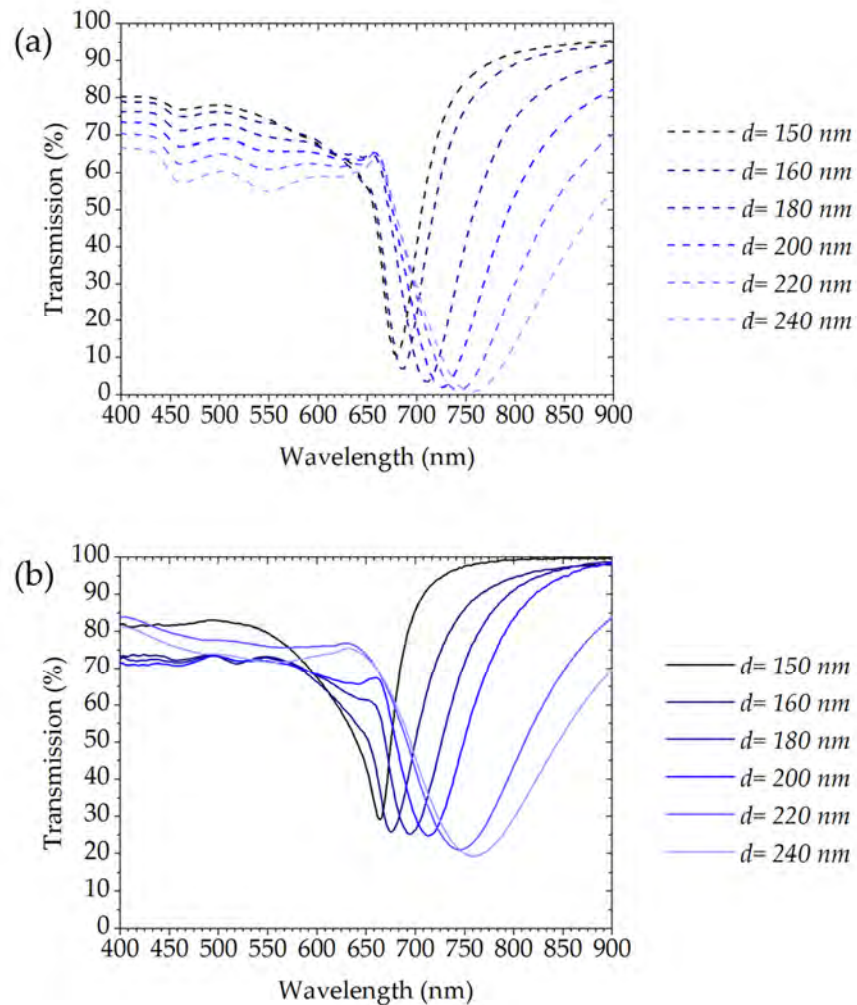


Figure 4.12 Transmission spectra of gold nanodisk array. (a) Simulated spectra. (b) Measured spectra. Both simulated and measured wavelengths were in the range 400 nm to 900 nm.

The transmission intensity decreases with larger diameter due to the larger fill factor. The small rise before the transmission starts to decrease only shows up with large nanodisk diameters. This suggests that it can be related to the electric field coupling between the adjacent nanodisks. This rise is also related to the array period. Figure 4.13 shows the simulation results for the gold nanodisk array with a fixed nanodisk diameter ( $d=200$  nm) and varying array periods from 460 nm to 490 nm. The wavelength of the small rise increases with a larger array period. This anomalous resonance weakens when the ratio

of diameter and array period gets larger, which also suggests that it is related to the electric field coupling between the adjacent nanodisks [175].

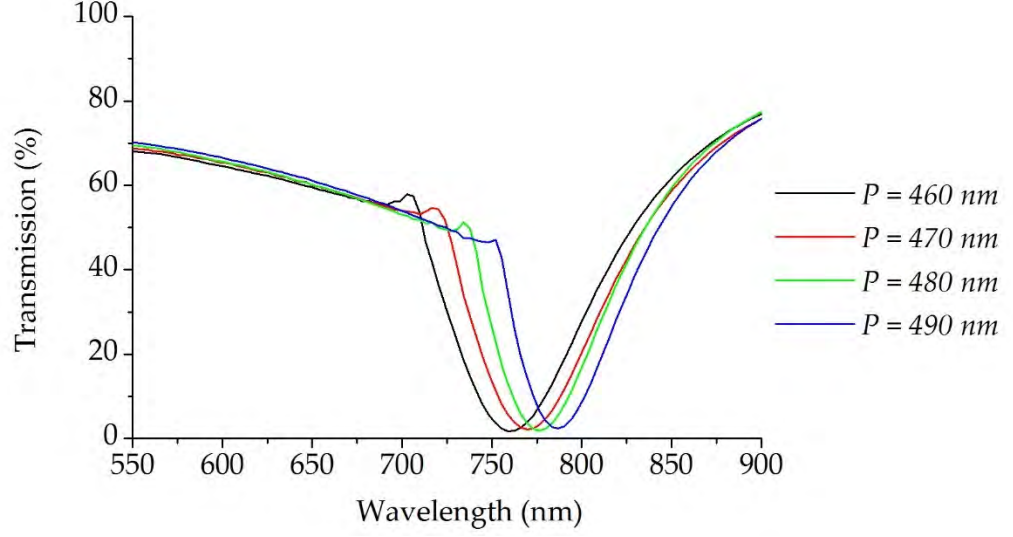


Figure 4.13 Simulated transmission spectra of 200 nm diameter gold nanodisk arrays with varying array periods.

Since the spectral position of the small rise (at wavelengths around 650nm) is related to the period, it suggests that the small rise is related to the Wood's anomaly [174]. The position of the anomaly's spectral position  $\lambda_w$  can be calculated using the following equation [176]:

$$\left(\frac{n_2}{\lambda_w}\right)^2 - \left(\frac{n_1}{\lambda_w}\right)^2 \sin^2 \theta - 2 \frac{n_1}{\lambda_w} \sin \theta \left(\frac{i}{P} \cos \phi + \frac{j}{P} \sin \phi\right) = \frac{i^2 + j^2}{P^2} \quad 4.1$$

where  $\lambda_w$  is the Wood's anomaly wavelength,  $n_1$  and  $n_2$  are the refractive indices of the superstrate and the substrate, respectively.  $P$  is the array period,  $\theta$  is the angle of incidence,  $\phi$  is the azimuthal angle between plane of incidence and the xz plane, and  $i$  and  $j$  correspond to integer values of the diffraction order. For normal incidence ( $\theta = 0$ ), air superstrate ( $n_1 = 1$ ), glass substrate ( $n_2 = 1.47$  fitted by simulation software),  $P = 450$  nm and  $(i, j) = (1, 0)$ , the analytically calculated wavelength of the Wood's anomaly is 661.5 nm, which matches well with the simulated result.

Figure 4.14 (a), (b) and (c) shows the dispersion relationships of the resonant wavelength, transmission intensity at resonant wavelength, FWHM with respect to the nanodisk diameters variation, respectively. The transmission spectra of the nanodisk arrays with

larger diameters shows a red shift at resonant wavelength. They also reveal wider linewidths, which will decrease the resolution, and a larger transmission dip because the amount of scattering increases in larger particles, leading to an overall increase in the area above the transmission dip. In addition as demonstrated by Munechika *et al.* using silver nanoprisms [177], larger particles exhibit radiation damping on faster timescales, which in turn will produce broader spectral features.

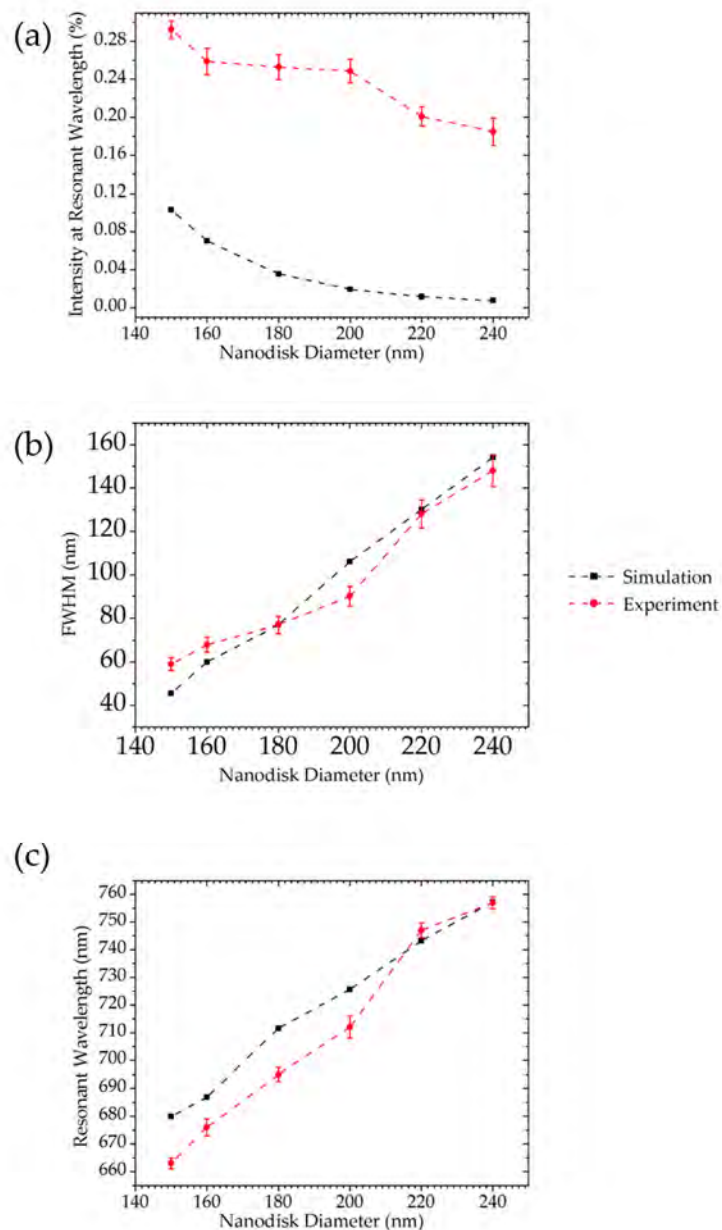


Figure 4.14 Summary of the nanodisk diameter effects on the (a) Intensity at the resonant wavelength, (b)FWHM, and (c) resonant wavelength of the LSPR. Error bars are added based on the standard deviation of

three different measurements on three different samples. The deviations are caused by fabrication imperfection and measurement error. The twenty percent intensity difference between the simulated and the measured results is likely to be caused by the difference in the optical properties of the evaporated Au and the ones used by the simulation software (see Section 7.4 Future Work).

Through the spectral characterisations, it is demonstrated that when increasing array period or structural diameter, the resonant wavelengths exhibit a red-shift and can be tuned from the visible to the near infrared. There is some trade-off between the spectral sensitivity (resonance wavelength) and the spatial resolution (transmission spectra linewidth). Since a LSPR at longer wavelength shows higher sensitivity to the refractive index change of the surrounding medium, a longer array period is desirable. However, these designs also have a large FWHM which is not desired for LSPR sensing. During the second set of characterisations, it is shown that the nanodisk diameter also has a strong impact on the resonance intensity and the resolution. During the investigation of the nanodisk diameter impact on LSPR, another trade-off between the linewidth and resonant intensity has been found. Small size nanodisks give narrower linewidth but meantime reduces the resonant intensity.

These two experiments did not include all the parameters which affect the plasmonic resonant conditions. The thickness of the nanodisks also can also be optimised to improve the performance of a LSPR-based sensor. Different shapes of nanostructures, such as nanoprisms, nanocubes, nanorods, nanopyramids have also been studied and give different sensitivity and FOM [178] [36]. The given examples of tunable resonance of gold nanodisk arrays are to demonstrate that such structural resonant wavelength can be tuned to some specific wavelength and optimised for various applications. For example, among all the designs listed in Table 4.1, design B3, C2, C3 have the plasmonic resonance close to the high limit of the microspectrophotometer and shows a narrow linewidth. Therefore, they can be selected as a potential candidate for LSPR sensing. Detailed discussions about gold nanodisk for LSPR-based sensing can be found in following sections.

#### 4.1.5 Glycerine-Water Solution for Sensitive Calibration

The ability with which metal nanostructures can detect changes in refractive index is generally expressed in terms of their bulk sensitivity ( $\eta_B$ ), which is the linear dependence

of resonance wavelength  $\Delta\lambda_{min}$  on the homogeneous bulk refractive index changes of the dielectric environment:  $\eta_B = \frac{\Delta\lambda_{LSPR}}{\Delta n}$  ( nm/RIU, RIU: refractive index unit).

In order to characterise the sensitivity of the LSPR nanostructures, the refractive index of the environment surrounding the nanodisks was varied by changing the concentration of glycerine-water solution that was pipetted on top of the sample. The glycerine was made in the lab using weight by weight dilution [179]. Figure 4.16 shows the transmission spectra of the gold nanodisk array when pipetting different concentrations of glycerine solutions on top. The different concentrations will invariably result in change of refractive index around the nanodisks. In order to simulate the transmission response, the surrounding refractive index of the sensor surface was changed (equivalent to the different concentrations of glycerine in water). A red shift of the dip position (resonant wavelength  $\lambda_{min}$ ) occurs. The resonant wavelength exhibit a linear relationship with the surrounding refractive index (Figure 4.15). This linear dependence is in good agreement with the simulated results.

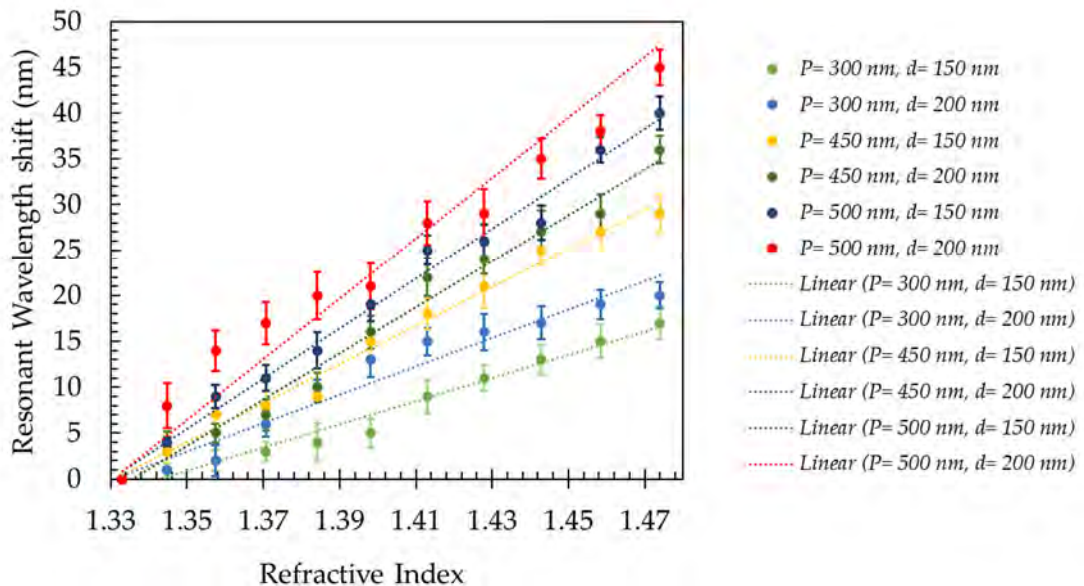


Figure 4.15 Resonance wavelength shift (y-axis) as a function of refractive index of glycerine-water solution (x-axis) for different gold nanodisk designs (A2, A3, B2, B3, C2, C3) ( $P$  is the period and  $d$  is the diameter of the nanodisk). Linear fits have been added. In combination with the results shown in Figure 4.3, the designs with resonances at longer wavelengths display greater sensitivity than those with resonances at shorter wavelengths. Error bars are added based on the standard deviation of three different measurements on three different samples. The deviations are caused by fabrication imperfection and measurement error.

Plasmonic sensors with resonances at longer wavelengths display a longer shift with an increase in refractive index change than those with resonances in the short wavelength region [34]. As shown in Figure 4.15, the sensitivity of the nanodisk LSPR sensor is greater at longer wavelengths.

	Sensitivity $\eta_B$ (nm/ RIU)	FWHM $\Gamma$ (nm)	$FOM = \frac{\eta_B}{\Gamma}$
A2: $P= 300 \text{ nm}, d= 150 \text{ nm}$	120.61	115	1.049
A3: $P= 300 \text{ nm}, d= 200 \text{ nm}$	141.88	159	0.892
B2: $P= 450 \text{ nm}, d= 150 \text{ nm}$	205.73	88	2.338
B3: $P= 450 \text{ nm}, d= 200 \text{ nm}$	255.39	103	2.479
C2: $P= 500 \text{ nm}, d= 150 \text{ nm}$	283.77	100	2.838
C3: $P= 500 \text{ nm}, d= 200 \text{ nm}$	319.24	150	2.128

Table 4.2 Calculated Sensitivity, FWHM, FOM of six candidates for sensing application.

Designs with array period larger than 600 nm have resonance wavelengths longer than the detection range (1000 nm) of the microspectrophotometer, so they were not included in Table 4.2. Design C2 has larger FOM compared to B3, but its transmission dip is 40% as compared to 60% of design B3. Design C3 shows high sensitivity amongst all designs but a rather large linewidth compared to design B3. Considering the resonant wavelength  $\lambda_{min}$  in liquid media was in the 800 - 900 nm range (close to the upper limit of the spectrometer measurement range), along with the transmission intensity and the FOM mentioned in the last section, the design B3 ( $a = 450 \text{ nm}, d = 200 \text{ nm}$ ) is the best candidate for sensing applications than the other designs. Design B3 was chosen for in-depth study and was combined with the acoustic sensor which will be discussed in Chapter 6.

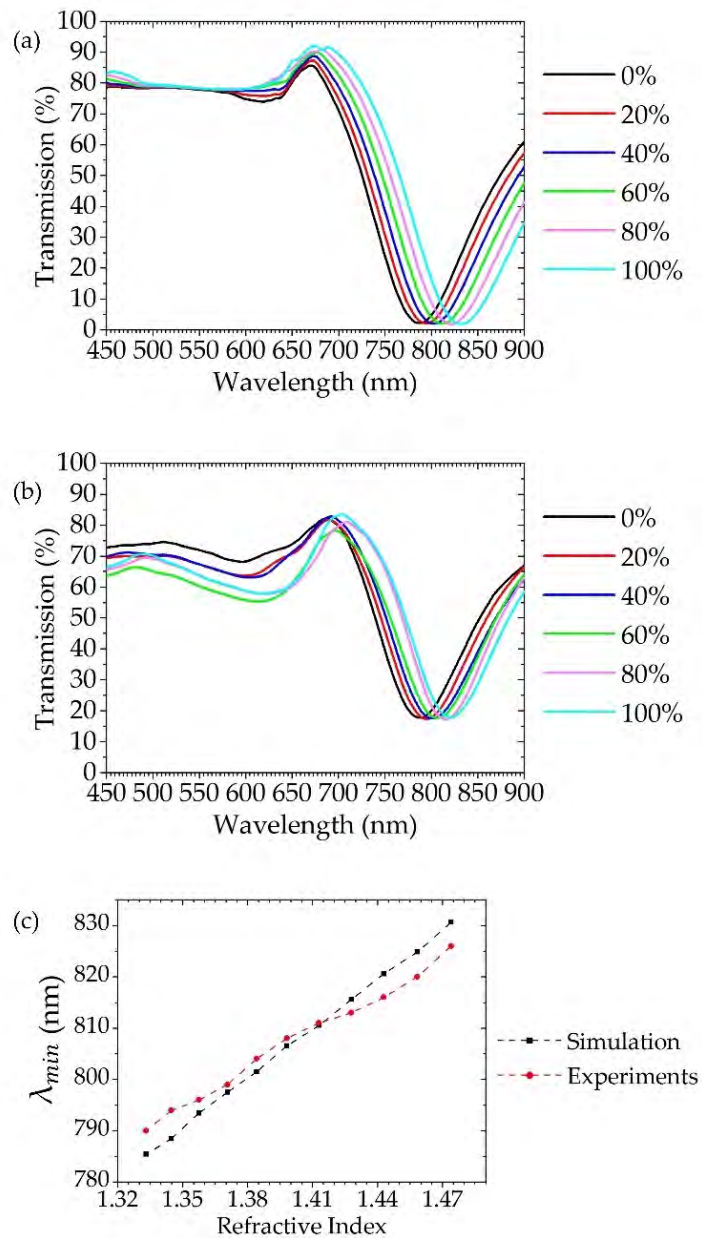


Figure 4.16 (a) Simulated and (b) measured transmission spectra for the LSPR sensors in glycerine-water solutions of differing concentrations. (c) LSPR resonance wavelength  $\lambda_{min}$  shift as a function of bulk refractive index change of glycerine-water solution.

Figure 4.16 shows the simulated and measured transmission spectra for the gold nanodisk LSPR sensor based on design B3. The sensitivity of its plasmon resonance to the refractive index of the surrounding medium is investigated. For the design B3, the resonance wavelength red-shifts with increasing refractive index of the solution. The sensitivity of the LSPR is 273 nm/RIU for the experimental result, which is comparable to the simulated value of 321 nm/RIU.

Figure 4.17 shows the simulated electric field distribution of design B3 at the resonance wavelength (719 nm in air and 827 nm in water). The material on top of the nanodisks is changed from air to water by setting corresponding refractive indices to the orange region in Figure 4.1 (b). Figure 4.17 (a) shows the cross-sectional view (in the x-z plane, see field monitor in Figure 4.1 (b)) of design B3 in air. Figure 4.17 (b) and (c) shows the top view (in the x-y plane) of the nanodisk top surface and the bottom surface respectively. While Figure 4.17 (d), (e) and (f) show the corresponding views of design B3 in water. The electric fields distributed was along the x-axis symmetrically, because the incident beam polarisation was set parallel to the x-axis in the simulations, and the maximum field area appeared at edges of the nanodisk when the coordinate in y-axis was 0. From the cross-sectional views, it is clearly seen that for gold nanodisk in air, stronger electric fields are generated at the bottom surface (the SiO<sub>2</sub>/gold interface), and only small fields appeared at the top surface (the air/gold interface). This is in contrast for gold nanodisks under water as both, the top and bottom surfaces, show similar field enhancement since the refractive index of water ( $n_w = 1.3303$ ) is close to that of the SiO<sub>2</sub> substrate ( $n_s = 1.46$  between 700 nm - 800 nm). When the difference between the refractive indices of the substrate and top dielectric environment is larger, LSPR at the top and the bottom of the metal will diverge into two different modes and it will be presented in the transmission spectra as two transmission dips at different wavelength. This effect will be discussed in the next chapter.

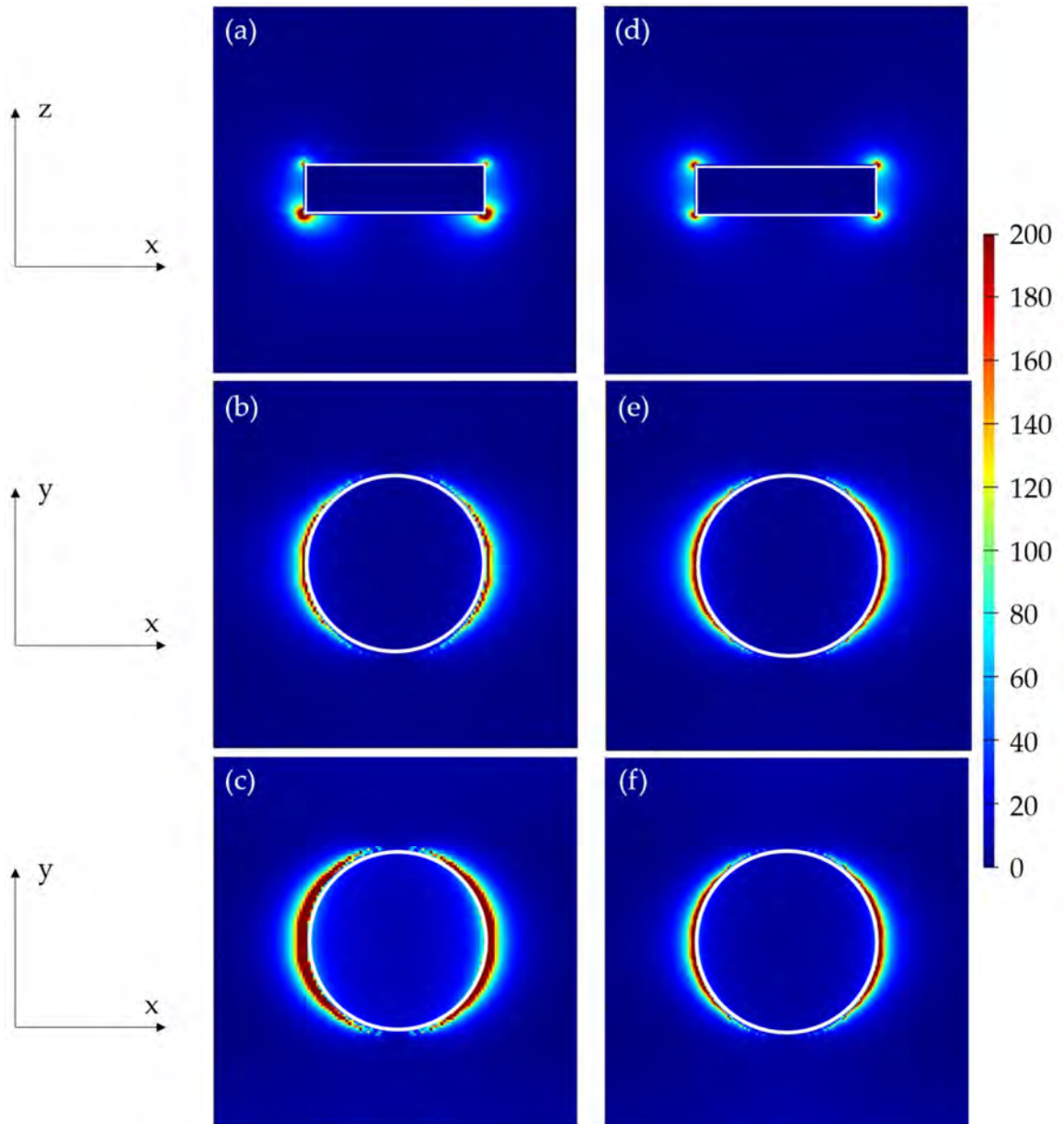


Figure 4.17 Electric field intensity distributions represented as  $|E|^2$  contours at the resonance wavelength  $\lambda_{min}$ . (a), (b), and (c) are the simulated results when the nanodisk is in air; (d), (e), and (f) are the simulated results when the nanodisk array in water. (a) and (d): Cross-section view of the nanodisk (b) and (e) Top view of the top surface of the nanodisk. (c) and (f) Top view of the bottom surface of the nanodisk. The outline

## 4.2 Gold Nanodisk Arrays as Biosensor Based on LSPR

As discussed in Chapter 2, metal nanostructures show great potential in biosensing due to the LSPR. To demonstrate this, the molecular binding between a pair of classical biological ligand and ligate: Protein A and immunoglobulin G (IgG) was studied. Protein A can be directly attached to gold surface IgG can be immobilised on Protein A due to the high affinity of protein A to the amine-terminated regions of protein IgG.

Design B3 was chosen to experimentally test the performance of the gold nanodisk array as a LSPR biosensor.

First the sample surface is cleaned with O<sub>2</sub> plasma ashing. Then it was dipped into 500 mg/mL Protein A solution for two hours. After rinsing using PBS, 500mg/mL concentration of IgG in solution was then pipetted onto the protein layer and stored under room temperature for 1 hour. Once immobilisation is achieved, the device was ready for characterisation. The final device is illustrated in a schematic shown in Figure 4.18.

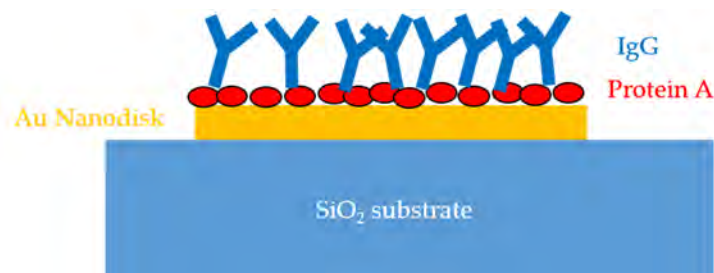


Figure 4.18 Illustration of Protein A and IgG binding on sample surface.

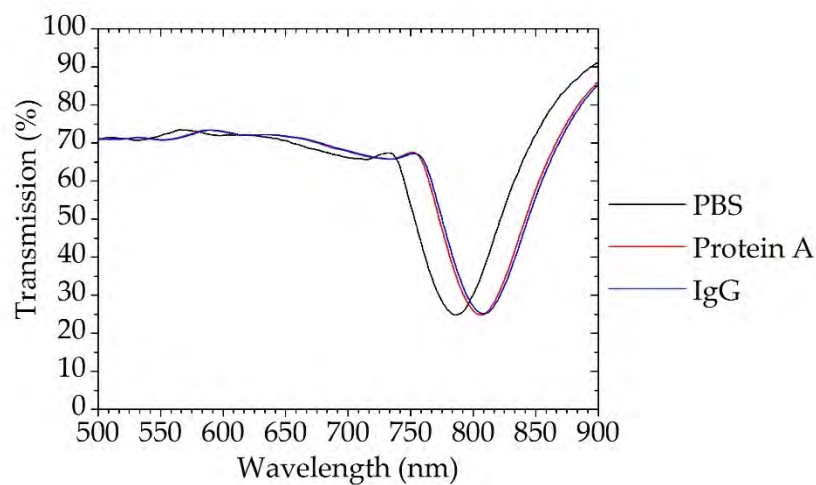


Figure 4.19 LSPR transmission spectra of Protein A attached to gold nanodisk array design B3. The measurement range has been reduced to 500-900 nm in order to discern the change in spectra. Red and blue spectra were obtained after immobilisation of Protein A and IgG on the gold nanodisks, respectively.

Figure 4.19 shows the transmission spectra after the Protein A binding and the IgG binding, as well as the spectra from an PBS immersed sensing surface as a reference.

As can be seen, the resonant wavelength has a red-shift ( $\Delta\lambda_1$ ) of 19.8 nm, after introducing Protein A on to the sample surface. After the binding reaction of Protein A and IgG, the resonant wavelength shows a red-shift of another 2.2 nm ( $\Delta\lambda_2$ ). Since this shift is smaller

than the error caused by fabrication imperfection (See Figure 4.11 and Figure 4.14), it implies that in order to maintain the repeatability, a reference measurement is necessary for each sample before the LSPR measurements. Moreover, a continuous measurement is preferred to reduce the measurement error (*e.g.* optical alignment). According to the Mie theory (Section 2.1.3.1), the LSPR depends on the refractive index of the surrounding medium. Therefore, the red shift of the transmission dip resulted from changes in the local refractive index around the nanoparticles by Protein A immobilisation and Protein-IgG binding reaction. The transmission spectra of gold nanodisk array immersed in PBS buffer solution shows similar resonant wavelength as immersed in water and indicates that the refractive index of PBS solution has similar refractive index as water.

Although direct attachment to gold works for Protein A and many other proteins, in some cases the proximity to the surface may make certain proteins prone to denaturation and lead to inconsistent results. So, the covalent attachment and self-assembled monolayer was adopted for the future work which was mention in Section 3.3.

### 4.3 Summary

It has been demonstrated that various nanodisk arrays with different geometrical sizes were successfully produced via a series of fabrication process which combined electron beam lithography, lift-off and post fabrication annealing. By engineering the geometrical sizes, the localised surface plasmon resonance (LSPR) of the nanodisk arrays can be tuned within a certain wavelength range and different linewidth. By comparing the sensing performance in terms of the sensitivity, FOM, and transmission intensity, the sensor design has been optimised. The nanodisk array design B3 that have been presented in this chapter was designed to be integrated with the acoustic device QCM. This work will be presented in Chapter 6. An approach for reducing ebeam time for writing nanodots have been presented and will be used in the work presented in Chapter 6.

In the experiment where the gold nanodisk arrays were used for LSPR sensing, the simulated results showed that at the resonant state an intense, highly confined electric field can be generated at the surface of the nanodisk. A biomolecule binding experiment was conducted and show that the gold nanodisk array can be used as a LSPR based biosensor.

# 5. LSPR Sensor on LiNbO<sub>3</sub>

This chapter presents the simulation, fabrication, and experimental characterisation of a localised surface plasmonic resonance (LSPR) sensor integrated with an acoustic sensing compatible substrate. The LSPR sensor is designed to work in the visible region with gold nanodisk arrays fabricated on Lithium Niobate (LiNbO<sub>3</sub>), which is both piezoelectric and birefringent. A linear relationship between resonance wavelength and varying liquid refractive indices were observed in experiments. Polarisation effects of the birefringent property of the Y-cut LiNbO<sub>3</sub> substrate have been investigated, which can also be applied to X-cut LiNbO<sub>3</sub>. This study demonstrates the feasibility of an LSPR sensor device utilising a birefringent substrate, which has acoustic wave compatibility and can pave the way towards much more robust and flexible biosensing devices.

## 5.1 Introduction

As has been presented in the previous chapter, both photonic and acoustic technologies are prominent in sensing applications. The configuration of LSPR sensors reduces instrumentation complexity and can be rendered into a low-cost laboratory-on-a-chip (LOAC) format [180] [181]. The planar configuration of surface acoustic wave (SAW) devices is also suitable for LOAC formats [182].

LSPR can be exploited to create an enhanced electric field at the surface of metallic nanostructures (boundary between a metal and dielectric). At resonance, the field is strongly localised so that the exact characteristics of the associated spectrum are highly sensitive to the refractive index of any material that is close, or attached, to the surface [2] [3]. LSPR biosensing can be achieved using metallic nanoparticles or from structured metallic thin films deposited on to a substrate - typically glass. Biosensors based on LSPR possess many advantages such as high sensitivity, can be used *in-situ*, and possess label-free operation that are desirable for biosensing applications [34] [183].

On the other hand, surface acoustic wave sensors use interdigitated transducers (IDT) to generate and detect acoustic waves on the surface of the piezoelectric substrate, e.g. quartz, LiNbO<sub>3</sub> or LiTaO<sub>3</sub> (lithium tantalate). A quantifiable change occurs in the resonance frequency and amplitude of the propagating wave that correlates to adsorbed mass,

viscoelastic changes, and the conductivity of the surrounding liquid [184]. Unlike LSPR, which is only sensitive to the bound molecule layer (in a liquid sample), acoustic sensors are not only sensitive to the binding molecules but also the viscosity of the solvent coupled to the biomolecule [185]. Whilst LSPR can measure the mass of the adsorbed layer, an acoustic sensor can measure the viscous drag between the liquid and biomolecules, and determine the size and shape of the target biomolecule [186]. SAW devices can be used to induce a liquid flow by acoustic streaming [71], where this phenomenon has been used in conjunction with a continuous metal film to accelerate and improve analyte capture for LSPR sensing [182], [187].

In this chapter, the potential for co-integration of acoustic and LSPR technologies on a single device has been investigated, and in particular to study the *optical* properties of LSPR nanostructures on piezo-active materials. In order to do this, the piezo-active material LiNbO<sub>3</sub> has been selected, as it has high optical transmission (over 80% in the visible range), large electromechanical coupling coefficients, as well as being optically birefringent unlike the glasses typically used to make LSPR sensors. Since Y-cut LiNbO<sub>3</sub> support shear horizontal SAW which is widely used for SAW sensing, samples from a 500  $\mu\text{m}$  thick Y-cut wafer were used in this study. Results on the refractive index dependent response of differing water-glycerine concentrations and polarisation sensitivity of LSPR nanostructures on LiNbO<sub>3</sub> are presented. This work has been published in Applied Physics Letters[188].

## 5.2 Design and Simulation

The transmission spectra of the gold nanodisks on LiNbO<sub>3</sub> were simulated using *Lumerical FDTD*. A semi-infinite Y-cut LiNbO<sub>3</sub> substrate and a semi-infinite air/liquid superstrate were used to create the model. Periodic boundary conditions were defined along the  $x$  and  $z$  axes and perfectly matched layers (PML) were set at the top and bottom boundaries to absorb any unwanted reflections. A mesh cell with size of  $\Delta x = \Delta y = \Delta z = 2 \text{ nm}$  was set in the region encompassing the metal layer and part of the LiNbO<sub>3</sub> and air/liquid layer. In the simulations, Johnson and Christy's experimental values were used for the complex permittivity data of Au [171].

The refractive index of LiNbO<sub>3</sub> was set in the material database. Crystalline LiNbO<sub>3</sub> can be cut on any of three planes to make X-, Y- or Z-cut surfaces, which are normal to crystallographic directions [2 $\bar{1}\bar{1}$ 0], [1 $\bar{1}$ 00], and [0001], respectively [189]. A schematic diagram illustrating the crystallographic directions of LiNbO<sub>3</sub> is shown in Figure 5.1. Due to the anisotropic nature of LiNbO<sub>3</sub> the refractive index for light normal to the Y-cut plane is sensitive to polarisation. For an incident ray  $k_o$  with the electric field in the direction of [2 $\bar{1}\bar{1}$ 0], then the refractive index is  $n_o = 2.287$  [190] whilst for an incident ray  $k_e$  with electric field in the direction of [0001], then  $n_e = 2.203$  [190]. A permittivity rotation grid attribute was used to rotate the refractive index matrix, using a set of Euler angles, to the Y-cut rotation matrix.

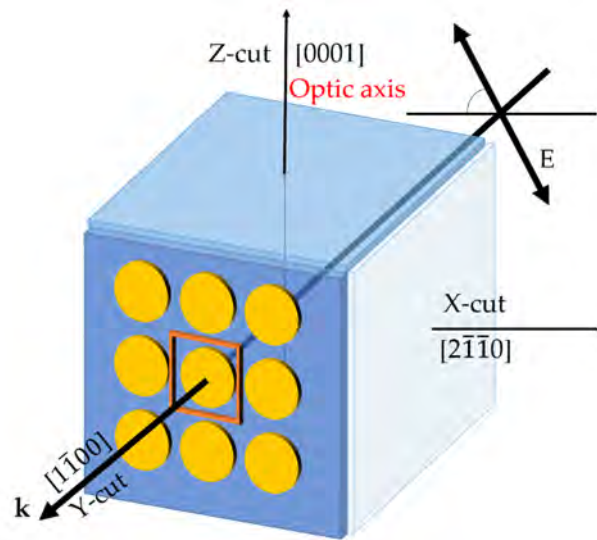


Figure 5.1 Schematic diagram showing gold nanodisk array and the crystal planes of the LiNbO<sub>3</sub>. The coordinate system in this figure is for showing the different crystal cutting, and is not the same as the one of FDTD simulation.

To simulate an unpolarised beam or plane wave source, two simulations with orthogonal polarisations are required. Results for an unpolarised source were then calculated by incoherently summing results from the two polarised simulations according to the formula shown below.

$$(|E|)^2 = \frac{1}{2}|\vec{E}_o|^2 + \frac{1}{2}|\vec{E}_e|^2 \quad 5.1$$

$E_o$  and  $E_e$  are the electric field of two orthogonally polarised beams  $k_o$  and  $k_e$ , respectively. In practice, this means that two simulations with orthogonally polarised beams ( $k_o$  and  $k_e$  show in Figure 5.2) needs to be performed sequentially. The simulation and calculation

was completed by using a script (Appendix). First, a beam with a “polarisation angle” of  $0^\circ$  was simulated and the simulated file was saved as ‘temp\_0’. Secondly, the beam ‘polarisation angle’ was set to  $90^\circ$  before running the simulation. When two simulations were completed, the unpolarised transmission and the field profile of both were extracted and the net transmission for both polarisations (*i.e.* unpolarised light) was calculated using the arithmetic average of these simulations[191].

$$(|E|)^2 = \frac{1}{2} |\vec{E}_0| + \frac{1}{2} |\vec{E}_{90}| \quad 5.2$$

The quantity  $(|E|)^2$  refers to the time averaged electric field intensity of an unpolarised beam source [191].

Schematics of the top-down view (x-y plane) and cross section (x-z plane) of simulated gold nanodisk arrays on LiNbO<sub>3</sub> are shown in Figure 5.1(a) and (b), respectively. The array period is given by  $P$  and the disk diameter is given by  $d$ .

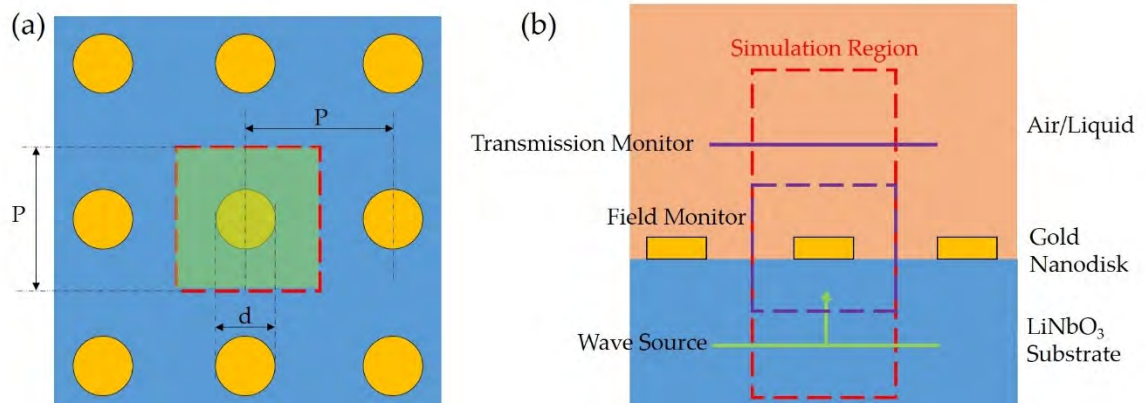


Figure 5.2 Schematic of the simulated gold nanodisk array structure. (a) Top-down view of the simulated gold nanodisks. The green region is the simulated region. The red dash line encloses the unit cell of the nanodisk array structure.  $P$  denotes the array period and  $d$  denotes the disk diameter. (b) Cross section of the simulated gold nanodisks. The red dash line encloses the simulated unit cell.

Figure 5.3 shows the simulated transmission spectra for applying air (refractive index  $n=1.0$ ) on top the sensing surface for unpolarised light with a wavelength range from 400 nm–1000 nm. When changing the array period and the diameter of the nanodisk, the LSPR on LiNbO<sub>3</sub> shows same modifiability as described in previous chapter. As we can see in the electric distribution (Figure 5.3(b)), the resonance has local maximum intensity at the bottom of the gold nanodisk, which is the interface of LiNbO<sub>3</sub> substrate and metal.

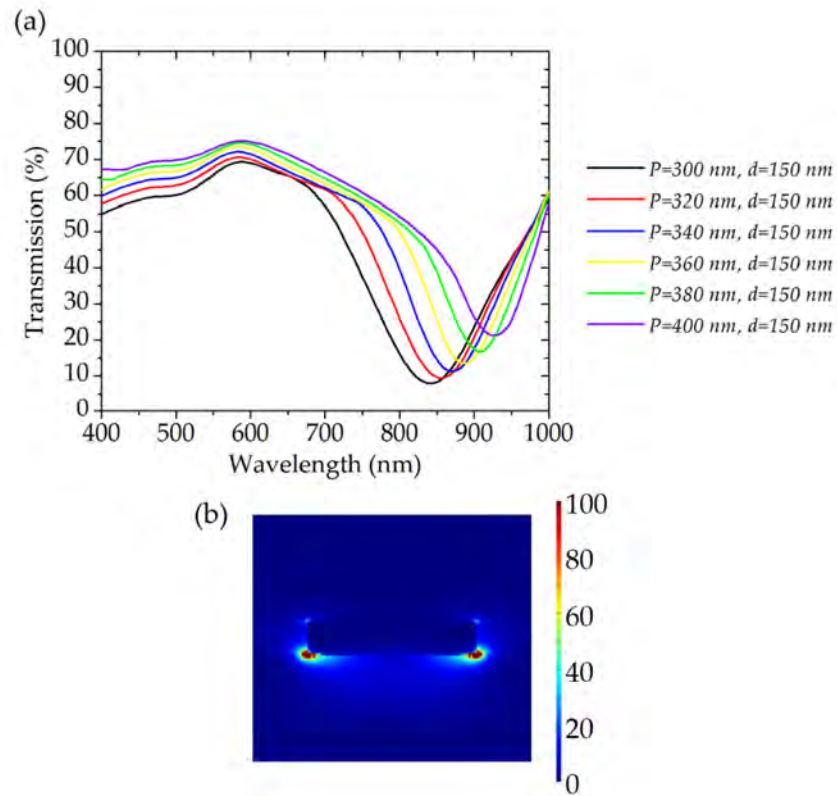


Figure 5.3 (a) Simulated transmission spectra gold nanodisk arrays on  $\text{LiNbO}_3$  with different periods,  $P$ , which show a red-shift tendency of resonance wavelength, also occurring among these designs as presented in the last chapter for gold nanodisk arrays on  $\text{SiO}_2$ . (b) Cross section view of the electric-field distribution at the resonance wavelength ( $\lambda_0 = 845 \text{ nm}$ ) of nanodisk arrays with  $P=300 \text{ nm}$ ,  $d = 150 \text{ nm}$ .

The effect of changing the diameters of nanodisks also show similar effects on transmission spectra as discussed in the last chapter. The simulated results are shown in Figure 5.4.

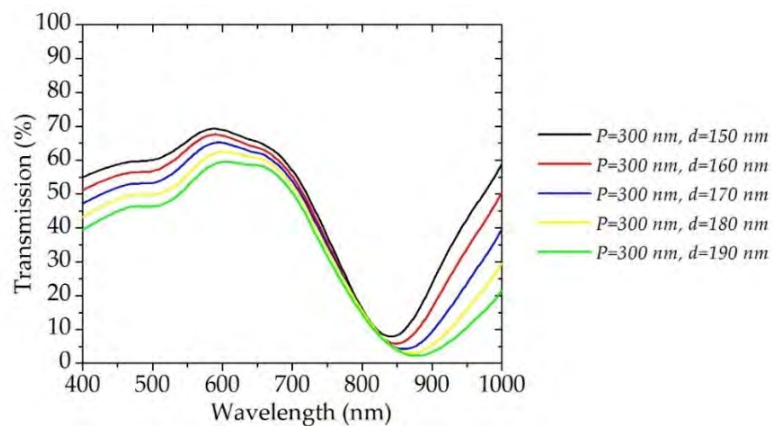


Figure 5.4 Simulated transmission spectra for gold nanodisk arrays with varying disk diameters,  $d$ . The period,  $P$ , has been set as  $300 \text{ nm}$  for this set of simulation. Larger disks result in a redshift of the resonant wavelength, lower transmission and a larger bandwidth, as has been presented in last chapter.

Figure 5.5 shows the simulation result for applying water on top of the sensing surface of gold nanodisk arrays on LiNbO<sub>3</sub>. The transmission spectra show two resonance transmission dips after replacing air with water. Both of the resonant wavelengths show similar variations tendency when the structure shape changes, where these variations also agree with the previous finding described in the last chapter.

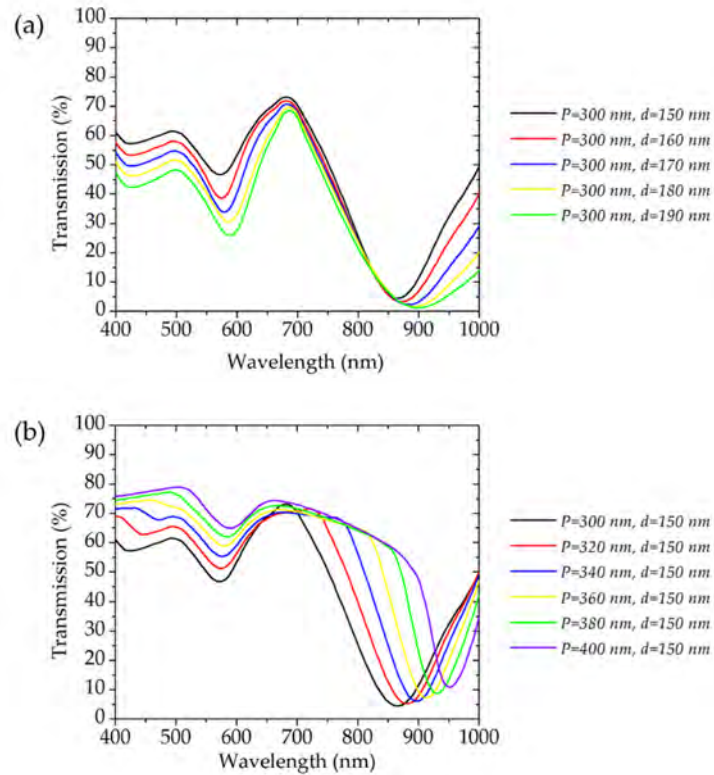


Figure 5.5 (a), (b) Simulated transmission spectra gold nanodisk arrays in water with different periods,  $P$ , and diameter,  $d$ , respectively.

### 5.3 Fabrication

Using the 500  $\mu\text{m}$  thick Y-cut LiNbO<sub>3</sub> as a substrate, arrays of gold nanodisks were proposed as LSPR sensors in the configuration shown in Figure 5.6. These were fabricated on the LiNbO<sub>3</sub> sample surfaces as follows: first, the sample was solvent cleaned using acetone and then isopropyl alcohol (IPA), with 5 minutes of ultrasonic cleaning at each stage. The sample was then rinsed in deionised (DI) water. Since LiNbO<sub>3</sub> is pyroelectric, an electrical potential will be generated during the thermal treatment. Also, as the material is piezoelectric, the built-up static charge may create mechanical strains in the crystal.

Therefore, a small temperature-gradient was used to heat and cool the sample to reduce the risk of wafer breakage.

A bi-layer of PMMA was spin coated on to the LiNbO<sub>3</sub> surface using same recipe as given in Section 3.2; the resist was then prebaked on a hot-plate by ramping the temperature from 65 °C to 95 °C for a total time of 8 minutes per coating. To avoid charging effects that can damage LiNbO<sub>3</sub> when carrying out electron beam lithography (EBL), a 30 nm Al layer was evaporated on top of the resist. EBL patterns were written using 1 nm resolution, a beam spot size of 4 nm and the VRU was 5. Since the molecular mass of LiNbO<sub>3</sub> (148 g/mol) is larger than that of SiO<sub>2</sub> (60 g/mol), the backscattering effect would be more critical for LiNbO<sub>3</sub>. Due to this reason, the dose test was set in the range of 150 μC/cm<sup>2</sup> to 450 μC/cm<sup>2</sup>. After the EBL patterning, the protective Al layer was removed by MF-CD26 after the electron beam exposure; finally, after development in MIBK: IPA (1:2) solution, 60 nm Au was evaporated on to the sample with an initial 3nm Ti adhesion layer and the sample was then put into hot acetone for up to 4 hours for lift off.

A scanning electron microscope (SEM) image of a sample can be seen in Figure 5.6, which was a square array of gold disks with a periodicity  $P = 300$  nm and a disk diameter  $d = 180$  nm (dimensions ' $P$ ' and ' $d$ ' are shown in the Inset of Figure 5.6.)

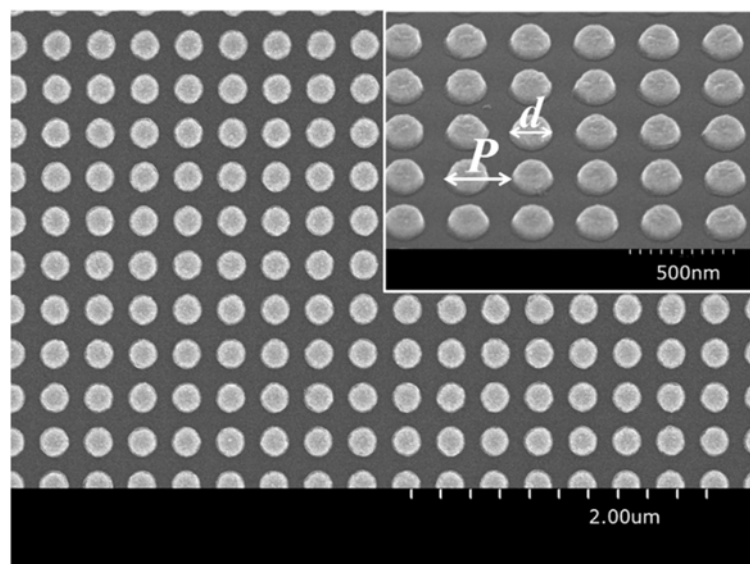


Figure 5.6 A scanning electron micrograph of gold nanodisks in a square array with a period of 300 nm on Y-cut LiNbO<sub>3</sub>. Inset: a microscope image tilted at 45°, where  $P$  and  $d$  are the periodicity and disk diameter, respectively.

## 5.4 Results and Discussion

### 5.4.1 Effect of the Substrate Refractive Index on Resonance

Shown in Figure 5.7 is the simulation result for applying water on top of the sensing surface for the design with  $P= 300$  nm and  $d= 180$  nm. Using an LSPR sensor based on  $\text{LiNbO}_3$ , which has an approximate *average* refractive index of 2.25 (due to the anisotropy of  $\text{LiNbO}_3$ ) for *unpolarised* light, and the water having a refractive index of 1.33, the large gap between these two refractive indices induces two resonance modes in the transmission spectra: a  $\text{LiNbO}_3$  mode at  $\lambda_B$  (where the subscript ' $B$ ' means 'bottom'); and a liquid mode at  $\lambda_T$  (where the subscript ' $T$ ' means 'top'). The power distribution shows that the resonance at  $\lambda_T$  has a local maximum intensity at the top of the gold nanodisk – which is the interface of water and metal (Figure 5.7(b)) – whilst the resonance at  $\lambda_B$  has a local maximum intensity at the bottom of the nanodisk – which is the interface of metal and  $\text{LiNbO}_3$  (Figure 5.7(c)). LSPR sensors based on glass that were studied in Chapter 4 appear to have only one resonance mode since the refractive index of the analyte is similar to that of glass ( $n=1.5$ ) and the two modes hybridise together in the transmission spectra to give a broad response [192].

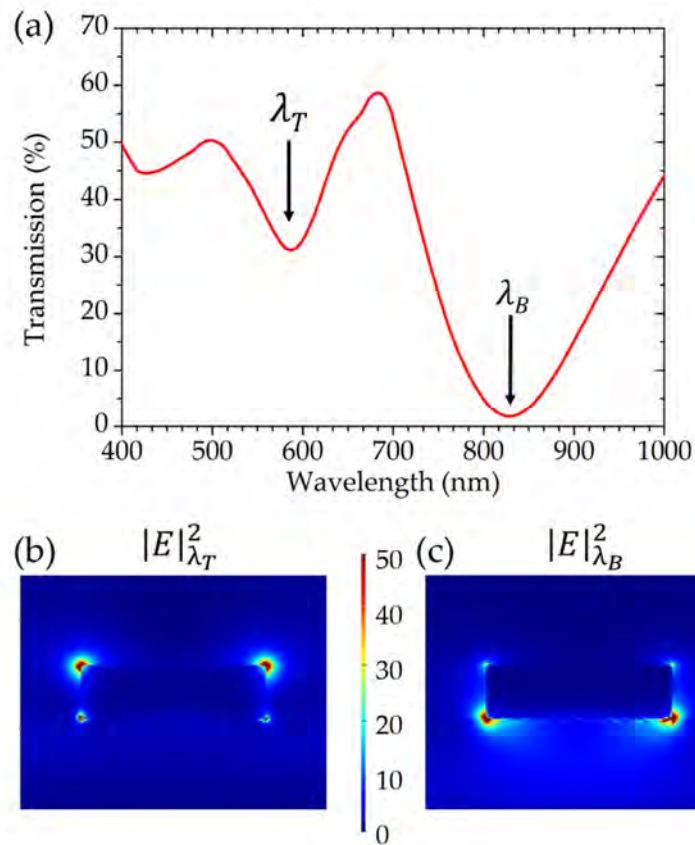


Figure 5.7 (a) Simulated transmission spectrum for LSPR sensors in water, where the two main resonance wavelengths are marked as  $\lambda_T$  and  $\lambda_B$ . (b), (c): Electric field intensity distributions in the xy plane at  $\lambda_T$  and  $\lambda_B$ , respectively.

For biosensing applications, the variation of the resonance wavelength is mostly caused by the refractive index change in the analyte [193]. To confirm this, a series of glycerine-water solutions with different concentrations were applied on top of the surface of the LSPR structures, where the refractive index of glycerine is 1.48 and differing concentrations of solution have refractive indices given by Ref. [179]. The corresponding transmission spectra measurements were performed using the TFProbe MSP300 microspectrophotometer. The spectral measurement method was described in Section 3.4. Using the polarisation analyser embedded in the tool, an unpolarised light beam from a halogen lamp was normally incident on to the backside of the sample. The ‘white reference’ and the ‘dark reference’ was acquired each time after setting up the polarisation angle. The polarised light was collected through a 4× magnification objective lens with a spot size of 100  $\mu\text{m}$  in diameter. Measured results are shown in Figure 5.8. It was found that an increase in the glycerine-to-water concentration induces a redshift of the resonance

wavelength modes for both  $\lambda_T$  and  $\lambda_B$ . The resonance wavelengths were extracted and plotted as a function of the liquid refractive index in the Figure 5.9. A sensitivity of 165 nm/RIU has been observed at the liquid mode  $\lambda_T$  and a sensitivity of 130 nm/RIU has been observed at the LiNbO<sub>3</sub> mode  $\lambda_B$ . The sensitivity for the liquid mode is comparable to LSPR sensors on isotropic media, such as SiO<sub>2</sub>, with a resonance in the same wavelength range (Design A2 in last chapter,  $P=300$  nm,  $d=150$  nm, shows a sensitivity of 145 nm/RIU) – for these, the sensitivity increases for longer resonant wavelengths [194], but this principle only applies due to the similarity of substrate and superstrate refractive indices and yields only one broad resonance: for the nanostructures on LiNbO<sub>3</sub> it does not hold true for the higher wavelength  $\lambda_B$  mode compared to  $\lambda_T$ . In essence, it can be inferred that it is the liquid (top) resonance mode  $\lambda_T$  which provides the high sensitivity and undergoes a sensitivity increase for longer wavelengths.

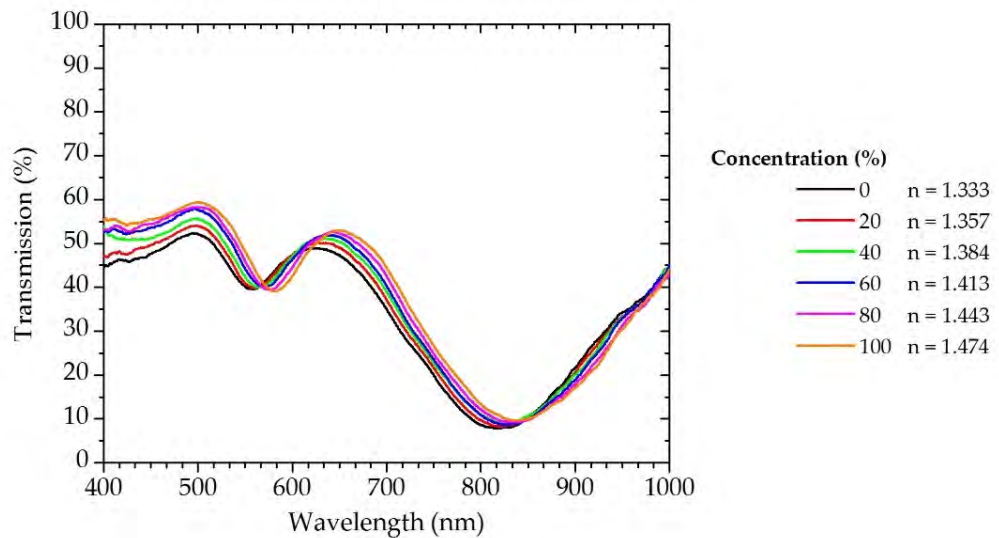


Figure 5.8. Measured transmission spectra for the LSPR sensors in a glycerine-water solution of differing concentrations. The average refractive index for each solution is given to the right of the concentration percentage.

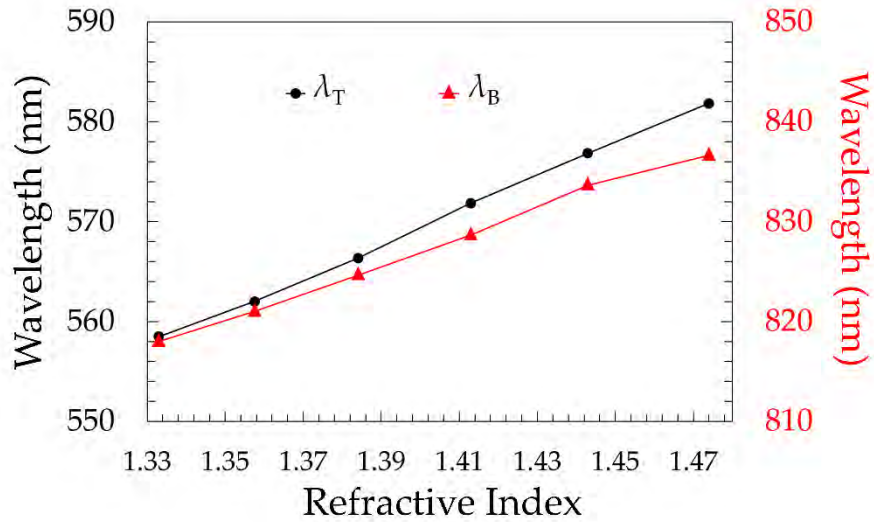


Figure 5.9 Resonance wavelength (nm, y-axis) versus refractive index of glycerine-water solution (x-axis). The black curve is the resonance wavelength shift at liquid mode  $\lambda_T$ , and the red curve is the resonance wavelength shift at LiNbO<sub>3</sub> mode  $\lambda_B$

#### 5.4.2 Effect of Polarisation on the Resonances

Since LiNbO<sub>3</sub> has two distinct values for its refractive index due to birefringence, it is necessary to evaluate the characteristics of the LSPR structure with respect to the crystal orientation. Therefore, simulations and experiments were performed to study the behaviour of the device in response to a changing polarisation by varying the orientation of the E-field from 0° (aligned to the X-cut axis) to 90°, whilst normally incident to the xy plane in Figure 5.2. The transmission spectra in Figure 5.10 (a) shows how the resonance wavelength shifts as the polarisation angles are varied. The superstrate was set to a refractive index of 1.0 (air) to suppress the liquid mode response  $\lambda_T$  (following the trend that the smaller refractive index of the liquid compared to LiNbO<sub>3</sub> yields a much lower response) – the small dip at 520 nm was attributed to be the  $\lambda_T$  (liquid) mode; this was so that we could primarily investigate the  $\lambda_B$  mode only. Due to the symmetrical properties of the nanodisks and their array periodicity, and the fact that the light was as close to normally incident as possible, the variation of  $\lambda_B$  was solely associated to the birefringent properties of the LiNbO<sub>3</sub> crystal. As can be seen in Figure 5.10, the wavelength  $\lambda_B$  varies as a function of the polarisation angle, where we find that it experimentally changes by up to 15 nm between 0° and 90°. The difference between simulated and experimental results

came from the imperfections in the fabricated device and the variation between the fabricated plasmonic filter and the idealised simulation model.

This experiment shows that LSPR structures on birefringent material can offer polarisation sensitive optical transmission for potential applications. For instance, traditional plasmonic colour filters fabricated on glass substrates can only support a single wavelength for each designed pattern; a colour filter which adopts a highly birefringent substrate material may be able to support multiple transmission peaks that can be individually selected by adding a polariser into the device. Following on from this, the wavelength shift at  $\lambda_T$  caused by polarisation change needs to be studied to give us a better understanding of the two resonance modes and the LSPR sensing functionality on high refractive index materials.

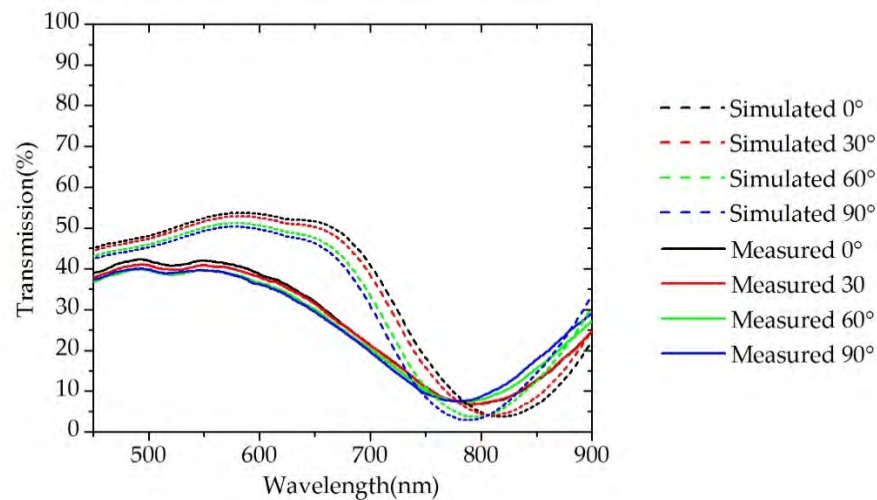


Figure 5.10 Simulated and measured spectra of Au nanodisk arrays on LiNbO<sub>3</sub> surrounded by air. Data is recorded for four different polarisation angles: 0° (x-polarised), 30°, 60°, and 90° (y-polarised).

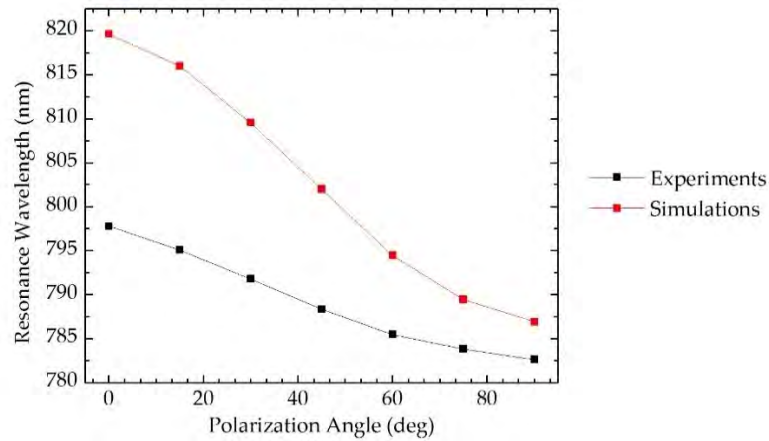


Figure 5.11 Simulated and measured resonance wavelengths of Au nanodisk arrays on LiNbO<sub>3</sub> for seven different polarisation angles.

To examine the impact that birefringence makes to LSPR sensing, experiments were carried out for different concentrations of glycerine-water solution on top of the sample surface in conjunction with polarisation angle changes, and transmission spectra were simulated for polarisation angle change (for water only). As seen in Figure 5.12, since  $\lambda_T$  is related to the LSPR at the interface between the metal and water/glycerine solution it does not shift with polarisation angle change (the vertical line markers between Figure 5.12 (a) and (b) are present for ease of viewing). This is also apparent in the simulated results (Inset of Fig. 4(a)) where the  $\lambda_T$  (top surface) LSPR mode does not shift when the polarisation is varied (even for unpolarised light). We should note that the transmission intensity differences for  $\lambda_T$  between 0° and 90° (when comparing Figure 5.12 (a) and (b)) are simply due to the refractive index mismatches between the birefringent substrate and liquid. Meanwhile, an LSPR at  $\lambda_B$  is more sensitive to the refractive index change of the substrate, as expected, and so exhibits a shift in the spectrum after changing the polarisation from x-polarised (0°) to y-polarised (90°). Experimental results show an average blue shift of the resonance wavelength at  $\lambda_B$  by ~14 nm for the two orthogonal polarisations, when using three different concentrations of water-glycerine solution (0% corresponds to purely water, 50% corresponds to 1:1 water-glycerine, and 100% is purely glycerine), which is comparable to the shift given in Figure 5.11; the Inset of Figure 5.12 (b) shows a plot of the resonance minima at  $\lambda_B$  for clarity.

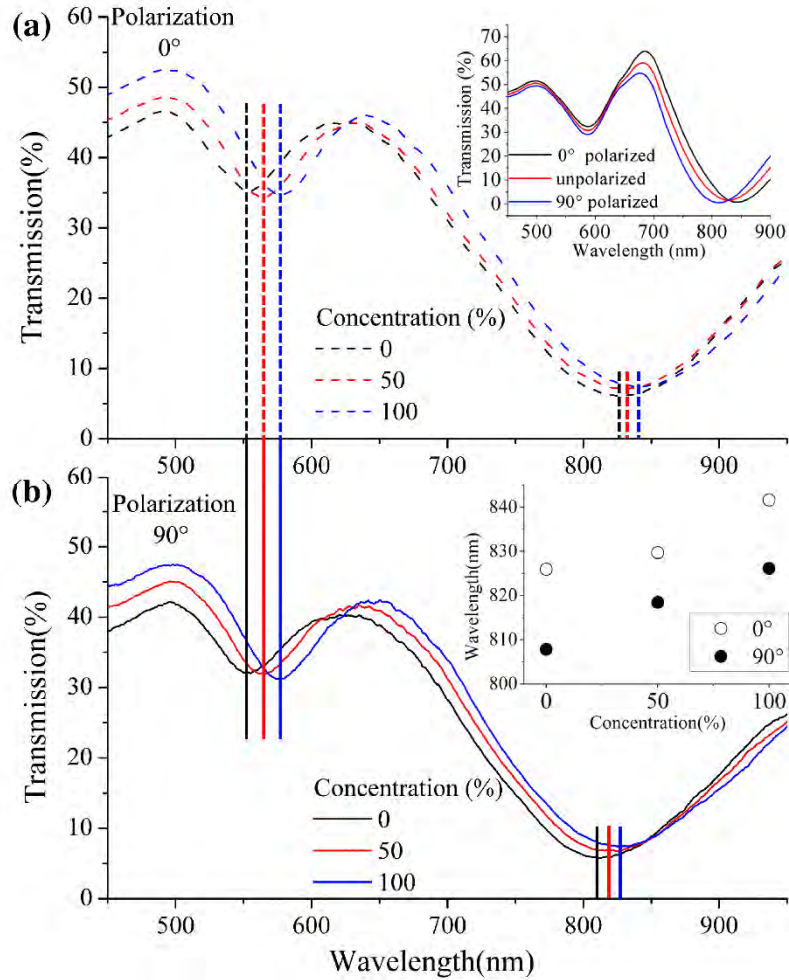


Figure 5.12 . (a) Measured transmission spectra for different concentrations of glycerine-water solution using x-polarised light ( $0^\circ$ ). Inset: Simulated results of the transmission spectra for water (*Black line*: x-polarised light. *Red line*: unpolarised light. *Blue line*: y-polarised light.) (b) Measured transmission spectra for different concentrations of glycerine-water solution using y-polarised light ( $90^\circ$ ). Inset: Measured  $\lambda_B$  minima of concentration-dependent wavelength shift, for  $0^\circ$  (*hollow data*) and  $90^\circ$  (*solid data*) polarisations.

Since the shift at  $\lambda_B$  due to the polarisation change is non-negligible, alignment of the light source and the sensor needs to be considered for a polarised light source. On the other hand, for a fixed polarisation angle, the shift at  $\lambda_T$  due to changes in liquid refractive index variation is larger than those for  $\lambda_B$ , and therefore the liquid mode has a higher sensitivity compared to the  $\text{LiNbO}_3$  mode; as such, it is preferential to utilise  $\lambda_T$  for sensing capabilities since it is also unaffected by substrate birefringence related effects.

### 5.4.3 Optimised Structure for Higher Sensitivity

Based on the investigation in the last chapter and the simulation results at the beginning of this chapter, the design of the LSPR sensor on  $\text{LiNbO}_3$  had been optimised for sensing

application. A design with  $P = 500$  nm,  $d = 300$  nm was simulated, fabricated and characterised. The measured transmission spectra and simulation results are shown in Figure 5.13 for comparisons. The  $\text{LiNbO}_3$  mode had been shifted beyond 1000 nm due to the increased array period and the liquid mode was also shifted to a longer wavelength for higher sensitivity. Since  $\text{LiNbO}_3$  is not suitable for post-fabrication annealing, the mismatch between the simulated and experimental results caused by the fabrication imperfection was foreseeable. The measured sensitivity of this design is 216 nm/RIU, which is similar to Design B2 (in Chapter 4) whose resonance is in the same wavelength range. However, the figure of merit ( $\text{FOM} = \text{sensitivity}/\text{FWHM}$ ) of this design is 1.4, which is only half of that of Design B2 due to the broad linewidth. This is due to the inevitable imperfections in the fabricated device and also the strong internal reflection between  $\text{LiNbO}_3$  and the air/liquid layer.

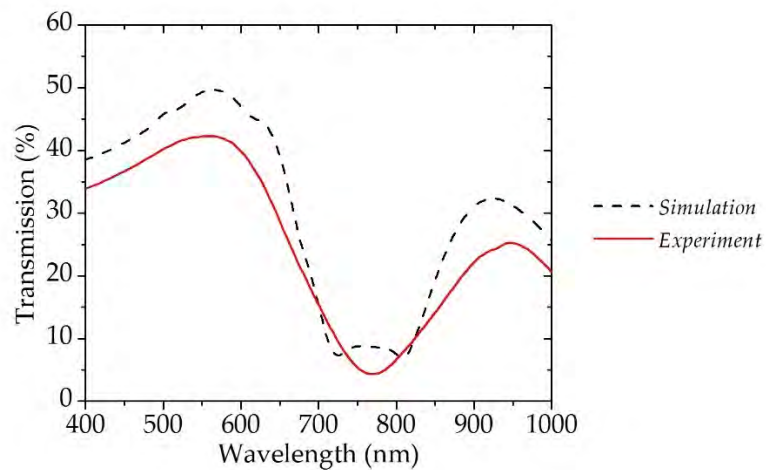


Figure 5.13 Comparison of experimental and simulation results for the  $\text{LiNbO}_3$  based LSPR sensor in water.

## 5.5 Summary

In this chapter, Au nanodisk arrays on piezoelectric substrates was proposed and the relevant fabrication and characterisation processes were introduced. The LSPR sensor has the capability to be coupled with compatible SAW technology. It has been demonstrated that the Au nanodisk arrays exhibit refractive index dependent LSPR properties which can be used for label free biosensing. This chapter has also demonstrated polarisation angle dependent transmission spectra, which arises from the birefringent  $\text{LiNbO}_3$  substrate. It is concluded that for a substrate which has a refractive index differing by a large amount from the analyte, the LSPR sensor should be designed targeting the liquid mode  $\lambda_T$  as this provides a higher sensitivity than  $\lambda_B$ , and is not sensitive to the birefringence of the piezoelectric material. The integration between these Au nanodisk arrays and a SAW sensor can make the hybridised device an efficient, versatile platform for better studying the biomolecule binding process in real time.

# 6. Hybrid QCM and LSPR Sensor for Label Free Biosensing

This chapter reports on the design and fabrication of a hybrid sensor that integrates transmission-mode localised surface plasmonic resonance (LSPR) into a quartz crystal microbalance (QCM) for studying biochemical surface binding reactions. The coupling of LSPR nanostructures and a QCM allows optical spectra and QCM resonant frequency shifts to be recorded simultaneously, and analysed in real time for a given surface adsorption process. This integration simplifies the conventional combination of SPR and QCM, which has the potential to be miniaturised for application in point-of-care (POC) diagnostics. The influence of antibody-antigen binding effect on both the QCM and LSPR has been analysed and discussed.

## 6.1 Introduction

Optical and mechanically oscillating sensing techniques have applications in *in-situ* label free sensing, and analysis of chemical and biological binding reactions [38] [137]. Optical sensing techniques, such as surface plasmonic resonance (SPR), typically measure the change in the refractive index arising from the molecular adsorption on the metal surface, thus determining the molecular mass of thin films [1]. Quartz crystal microbalance (QCM) devices use the resonance phenomenon of piezoelectric quartz, where the frequency of its mechanical oscillation is dependent upon the acoustic mass of the sum of the deposited molecules and the solvent coupled to the adsorbed molecules. Therefore, in a surface adsorption process, the integration of optical and acoustic sensing can not only give information regarding weight but also detect the film hydration status that provides insights into the conformational properties of the molecules in the formed layer on surface and the biomolecule adsorption characteristics.

Owing to the complementary characteristics of SPR and QCM, methods of combining SPR and QCM devices have attracted significant interest. Studies have taken advantage of both modalities to evaluate the thickness of polymer films [146] and biomolecule adsorption [147] [195]. However, the optical and acoustic responses are measured sequentially on

different devices, not at the same time on the same film. To eliminate the variations of the experimental conditions, a sensor that can record both the optical and acoustic signal simultaneously is essential. A hybrid sensor using a continuous thin film gold electrode on one side of a bulk-mode acoustic wave (BAW) sensor has been reported [155]. SPR detection was performed by monitoring the variation in the angle of the reflected light from the electrode [1] [148] [152] [155]. In this way, it is possible to determine the adsorbed mass. Localised surface plasmon resonance (LSPR) has the advantage that measurements are made by collecting spectra, and suitable equipment is widely available. The sensitivity of LSPR is comparable to SPR in biomolecule binding reactions.[34] Both LSPR sensor and QCM have great potential regarding to point-of-care (POC) tests. [180] [196] Hence, the following section reports the design of a hybrid sensor that integrates transmission-mode LSPR with a QCM, which can be useful for the analysis of immunological reactions, film structures and other biological absorption reactions.

## 6.2 QCM Design

A schematic of the hybrid LSPR and QCM sensor is shown in Figure 6.1. In contrast to traditional QCM devices that have continuous metallic films on both sides of the piezoelectric material, the device used in this work has a 400  $\mu\text{m}$  diameter window defined in the back electrode and a 400  $\mu\text{m} \times 400 \mu\text{m}$  array of Au LSPR nanodiscs patterned in the centre of the front electrode. The 400  $\mu\text{m}$  diameter was chosen to allow accurate alignment using the microspectrophotometer for measurement. The opening in the back metal electrode is necessary to allow visible light to pass through the device. AT-cut quartz crystal wafers with a diameter of 13.6 mm and a fundamental resonant frequency of ~5 MHz were purchased from ICM Co. Inc. The LSPR nanostructures and QCM electrodes were fabricated on the quartz substrates using electron beam lithography and photolithography respectively. Figure 6.2 shows the experimental results comparing the QCM chip with continuous metallic electrodes and the hybrid LSPR and QCM device. The characterisation of a standard QCM chip and a modified QCM chip was done using an Agilent vector network analyser (VNA) E5071B. WinCal software was used to collect the return loss S11 spectra. The resonance frequency of the modified QCM device with LSPR structures on it shifts from 5.0058MHz to 5.0115MHz due to the loss of the metal mass at

the centre of the electrode (recall Equation 2.46). The hybrid LSPR and QCM chip has excellent performance with a Q factor increased by  $1 \times 10^4$  compared to the standard QCM which has a Q factor of  $5.5 \times 10^4$ .

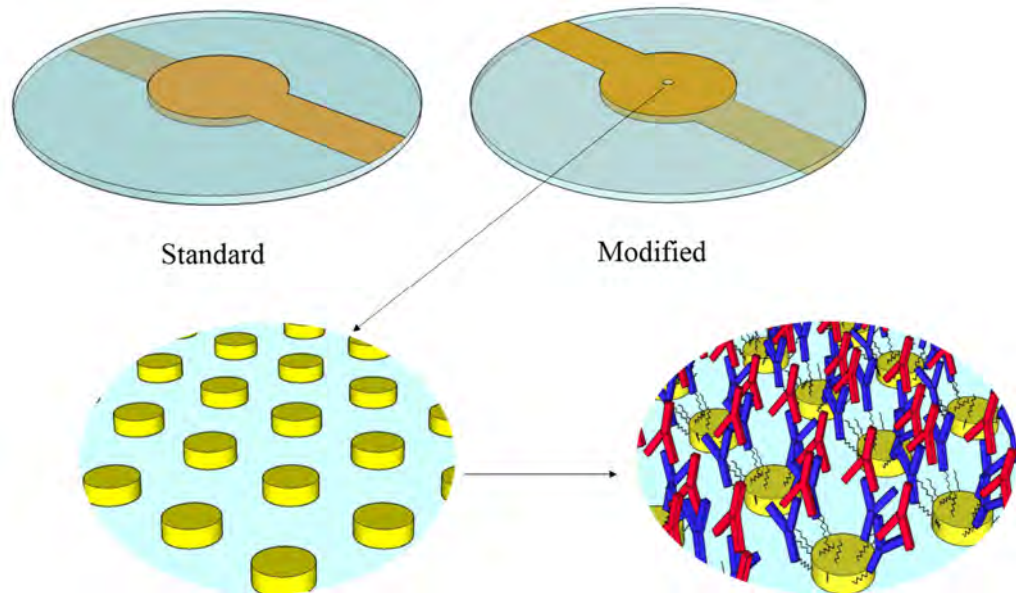


Figure 6.1. Schematic diagram of the modified QCM showing the antibody/antigen binding reaction attached to the Au LSPR nanostructures.

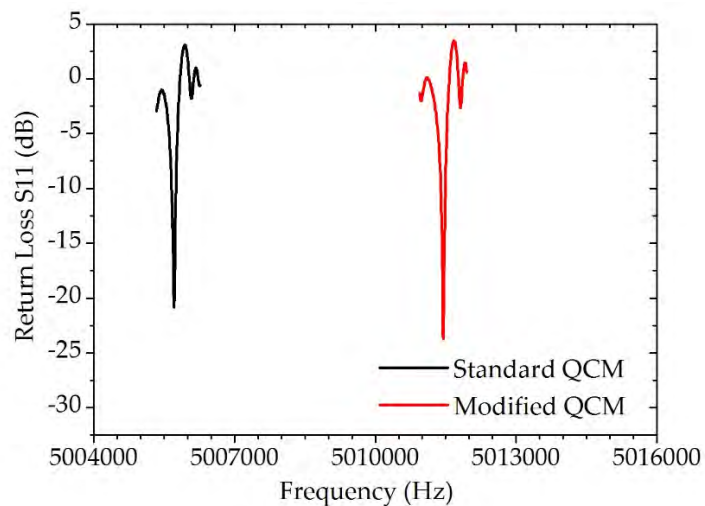


Figure 6.2 VNA measured return loss (S11) spectra of the standard QCM and hybrid LSPR and QCM

In order to verify that the modified QCM operated as expected, experiments were conducted using a glycerine-water solution. The QCM frequency were recorded and the analytical and experimental results are shown in Figure 6.3. Equation was used to calculate the theoretical frequency of the QCM.  $f_0=5$  MHz is set as the base resonant frequency of the crystal,  $\mu_q = 2.65$  g/cm<sup>3</sup> and  $\rho_q = 2.95 \times 10^{11}$  g/cm<sup>·s</sup><sup>2</sup> are the elastic modulus

and density of quartz, respectively.  $\eta_l$  and  $\rho_l$  are the viscosity and density of differing concentrations of glycerine-water solution and are given by Ref.[197].

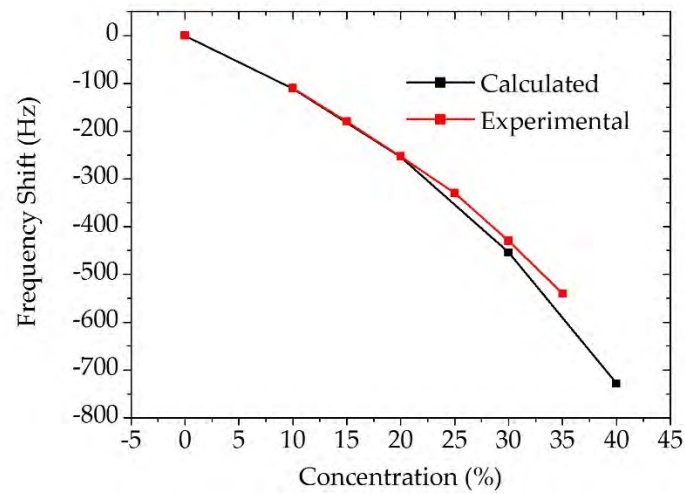


Figure 6.3 Frequency shift of the hybrid QCM versus increasing concentrations of glycerine-water solutions.

### 6.3 LSPR Design

A number of different Au nanostructures were simulated, fabricated and characterised on  $\text{SiO}_2$  substrates in Chapter 4. The design was tailored such that the resonant wavelength was in the 800 - 900 nm range as the spectra shows a larger sensitivity, shorter full width at half maximum (*i.e.* better FOM), and higher absorption intensity (transmission minimum). The optimised design has an array period of 450 nm and nanodisk diameter of 200 nm. The nanodisk array was fabricated on a blank QCM using the same fabrication and annealing process as described in Chapter 4. The measured transmission spectra can be seen in Figure 6.4. The refractive index of quartz is higher than borosilicate glass, as a result, the resonant wavelength shows a small red shift and a lower transmission comparing to borosilicate glass.

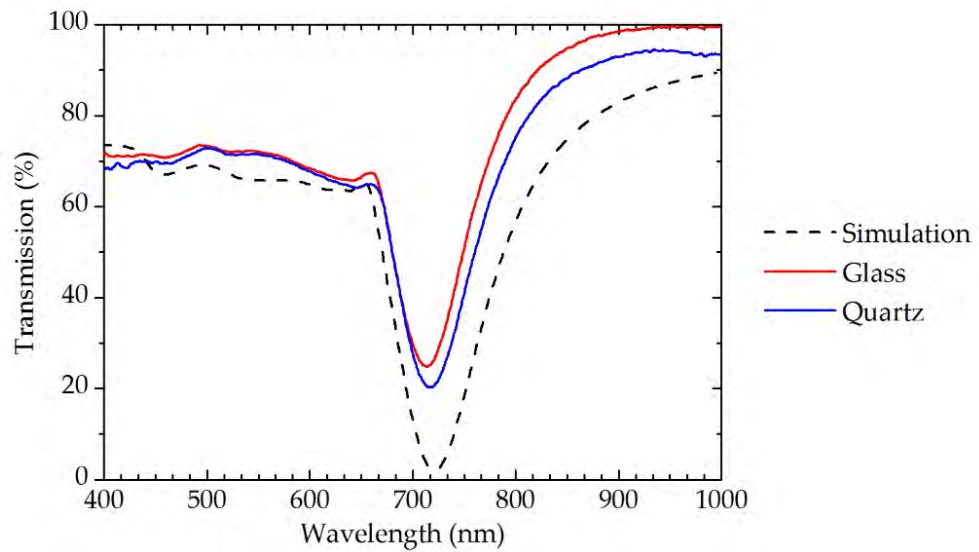


Figure 6.4 Simulated and measured transmission spectra of gold nanodisks on borosilicate glass and quartz substrate.

## 6.4 Fabrication

The hybrid LSPR and QCM device was fabricated on a 330  $\mu\text{m}$  quartz substrate as follows. The QCM electrodes were formed by evaporating a 10 nm/100 nm Ti/Au layer on to both sides of the quartz substrate using a standard photolithography and lift-off process described in Chapter 3. The round shape and size of the blank quartz crystal makes it very difficult to achieve accurate alignment between the gold electrode and the gold nanodisk array. In order to solve this problem, four global markers at the edge of the quartz crystal were employed. The large cross marker was used as a guide to locate the global markers in the EBL tool. Since they were far from the active region of the QCM, they didn't affect the performance of the QCM. The photomask design for top electrode is shown in Figure 6.5, the markers are used to locate the centre of the electrode. The photomask design of the back surface has the same electrode design but without the cross marker and the square markers.

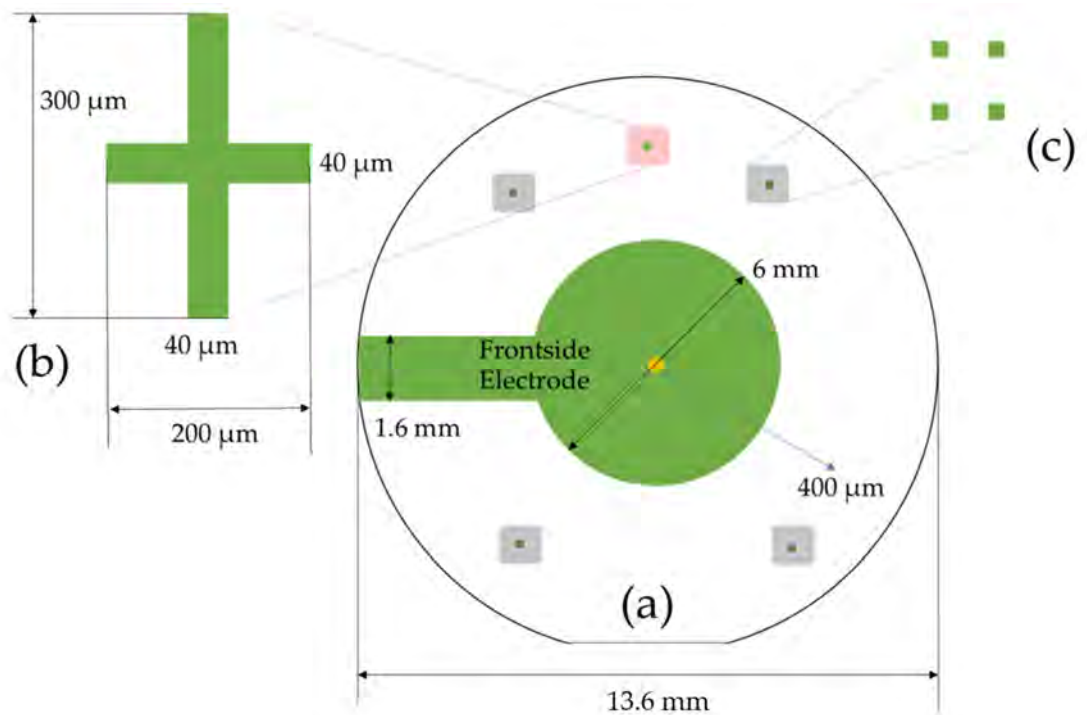


Figure 6.5 (a) Design of the pattern with the marker strategy for alignment in EBL. Yellow region is a small hole with a diameter of  $400\ \mu\text{m}$  allowing the transmission measurement and (b) enlarged image showing the cross design which is used as the origin for the global marker group (c) global marker group design: four  $40\ \mu\text{m} \times 40\ \mu\text{m}$  squares in a group. Four marker groups at four corners on the front and back surface.

After putting down the electrode pattern, a bi-layer PMMA ebeam resist were spin-coated on top of the sample and an Al conduction layer was evaporated on to the resist, which is following the same procedure as described in Chapter 4. Gold nanodisk array patterns were aligned and written in the yellow region in Figure 6.5 by EBL at a beam voltage of 100 kV. The multipixel method mentioned in Chapter 4 was adopted in the work. Quartz is also suitable for annealing so the post-fabrication annealing step was employed to reduce the imperfections in the fabricated devices.

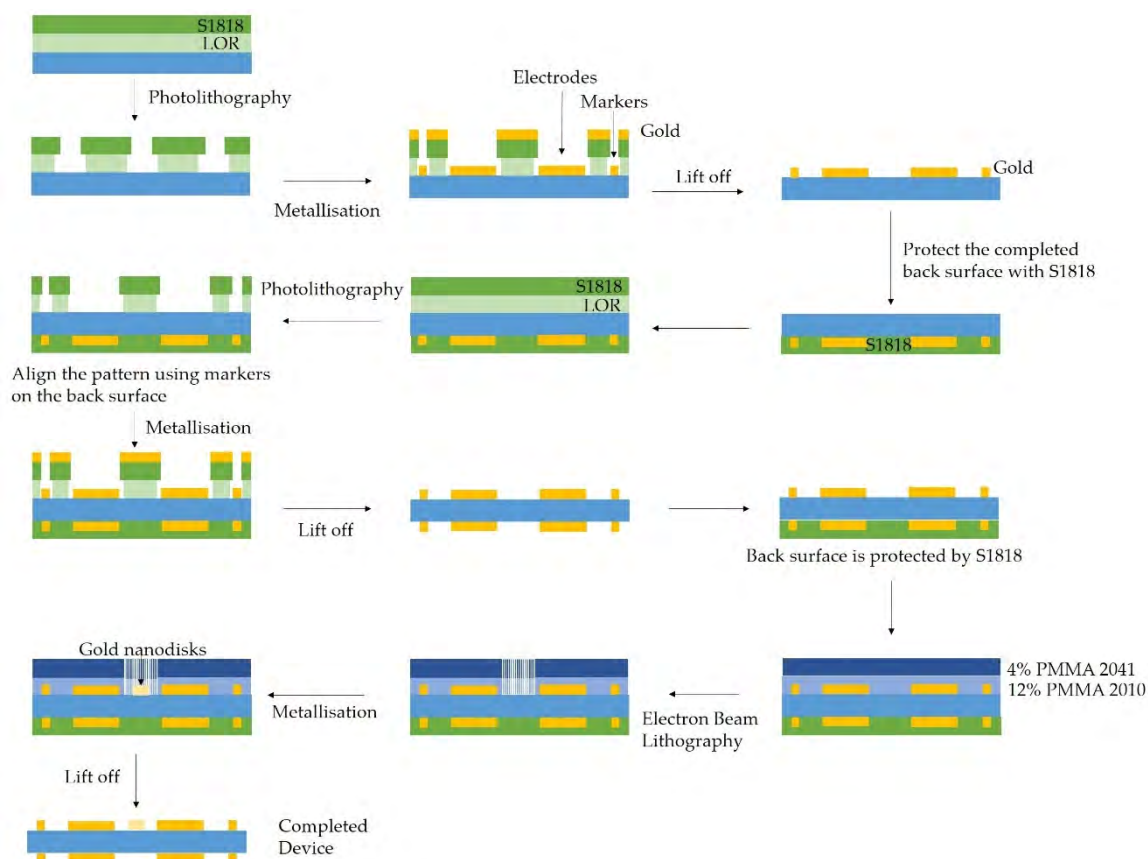


Figure 6.6 Fabrication process of the hybrid LSPR and QCM device.

## 6.5 Setup for the Simultaneous Recording

A measurement setup was constructed to monitor the LSPR and QCM signal simultaneously (Figure 6.7). A Harvard Pump 11 Elite syringe pump was set to deliver solutions at a flow rate of 0.18 mL/min. A polyethylene terephthalate (PET) flow cell was made in-house using a 3D printer. Silicone sealant was applied to seal the flow cell and minimise the mechanical stress in the crystal [198]. Finally, a glass slide was positioned on top of the flow cell to seal it.

Different to the previous two chapters, all the work described in this chapter used a Foster and Freeman ffTA microspectrometer to obtain the transmission spectra. The lens objective has a numerical aperture of 0.1 and magnification of 4 $\times$ . The microspectrometer measurement area is 12.5  $\mu\text{m}$  in diameter. Unpolarised light from a halogen lamp was normally incident on to the backside of the modified QCM. The transmitted light that passes through the spectrometer is analysed and recorded by the ffTA software. By using an autoclick software, the interval between each spectral recording was set at 3 seconds; a

trade-off between the signal-to-noise ratio and recording speed. The scan time of the spectrometer was 0.4 sec and the spectral averaging number was set as 5.

The hybrid QCM chip (working crystal in Crystal Holder 1) and the reference crystal (Crystal holder 2) were incorporated into an in-house made frequency comparison PCB (Figure 6.8). The working principle was presented in Chapter 3. A Tektronix TDS2000C oscilloscope and LabVIEW SignalExpress software were used to automatically record the frequency shift in real-time.

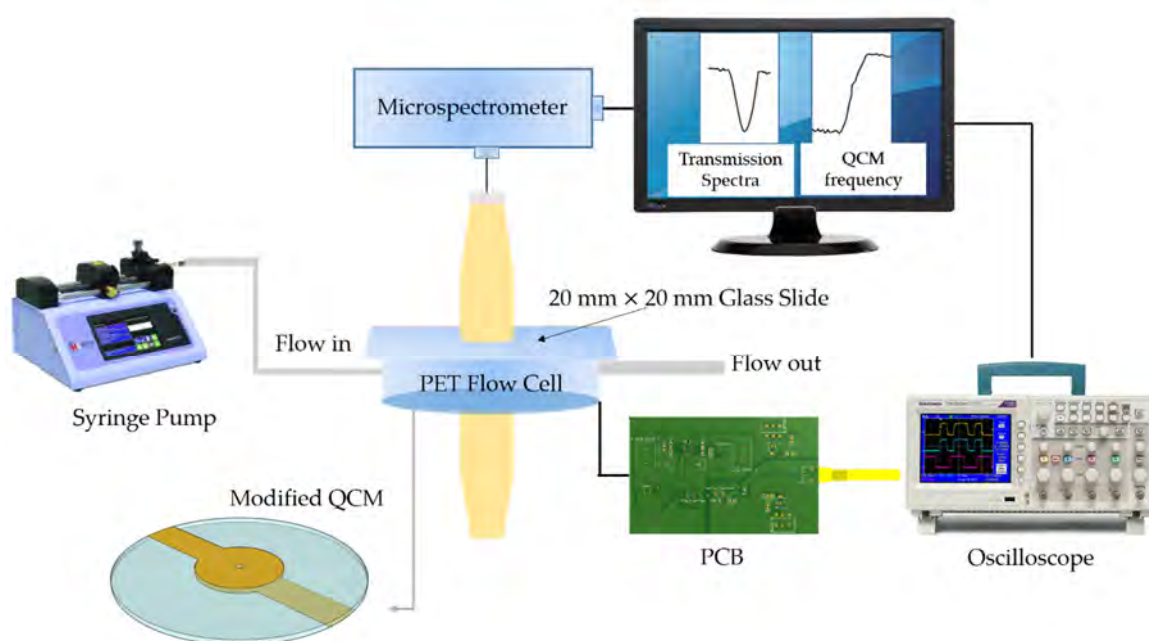


Figure 6.7 Schematic diagram of the combined QCM and LSPR instrument setup.

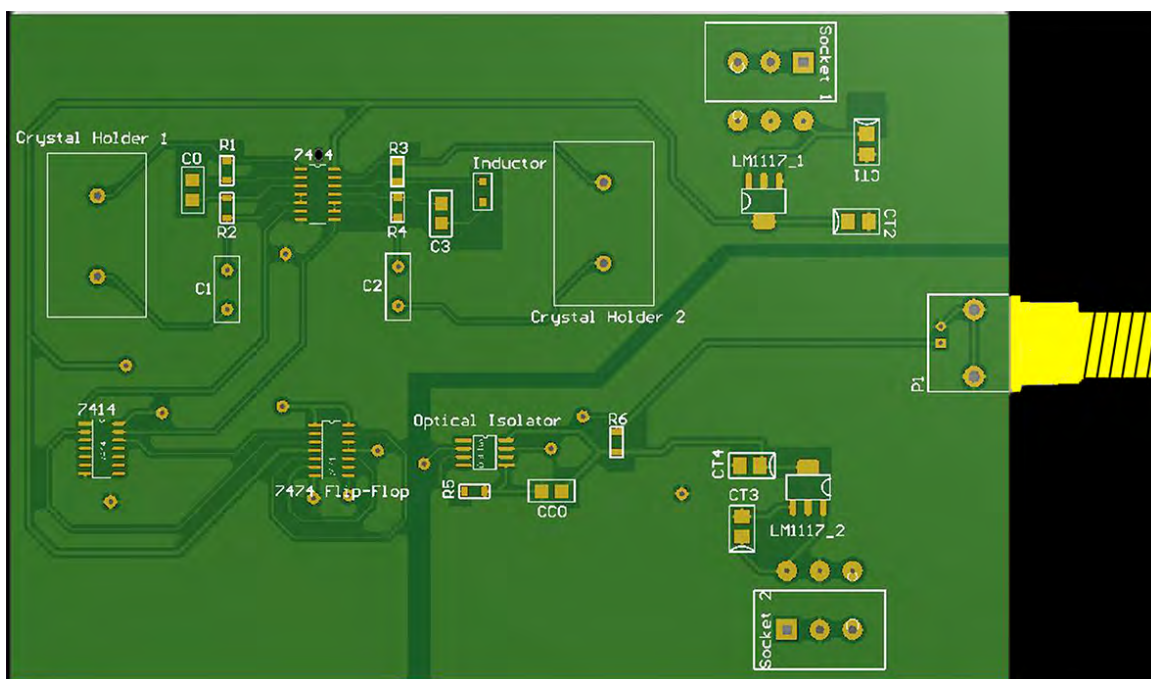


Figure 6.8 Layout of the frequency comparison PCB

The computer simultaneously ran two pieces of recording software: fftA software for the microspectrometer, and LabView program to acquire the QCM data and to synchronise the data acquisition.

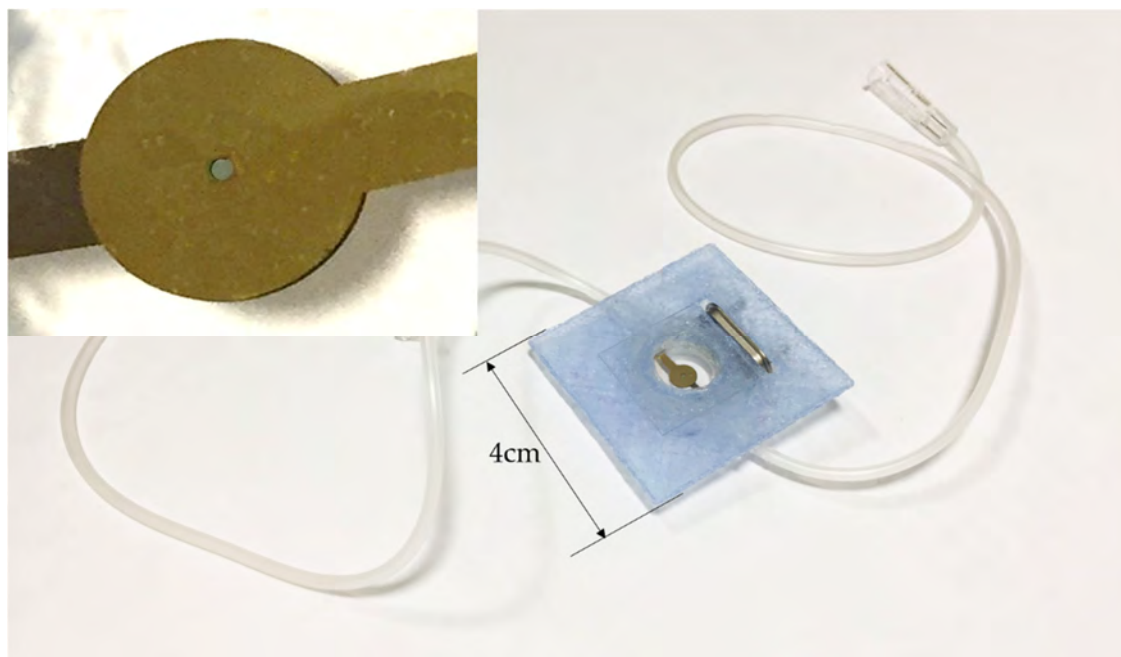


Figure 6.9 Photograph of the PET flow cell. Crystal holder model: HC-48/U. Inset image is a close-up photo of the top electrode and the nanodisk array in the centre.

## 6.6 Results and Discussion

All chemicals used in this work were of analytical-reagent grade and had been stated in Section 3.3. Anti-IgG antibodies (blue Y-shape molecule in Figure 6.1) were covalently immobilised on the sensing surface using the recipe stated in Chapter 3. During the first step, to ensure that the APTES is attached on the sensing surface, the QCM frequency was monitored using the VNA and the frequency decrement was 14.4Hz (averaged from three experiments). This agrees well with previously published work [199]. After step4 in Chapter 3, the cell was then rinsed using PBS and BSA was introduced for 15 minutes to block the surface for any unspecific binding of the antibody. After another rinse with PBS, the recording was initialised for basal resonant frequency stabilisation. The rabbit IgG (red Y-shape molecule in Figure 6.1) solution (10-100  $\mu\text{g/mL}$ ) was injected into the cell at a flow rate of 0.18 mL/min and the LSPR transmission shift and the QCM frequency change were continuously monitored. On completion of the experiment, the chip surface was regenerated using a 10 min 150W oxygen plasma treatment. The experiments for all concentrations have been repeated three times and averaged. The standard deviation for each concentration and each sensing techniques can be found in Table 6.1.

	100 $\mu\text{g/mL}$	50 $\mu\text{g/mL}$	25 $\mu\text{g/mL}$	10 $\mu\text{g/mL}$	0 $\mu\text{g/mL}$
QCM (Hz)	2.0	4.4	2.1	3.4	3.5
LSPR (nm)	0.16	0.13	0.11	0.08	0.05

Table 6.1 The standard deviation for each concentration and each sensing techniques.

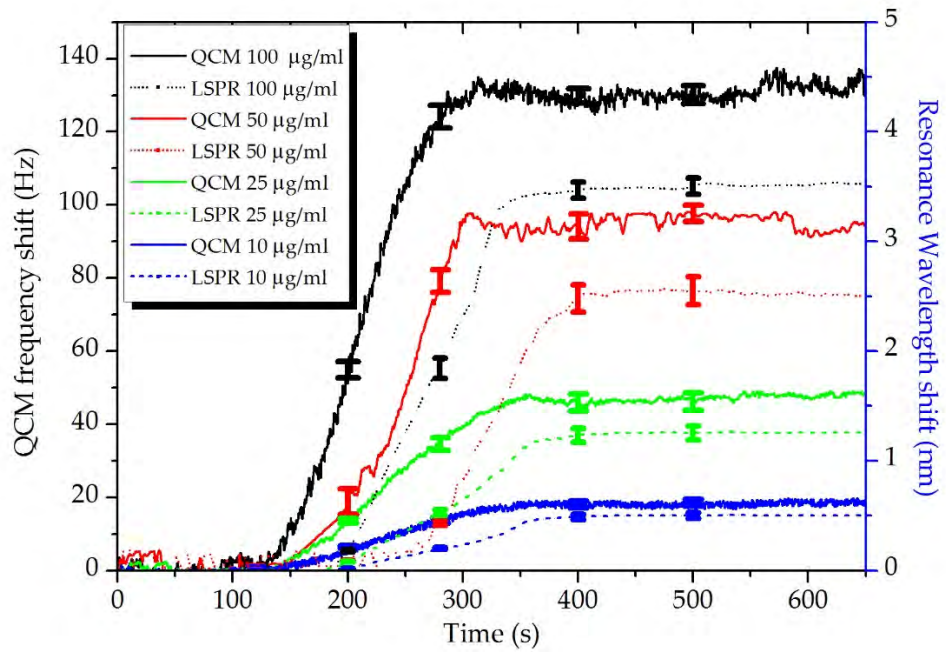


Figure 6.10 Changes in QCM frequency (line) and LSPR resonance wavelength (dotted line) versus time. Rabbit IgG was injected at  $t = 100$  s.

As can be seen in Figure 6.10, after introducing IgG molecules into the flow cell, both the LSPR wavelength and QCM signal increase, and the correlation can be made between the QCM frequency shift and the LSPR resonance wavelength shift (see Figure 6.11). The linear range of the sensor is between 10-50  $\mu\text{g/mL}$  and the limit of detection (LOD) is 5  $\mu\text{g/mL}$  for QCM and 1.88  $\mu\text{g/mL}$  for LSPR measurements. The adsorbed mass measured by the QCM is 1593  $\text{ng cm}^{-2}$  (calculated using Equation 2.44) for 50  $\mu\text{g/mL}$  IgG solution. Since IgG binds to anti-IgG in the 2 to 1 binding model, the result here is in good agreement with twice of the value( 726  $\text{ng cm}^{-2}$ ) in the published literature [200].

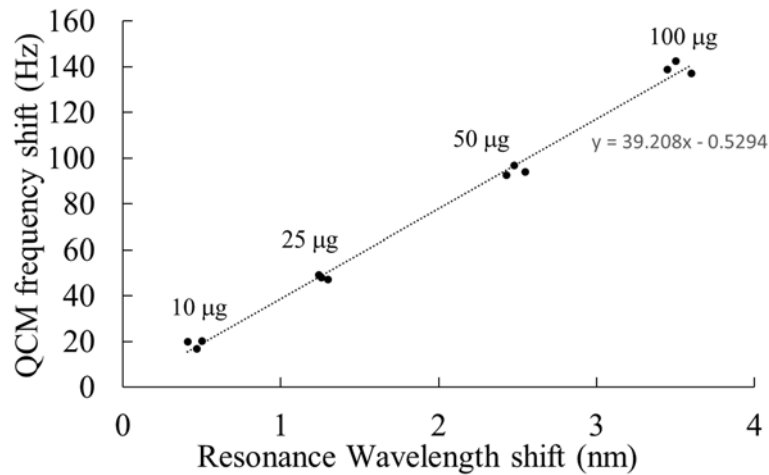


Figure 6.11 End point QCM frequency shift versus resonance wavelength shift for different concentrations of IgG, demonstrating the linear relationship between QCM and LSPR in our experiments.

$K_d$ , the dissociation constant, is widely used to describe the affinity between the antibody and its antigen. It can be calculated by fitting the analyte concentration and the corresponding signal shift into the Hill equation. The Hill equation is used to describe the fraction of a macromolecule saturated by the ligand as a function of the ligand concentration:

$$\theta = \frac{[L]^n}{K_d + [L]^n} = \frac{[L]^n}{(K_A)^n + [L]^n} = \frac{1}{\left(\frac{K_A}{[L]}\right)^n + 1}$$

where  $\theta$  is the fraction of the receptor protein concentration that is bound to the ligand,  $[L]$  is the unbound ligand concentration,  $K_d$  is the equilibrium dissociation constant of the ligand-receptor complex, which is equal to the ratio of the dissociation rate of the ligand-receptor complex to its association rate:  $K_d = \frac{k_{dissociation}}{k_{association}}$ ,  $K_A$  is the ligand concentration, at which half the receptors are ligand-bound.  $K_A$  is defined as  $(K_A)^n = K_d = \frac{k_{dissociation}}{k_{association}}$  and is also known as the microscopic disassociation constant.  $n$  is the Hill coefficient (or Hill slope factor).  $K_d$  is treated as a measure for the affinity of the ligand to the receptor: a smaller  $K_d$  means a greater affinity.

To characterise the sensor's sensitivity, the  $K_d$  was calculated for the antibody-antigen binding reaction. The data of the QCM and LSPR measurement was plotted in Figure 6.12 and fitted to the Hill equation using GraphPad Prism software, whereas the calculated dissociation constant of the reaction is  $6.67 \times 10^{-7}$  M for QCM and  $7.62 \times 10^{-7}$  M for LSPR.

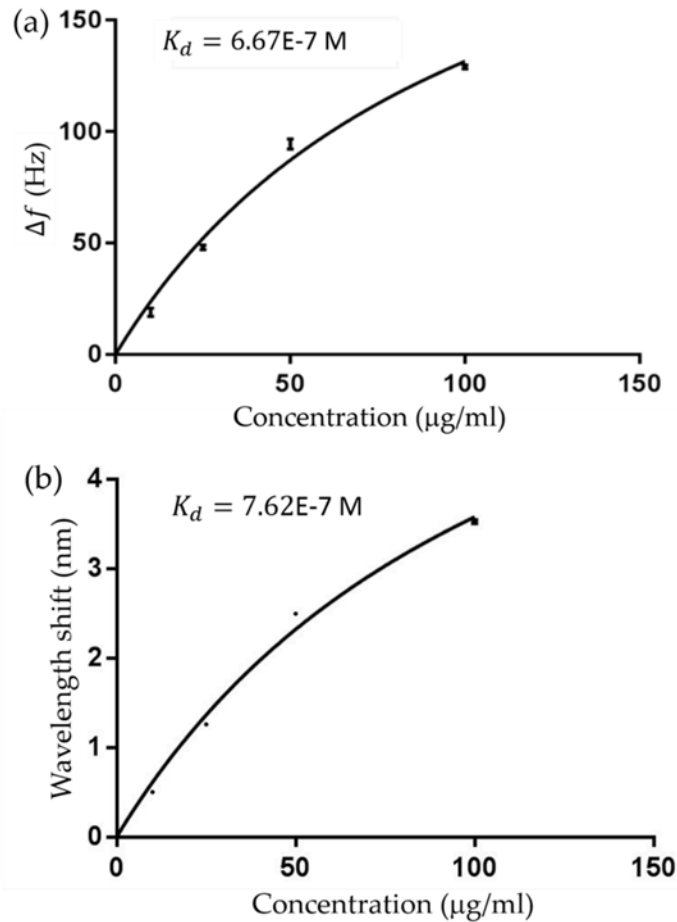


Figure 6.12 The endpoint of the (a) QCM frequency shift,  $f$ , and (b) LSPR resonant wavelength shift, as a function of IgG concentration was plotted and fitted to the Hill equation. The calculated dissociation constant of the reaction was  $6.67 \times 10^{-7}\text{ M}$  for QCM and  $7.62 \times 10^{-7}$  for LSPR.

We can also see from Figure 6.10 that the QCM signal starts changing in the first few seconds after the introduction of the antigen while the LSPR response has a  $\sim 40$  secs delay. The LSPR signal change is slower than the QCM shift for two primary reasons. The analyte is introduced at a distance of  $\sim 7$  mm from where the LSPR structures reside. The analyte must diffuse to the Au nanodisc region and bind with the LSPR structures to illicit a change in the LSPR wavelength. In contrast, the QCM measures the area-average result therefore it shows a response as soon as the binding action starts at the edge of the gold electrode. Secondly, as shown in Figure 4.17 in Section 4.1.5, the electric field distribution suggests that part of the LSPR-active region is at the bottom of the gold nanodiscs. The introduced antigen must bind to the antibodies residing on these regions to obtain the full LSPR response.

The hybrid sensor has been compared with three commonly used techniques, QCM, LSPR and SPR, in terms of detection time, linear range, and limit of detection (LOD). The LOD for the hybrid sensor was calculated using the formula  $LOD = (3 \times SD)/k$ , where  $SD$  stands for standard deviation of a blank control, and  $k$  is the slope of the response curve in the linear range.

The detection target of the LSPR sensor [201] is anti-IgG while the others' detection targets are the same to the hybrid sensor. As can see in the table, the detection time and linear range of our sensor are comparable to the published works.

	Detection Time	Linear range	LOD	
			QCM	LSPR
Hybrid sensor	8min	10-50 $\mu\text{g/mL}$	5.5 $\mu\text{g/mL}$	2.1 $\mu\text{g/mL}$
QCM [199]	30min	up to 20 $\mu\text{g/mL}$	3.3 $\mu\text{g/mL}$	
LSPR [201]	5min	0-50 $\mu\text{g/mL}$	0.3 $\mu\text{g/mL}$	
Commercial SPR instrument [202]	5min	10 -150 $\mu\text{g/mL}$	2.36 $\mu\text{g/mL}$	

Table 6.2 Table for comparing hybrid sensor to other sensing technologies.

## 6.7 Summary

We have demonstrated the simultaneous measurement capabilities of a hybrid sensor that integrates a transmission-mode LSPR sensor with a QCM sensor. The device provides a versatile tool for studying dynamic processes in biomolecular reactions and thin films. The measurement platform can be further improved to include a QCM dissipation measurement or choosing a QCM that operate at a higher frequency to obtain higher sensitivity. Moreover, the costly and bulky equipment required to detect the LSPR and QCM signal (spectrometer and VNA respectively) could be replaced by Si pn diodes and thin film bulk acoustic resonators resulting in a low-cost, portable, hybrid LSPR and QCM device, which is suitable for POC diagnostics.

# 7. Conclusions and Future Work

In this thesis, LSPR gold nanodisk arrays on both common piezo inactive material and piezoelectric material have been designed, simulated, fabricated and characterised. Based on the results from the nanostructures on SiO<sub>2</sub>, the gold nanodisk arrays have been combined with QCM to develop a new hybrid biosensing device. The LSPR gold nanodisk array has been fabricated on piezoelectric LiNbO<sub>3</sub> substrate which supports SAW sensing and SAW streaming. This chapter concludes the development of the LSPR on two different substrates and the hybrid LSPR and QCM device, and includes some discussion for future work.

## 7.1 LSPR Biosensor on SiO<sub>2</sub>

LSPR gold nanodisk arrays were simulated using Lumerical FDTD solutions. The array periods and disk size were scaled to create 12 designs in the wavelength range from 400 nm to 1  $\mu$ m. The gold nanodisk arrays were fabricated on the SiO<sub>2</sub> substrate using electron beam lithography (EBL) and lift off process. The effect of post-fabrication annealing was presented in this chapter as well. The bumpy surface and the rough sidewall of the nanodisk after fabrication was improved after annealing and the resultant spectral characteristics become closer to those observed in the simulated results. A 'multipixel' method was tested and almost halved the ebeam time for writing the nanodisks.

The effect of changing the geometry of the nanostructure, the diameter of the disk diameter and the array period, was discussed using simulation and experimental results. Keeping the diameter fixed at 200 nm and increasing the array period from 300 nm to 600 nm resulted in the resonant wavelength red shifting from 600 nm to 850 nm and an increase in the peak transmission intensity. Keeping the array period as 450 nm, when increasing the nanodisk diameter, the resonance wavelength showed a red shift and a decrease in the transmission. It is also demonstrated that there is correlation between the resonance wavelength and the transmission spectra linewidth.

The sensitivity, *i.e.* the wavelength shift per refractive index unit change, of nanodisk array designs were characterised using varying concentrations of glycerine water solution. It

was shown that the resonance at a longer wavelength has higher sensitivity. Due to the correlation between the resonance wavelength and the transmission spectra line width, there is a trade-off between the sensitivity and the spectral resolution. Figure of merit (FOM) of LSPR sensor, sensitivity over the linewidth of the LSPR transmission dip, was calculated. By comparing the sensitivity and FOM of different designs, three designs showed excellent performance. Considering the transmission intensity of these designs, which is also important for discriminating spectra, the design with 450 nm array period and 200 nm disk diameter demonstrated the best performance. The simulated electric field distribution showed the sensitive region of the LSPR sensor and suggested that when the difference between the refractive indices of the substrate and top dielectric environment is small, the two modes on the top and bottom will merge together and shows a stronger resonance.

Finally, an immunoassay was conducted on the LSPR sensing surface using protein A and IgG's non-specific binding reaction, demonstrating that the LSPR sensor has great potential in biosensing.

## 7.2 LSPR Nanodisks on LiNbO<sub>3</sub>

Au nanodisk array designs with different array period and disk diameters were simulated on a LiNbO<sub>3</sub> substrate. After changing the dielectric environment from air to water, the simulated transmission spectra showed two resonance modes: a LiNbO<sub>3</sub> mode which is caused by the LSPR at the interface of the LiNbO<sub>3</sub> substrate and the metal; a liquid mode which is caused by the LSPR at the interface of the dielectric environment and the metal. These two modes are produced by the big difference between the refractive index of the liquid layer and the substrate.

The sensitivity of both modes was characterised using glycerine/water solution. It was found that the resonance wavelength of both modes showed a red shift when increasing the environmental refractive index. The liquid (top) mode has a larger sensitivity (165 nm/RIU) than the LiNbO<sub>3</sub> (bottom) mode (130 nm/RIU). This is due to the fact that the LSPR active region of the liquid mode is completely inside the solution, whereas LiNbO<sub>3</sub> mode it is mostly inside the substrate.

The birefringence of LiNbO<sub>3</sub> was studied by simulation and experiments. Glycerine/water solutions were injected on top of the sensing surface, and the simulation and experiments was conducted using a polarised light beam. The results showed that the top mode is not affected by the polarisation of the incident light, thus not sensitive to the birefringence of the substrate. It is suggested that the LSPR sensor design on high refractive index and anisotropic material should target the liquid mode.

A design of gold nanodisk on LiNbO<sub>3</sub> targeting the liquid mode was simulated, fabricated and characterised. The sensitivity of the design is 216 nm/RIU which is similar to the design on SiO<sub>2</sub> in the same wavelength range. The linewidth of the transmission spectra is broader than that on SiO<sub>2</sub>, due to the fabrication imperfections and the strong internal reflection between LiNbO<sub>3</sub> and the liquid layer.

### 7.3 Hybrid LSPR and QCM Biosensor

The design of the gold nanodisks on quartz was investigated on a glass substrate in Chapter 5. After fabricating the gold nanodisks design on a quartz substrate, it was characterised and showed similar performance as on a glass substrate. The modified QCM design was characterised using a vector network analyser (VNA), the quality factor increased from  $5.5 \times 10^4$  to  $6.5 \times 10^4$  due to the loss of the metal mass at the centre of the electrode. The performance of the modified QCM was verified using the glycerine-water solution and measured frequency shifts are in good agreement with the calculated theoretical results. The designed Au nanodisk array was fabricated on the 400  $\mu\text{m}$  diameter opening at the centre of the modified QCM top electrode. The back electrode also had an opening in the centre to allow transmission measurements.

An immunoassay was conducted on the sensing surface of the hybrid sensor. The first APTES layer immobilisation gave a frequency shift of 14.4 Hz which agrees with previous published work. Following the immobilisation of anti-IgG, different concentration IgG solution was injected into the flow cell. QCM and LSPR data was recorded simultaneously for the surface adsorption process. The correlation was made between the QCM frequency shift and the LSPR resonance wavelength shift. The linear range of the sensor is between 10-50  $\mu\text{g/mL}$ , and the limit of detection (LOD) is 5  $\mu\text{g/mL}$  for QCM and 1.88  $\mu\text{g/mL}$  for LSPR measurements. These parameters were compared with other sensing technologies

and show that the detection time and linear range of our sensor are comparable to the published works.

#### 7.4 Future Work

The focus of the work presented in this thesis was placed on the development of a hybrid biosensor through integration of plasmonic sensing and acoustic sensing techniques. There is still some unfulfilled potential associated with this work.

In Chapter 4, effects of changing the gold nanodisk array geometry in the *xy*-plane (array period and disk sizes) were investigated. Some simulation work was done to investigate the effect of changing the thickness of the nanodisks. The next step should be the fabrication and characterisation of different thickness of nanodisk arrays, with the intention to further improve their sensing performance. However, the gold nanodisk is not the most sensitive structure in the visible wavelength range. Some other shapes of nanostructure show higher sensitivity also worth investigating such as nanorods, nanoprisms, nanospheres, *etc* [178] [36] [177]. The LSPR sensor working in infrared range can also be investigated since theoretically they have a larger sensitivity than those working in visible range [203] [204].

As shown in Section 4.1.4.2 and detailed in the caption of Figure 4.14, there is difference between the simulated and measured intensity at the resonance wavelength. It is likely to be caused by the difference between the optical properties of the evaporated gold and the bulk values used in the simulation software's database. In future, ellipsometry could be used to acquire the optical properties of the evaporated gold [205]. Then the measured optical constants can be imported into the simulation software to make it better resemble to the measured results.

As discussed in Chapter 5, the next step would be the integration of LSPR sensor with surface acoustic wave (SAW) sensing technique or SAW streaming. The current fabrication process of LSPR nanostructure can also be used for fabricating interdigital transducers (IDT), which can generate SAW on piezoelectric material. The dual LSPR modes on high refractive index material also applies for LiTaO<sub>3</sub>, another popular piezoelectric material. It should be helpful to study the LSPR phenomenon on LiTaO<sub>3</sub> [206].

As shown in Chapter 7, the sensitivity, limit of detection of the hybrid sensor is not as good as the individual technique. Further work could be conducted to improve the performance of the hybrid sensor. Future work could also incorporate the dissipation measurement of the QCM [143]. The costly and bulky measurements tools can be replaced by other miniaturised technologies to make the device into a low-cost and portable format [137][174] [198][207].

# Bibliography

- [1] Y. Zong, F. Xu, X. Su, and W. Knoll, "Quartz Crystal Microbalance with Integrated Surface Plasmon Grating Coupler," *Anal. Chem.*, vol. 80, no. 13, pp. 5246–5250, Jul. 2008.
- [2] B. Sepúlveda, P. C. Angelomé, L. M. Lechuga, and L. M. Liz-Marzán, "LSPR-based nanobiosensors," *Nano Today*, vol. 4, no. 3, pp. 244–251, Jun. 2009.
- [3] S. Unser, I. Bruzas, J. He, and L. Sagle, "Localized Surface Plasmon Resonance Biosensing: Current Challenges and Approaches," *Sensors*, vol. 15, no. 7, pp. 15684–15716, Jul. 2015.
- [4] D. J. Griffiths and C. Inglefield, "Introduction to Electrodynamics," *Am. J. Phys.*, vol. 73, no. 6, pp. 574–574, Jun. 2005.
- [5] R. W. Wood, "On a Remarkable Case of Uneven Distribution of Light in a Diffraction Grating Spectrum," *Proc. Phys. Soc. London*, vol. 18, no. 1, pp. 269–275, Jun. 1902.
- [6] L. Rayleigh, "On the Dynamical Theory of Gratings," *Proc. R. Soc. A Math. Phys. Eng. Sci.*, vol. 79, no. 532, pp. 399–416, Aug. 1907.
- [7] J. Strong, "Effect of Evaporated Films on Energy Distribution in Grating Spectra," *Phys. Rev.*, vol. 49, no. 4, pp. 291–296, Feb. 1936.
- [8] U. Fano, "The Theory of Anomalous Diffraction Gratings and of Quasi-Stationary Waves on Metallic Surfaces (Sommerfeld's Waves)," *J. Opt. Soc. Am.*, vol. 31, no. 3, p. 213, Mar. 1941.
- [9] R. Ritchie, E. Arakawa, J. Cowan, and R. Hamm, "Surface-Plasmon Resonance Effect in Grating Diffraction," *Phys. Rev. Lett.*, vol. 21, no. 22, pp. 1530–1533, Nov. 1968.
- [10] H. L. Lord, W. Zhan, and J. Pawliszyn, "Fundamentals and applications of needle trap devices," *Anal. Chim. Acta*, vol. 677, no. 1, pp. 3–18, Sep. 2010.
- [11] H. Raether, *Surface Plasmons on Smooth and Rough Surfaces and on Gratings*, vol. 111. Berlin, Heidelberg: Springer Berlin Heidelberg, 1988.
- [12] S. Raine, *Surface Plasmon Nanophotonics*, vol. 131, no. 404–405. Dordrecht: Springer Netherlands, 2007.
- [13] J. M. Brockman, B. P. Nelson, and R. M. Corn, "Surface Plasmon Resonance Imaging Measurements of Ultrathin Organic Films," *Annu. Rev. Phys. Chem.*, vol. 51, no. 1, pp. 41–63, Oct. 2000.
- [14] W. Knoll, "INTERFACES AND THIN FILMS AS SEEN BY BOUND ELECTROMAGNETIC WAVES," *Annu. Rev. Phys. Chem.*, vol. 49, no. 1, pp. 569–638, Oct. 1998.
- [15] H. Knobloch, H. Brunner, A. Leitner, F. Aussenegg, and W. Knoll, "Probing the evanescent field of propagating plasmon surface polaritons by fluorescence and Raman spectroscopies," *J. Chem. Phys.*, vol. 98, no. 12, pp. 10093–10095, Jun. 1993.

- [16] W. L. Barnes, A. Dereux, and T. W. Ebbesen, "Surface plasmon subwavelength optics," *Nature*, vol. 424, no. 6950, pp. 824–830, Aug. 2003.
- [17] W. L. Barnes, "Surface plasmon–polariton length scales: a route to sub-wavelength optics," *J. Opt. A Pure Appl. Opt.*, vol. 8, no. 4, pp. S87–S93, Apr. 2006.
- [18] B. Gupta, A. Shrivastav, and S. Usha, "Surface Plasmon Resonance-Based Fiber Optic Sensors Utilizing Molecular Imprinting," *Sensors*, vol. 16, no. 9, p. 1381, Aug. 2016.
- [19] C. Nylander, B. Liedberg, and T. Lind, "Gas detection by means of surface plasmon resonance," *Sensors and Actuators*, vol. 3, no. C, pp. 79–88, Jan. 1982.
- [20] B. Liedberg, C. Nylander, and I. Lunström, "Surface plasmon resonance for gas detection and biosensing," *Sensors and Actuators*, vol. 4, pp. 299–304, Jan. 1983.
- [21] L. Verslegers, P. B. Catrysse, Z. Yu, J. S. White, E. S. Barnard, M. L. Brongersma, and S. Fan, "Planar Lenses Based on Nanoscale Slit Arrays in a Metallic Film," *Nano Lett.*, vol. 9, no. 1, pp. 235–238, Jan. 2009.
- [22] Q. Chen and D. R. S. Cumming, "Subwavelength light focusing demonstrated by plasmonic lenses based on nano-slits in an aluminium film," in *2010 IEEE Photonic Society's 23rd Annual Meeting*, 2010, vol. 18, no. 14, pp. 391–392.
- [23] Werayut Srituravanich, "Plasmonic Nanolithography," pp. 1–4, 2007.
- [24] S. Seo, H. C. Kim, H. Ko, and M. Cheng, "Subwavelength proximity nanolithography using a plasmonic lens," *J. Vac. Sci. Technol. B Microelectron. Nanom. Struct.*, vol. 25, no. 6, p. 2271, 2007.
- [25] I. Freestone, N. Meeks, M. Sax, and C. Higgitt, "The Lycurgus Cup – A Roman nanotechnology," *Gold Bull.*, vol. 40, no. 4, pp. 270–277, Dec. 2007.
- [26] M. I. Stockman, "Nanoplasmonics: The physics behind the applications," *Phys. Today*, vol. 64, no. 2, pp. 39–44, Feb. 2011.
- [27] A. J. Haes, C. L. Haynes, A. D. McFarland, G. C. Schatz, R. P. Van Duyne, and S. Zou, "Plasmonic Materials for Surface-Enhanced Sensing and Spectroscopy," *MRS Bull.*, vol. 30, no. 5, pp. 368–375, May 2005.
- [28] K. L. Kelly, E. Coronado, L. L. Zhao, and G. C. Schatz, "The Optical Properties of Metal Nanoparticles: The Influence of Size, Shape, and Dielectric Environment," *J. Phys. Chem. B*, vol. 107, no. 3, pp. 668–677, Jan. 2003.
- [29] L. J. Sherry, S.-H. Chang, G. C. Schatz, R. P. Van Duyne, B. J. Wiley, and Y. Xia, "Localized Surface Plasmon Resonance Spectroscopy of Single Silver Nanocubes," *Nano Lett.*, vol. 5, no. 10, pp. 2034–2038, Oct. 2005.
- [30] M. Faraday, "The Bakerian Lecture: Experimental Relations of Gold (and Other Metals) to Light," *Philos. Trans. R. Soc. London*, vol. 147, no. 0, pp. 145–181, Jan. 1857.
- [31] G. Mie, "Beiträge zur Optik trüber Medien, speziell kolloidaler Metallösungen," *Ann. Phys.*, vol. 330, no. 3, pp. 377–445, 1908.
- [32] H. Horvath, "Gustav Mie and the scattering and absorption of light by particles: Historic developments and basics," *J. Quant. Spectrosc. Radiat. Transf.*, vol. 110, no.

- 11, pp. 787–799, Jul. 2009.
- [33] U. Kreibig and P. Zacharias, “Surface plasma resonances in small spherical silver and gold particles,” *Zeitschrift für Phys. A Hadron. Nucl.*, vol. 231, no. 2, pp. 128–143, Apr. 1970.
- [34] K. A. Willets and R. P. Van Duyne, “Localized Surface Plasmon Resonance Spectroscopy and Sensing,” *Annu. Rev. Phys. Chem.*, vol. 58, no. 1, pp. 267–297, May 2007.
- [35] A. J. Haes and R. P. Van Duyne, “A Nanoscale Optical Biosensor: Sensitivity and Selectivity of an Approach Based on the Localized Surface Plasmon Resonance Spectroscopy of Triangular Silver Nanoparticles,” *J. Am. Chem. Soc.*, vol. 124, no. 35, pp. 10596–10604, Sep. 2002.
- [36] J. Cao, T. Sun, and K. T. V. Grattan, “Gold nanorod-based localized surface plasmon resonance biosensors: A review,” *Sensors Actuators B Chem.*, vol. 195, pp. 332–351, May 2014.
- [37] W. Yang, J. Hulteen, G. C. Schatz, and R. P. Van Duyne, “A surface-enhanced hyper-Raman and surface-enhanced Raman scattering study of trans -1,2-bis(4-pyridyl)ethylene adsorbed onto silver film over nanosphere electrodes. Vibrational assignments: Experiment and theory,” *J. Chem. Phys.*, vol. 104, no. 11, pp. 4313–4323, Mar. 1996.
- [38] K. M. Mayer and J. H. Hafner, “Localized Surface Plasmon Resonance Sensors,” *Chem. Rev.*, vol. 111, no. 6, pp. 3828–3857, Jun. 2011.
- [39] B. T. Draine and P. J. Flatau, “Discrete-Dipole Approximation For Scattering Calculations,” *J. Opt. Soc. Am. A*, vol. 11, no. 4, p. 1491, Apr. 1994.
- [40] A. Taflove and S. C. Hagness, *Computational Electrodynamics: The Finite-difference Time-domain Method*. Artech House, 2005.
- [41] T. W. Ebbesen, H. J. Lezec, H. F. Ghaemi, T. Thio, and P. A. Wolff, “Extraordinary optical transmission through sub-wavelength hole arrays,” *Nature*, vol. 391, no. 6668, pp. 667–669, Feb. 1998.
- [42] H. A. Bethe, “Theory of Diffraction by Small Holes,” *Phys. Rev.*, vol. 66, no. 7–8, pp. 163–182, Oct. 1944.
- [43] Q. Chen and D. R. S. Cumming, “High transmission and low color cross-talk plasmonic color filters using triangular-lattice hole arrays in aluminum films,” *Opt. Express*, vol. 18, no. 13, p. 14056, Jun. 2010.
- [44] A. De Leebeek, K. Kumar, A. G. Brolo, R. Gordon, and D. Sinton, “On-chip Detection with Nanohole Arrays,” in *2006 Digest of the LEOS Summer Topical Meetings*, 2006, vol. 79, no. 11, pp. 54–55.
- [45] R. T. Beyer and D. R. Raichel, “Sounds of our times, two hundred years of acoustics,” *J. Acoust. Soc. Am.*, vol. 106, no. 1, pp. 15–16, Jul. 1999.
- [46] P. Dineva, D. Gross, R. Müller, and T. Rangelov, *Dynamic Fracture of Piezoelectric Materials*, vol. 212. Cham: Springer International Publishing, 2014.

- [47] J. Curie and P. Curie, "Phénomènes électriques des cristaux hémihédres à faces inclinées," *J. Phys. Théorique Appliquée*, vol. 1, no. 1, pp. 245–251, 1882.
- [48] K. Uchino, "The development of piezoelectric materials and the new perspective," in *Advanced Piezoelectric Materials*, Elsevier, 2010, pp. 1–85.
- [49] J. Valasek, "Piezo-Electric and Allied Phenomena in Rochelle Salt," *Phys. Rev.*, vol. 17, no. 4, pp. 475–481, Apr. 1921.
- [50] P. Transducers, A. A. Vives, and P. Transducers, *Piezoelectric Transducers and Applications*. Berlin, Heidelberg: Springer Berlin Heidelberg, 2008.
- [51] Y. Saigusa, "Quartz-based piezoelectric materials," in *Advanced Piezoelectric Materials*, Elsevier, 2010, pp. 171–203.
- [52] Lord Rayleigh, "On the Free Vibrations of an Infinite Plate of Homogeneous Isotropic Elastic Matter," *Proc. London Math. Soc.*, vol. s1-20, no. 1, pp. 225–237, Nov. 1888.
- [53] G. Sauerbrey, "Verwendung von Schwingquarzen zur Wägung dünner Schichten und zur Mikrowägung," *Zeitschrift für Phys.*, vol. 155, no. 2, pp. 206–222, Apr. 1959.
- [54] W. H. King, "Piezoelectric Sorption Detector.," *Anal. Chem.*, vol. 36, no. 9, pp. 1735–1739, Aug. 1964.
- [55] G. G. Guilbault, "Determination of formaldehyde with an enzyme-coated piezoelectric crystal detector," *Anal. Chem.*, vol. 55, no. 11, pp. 1682–1684, Sep. 1983.
- [56] G. G. Guilbault, J. M. Jordan, and E. Scheide, "Analytical Uses of Piezoelectric Crystals: A Review," *C R C Crit. Rev. Anal. Chem.*, vol. 19, no. 1, pp. 1–28, Jan. 1988.
- [57] M. E. Escuderos, S. Sánchez, and A. Jiménez, "Application of a Quartz Crystal Microbalance (QCM) System Coated with Chromatographic Adsorbents for the Detection of Olive Oil Volatile Compounds," *J. Sens. Technol.*, vol. 1, no. 1, pp. 1–8, 2011.
- [58] P. L. Konash and G. J. Bastiaans, "Piezoelectric crystals as detectors in liquid chromatography," *Anal. Chem.*, vol. 52, no. 12, pp. 1929–1931, Oct. 1980.
- [59] S. K. Vashist and P. Vashist, "Recent Advances in Quartz Crystal Microbalance-Based Sensors," *J. Sensors*, vol. 2011, no. 2, pp. 1–13, May 2011.
- [60] Janshoff, Galla, and Steinem, "Piezoelectric Mass-Sensing Devices as Biosensors-An Alternative to Optical Biosensors?," *Angew. Chem. Int. Ed. Engl.*, vol. 39, no. 22, pp. 4004–4032, Nov. 2000.
- [61] Y. J. Montagut, J. V. García, Y. Jiménez, C. March, A. Montoya, and A. Arnau, "Frequency-shift vs phase-shift characterization of in-liquid quartz crystal microbalance applications," *Rev. Sci. Instrum.*, vol. 82, no. 6, p. 64702, Jun. 2011.
- [62] A. B. Dahlin, P. Jönsson, M. P. Jonsson, E. Schmid, Y. Zhou, and F. Höök, "Synchronized Quartz Crystal Microbalance and Nanoplasmonic Sensing of Biomolecular Recognition Reactions," *ACS Nano*, vol. 2, no. 10, pp. 2174–2182, Oct. 2008.
- [63] J. Friend and L. Y. Yeo, "Microscale acoustofluidics: Microfluidics driven via

- acoustics and ultrasonics," *Rev. Mod. Phys.*, vol. 83, no. 2, pp. 647–704, Jun. 2011.
- [64] Lord Rayleigh, "On the Circulation of Air Observed in Kundt's Tubes, and on Some Allied Acoustical Problems," *Philos. Trans. R. Soc. London*, vol. 175, no. January, pp. 1–21, Jan. 1884.
- [65] P. Transducers, *Piezoelectric Transducers and Applications*. Berlin, Heidelberg: Springer Berlin Heidelberg, 2008.
- [66] N. Tesla, "Electrical Condenser," US464667A, 1891.
- [67] J. Nam, H. Lim, and S. Shin, "Manipulation of microparticles using surface acoustic wave in microfluidic systems: a brief review," *Korea-Australia Rheol. J.*, vol. 23, no. 4, pp. 255–267, Dec. 2011.
- [68] A. Pohl, "A review of wireless SAW sensors," *IEEE Trans. Ultrason. Ferroelectr. Freq. Control*, vol. 47, no. 2, pp. 317–332, Mar. 2000.
- [69] R. Weigel, D. P. Morgan, J. M. Owens, A. Ballato, K. M. Lakin, K. Hashimoto, and C. C. W. Ruppel, "Microwave acoustic materials, devices, and applications," *IEEE Trans. Microw. Theory Tech.*, vol. 50, no. 3, pp. 738–749, Mar. 2002.
- [70] K. Sritharan, C. J. Strobl, M. F. Schneider, A. Wixforth, and Z. Guttenberg, "Acoustic mixing at low Reynold's numbers," *Appl. Phys. Lett.*, vol. 88, no. 5, p. 54102, Jan. 2006.
- [71] W.-K. Tseng, J.-L. Lin, W.-C. Sung, S.-H. Chen, and G.-B. Lee, "Active micro-mixers using surface acoustic waves on Y-cut 128° LiNbO<sub>3</sub>," *J. Micromechanics Microengineering*, vol. 16, no. 3, pp. 539–548, Mar. 2006.
- [72] M. Cecchini, S. Girardo, D. Pisignano, R. Cingolani, and F. Beltram, "Acoustic-counterflow microfluidics by surface acoustic waves," *Appl. Phys. Lett.*, vol. 92, no. 10, p. 104103, Mar. 2008.
- [73] Z. Guttenberg, A. Rathgeber, S. Keller, J. O. Rädler, A. Wixforth, M. Kostur, M. Schindler, and P. Talkner, "Flow profiling of a surface-acoustic-wave nanopump," *Phys. Rev. E*, vol. 70, no. 5, p. 56311, Nov. 2004.
- [74] H. Li, J. R. Friend, and L. Y. Yeo, "Microfluidic Colloidal Island Formation and Erasure Induced by Surface Acoustic Wave Radiation," *Phys. Rev. Lett.*, vol. 101, no. 8, p. 84502, Aug. 2008.
- [75] H. Li, J. R. Friend, and L. Y. Yeo, "Surface acoustic wave concentration of particle and bioparticle suspensions," *Biomed. Microdevices*, vol. 9, no. 5, pp. 647–656, Aug. 2007.
- [76] R. V. Raghavan, J. R. Friend, and L. Y. Yeo, "Particle concentration via acoustically driven microcentrifugation: microPIV flow visualization and numerical modelling studies," *Microfluid. Nanofluidics*, vol. 8, no. 1, pp. 73–84, Jan. 2010.
- [77] T. Smorodin, U. Beierlein, J. Ebbecke, and A. Wixforth, "Surface-Acoustic-Wave-Enhanced Alignment of Thiolated Carbon Nanotubes on Gold Electrodes," *Small*, vol. 1, no. 12, pp. 1188–1190, Dec. 2005.
- [78] C. J. Strobl, C. Schäflein, U. Beierlein, J. Ebbecke, and A. Wixforth, "Carbon

- nanotube alignment by surface acoustic waves," *Appl. Phys. Lett.*, vol. 85, no. 8, pp. 1427–1429, Aug. 2004.
- [79] T. Franke, S. Braunmüller, L. Schmid, A. Wixforth, and D. A. Weitz, "Surface acoustic wave actuated cell sorting (SAWACS)," *Lab Chip*, vol. 10, no. 6, p. 789, 2010.
- [80] T. Franke, A. R. Abate, D. A. Weitz, and A. Wixforth, "Surface acoustic wave (SAW) directed droplet flow in microfluidics for PDMS devices," *Lab Chip*, vol. 9, no. 18, p. 2625, 2009.
- [81] J. K. Luo, Y. Q. Fu, and W. I. Milne, "Acoustic Wave Based Microfluidics and Lab-on-a-Chip," in *Modeling and Measurement Methods for Acoustic Waves and for Acoustic Microdevices*, vol. 6, K. Pesek, Ed. InTech, 2013, pp. 515–556.
- [82] E. Galopin, M. Beaugeois, B. Pinchemel, J.-C. Camart, M. Bouazaoui, and V. Thomy, "SPR biosensing coupled to a digital microfluidic microstreaming system," *Biosens. Bioelectron.*, vol. 23, no. 5, pp. 746–750, Dec. 2007.
- [83] S. W. Schneider, S. Nuschele, A. Wixforth, C. Gorzelanny, A. Alexander-Katz, R. R. Netz, and M. F. Schneider, "Shear-induced unfolding triggers adhesion of von Willebrand factor fibers," *Proc. Natl. Acad. Sci.*, vol. 104, no. 19, pp. 7899–7903, May 2007.
- [84] G. D. Skotis, J. Roberts, D. R. S. Cumming, M. O. Riehle, and A. L. Bernassau, "Acoustic tweezing for patterning and discriminating particles," in *2015 11th Conference on Ph.D. Research in Microelectronics and Electronics (PRIME)*, 2015, pp. 29–32.
- [85] J. Shi, X. Mao, D. Ahmed, A. Colletti, and T. J. Huang, "Focusing microparticles in a microfluidic channel with standing surface acoustic waves (SSAW)," *Lab Chip*, vol. 8, no. 2, pp. 221–223, 2008.
- [86] J. Shi, H. Huang, Z. Stratton, Y. Huang, and T. J. Huang, "Continuous particle separation in a microfluidic channel via standing surface acoustic waves (SSAW)," *Lab Chip*, vol. 9, no. 23, p. 3354, 2009.
- [87] T. M. A. Gronewold, "Surface acoustic wave sensors in the bioanalytical field: Recent trends and challenges," *Anal. Chim. Acta*, vol. 603, no. 2, pp. 119–128, Nov. 2007.
- [88] E. Berkenpas, P. Millard, and M. Pereira da Cunha, "Detection of Escherichia coli O157:H7 with langasite pure shear horizontal surface acoustic wave sensors," *Biosens. Bioelectron.*, vol. 21, no. 12, pp. 2255–2262, Jun. 2006.
- [89] K. A. Marx, "Quartz Crystal Microbalance: A Useful Tool for Studying Thin Polymer Films and Complex Biomolecular Systems at the Solution–Surface Interface," *Biomacromolecules*, vol. 4, no. 5, pp. 1099–1120, Sep. 2003.
- [90] H. Wohltjen, "Mechanism of operation and design considerations for surface acoustic wave device vapour sensors," *Sensors and Actuators*, vol. 5, no. 4, pp. 307–325, Jul. 1984.
- [91] C. Caliendo, E. Verona, and V. I. Anisimkin, "Surface acoustic wave humidity sensors: a comparison between different types of sensitive membrane," *Smart Mater.*

*Struct.*, vol. 6, no. 6, pp. 707–715, Dec. 1997.

- [92] D. Nardi, E. Zagato, G. Ferrini, C. Giannetti, and F. Banfi, "Design of a surface acoustic wave mass sensor in the 100 GHz range," *Appl. Phys. Lett.*, vol. 100, no. 25, p. 253106, Jun. 2012.
- [93] Z. Yu and S. Boseck, "Scanning acoustic microscopy and its applications to material characterization," *Rev. Mod. Phys.*, vol. 67, no. 4, pp. 863–891, Oct. 1995.
- [94] S. P. Mohanty and E. Kougiyanos, "Biosensors: a tutorial review," *IEEE Potentials*, vol. 25, no. 2, pp. 35–40, Mar. 2006.
- [95] J. C. Andle and J. F. Vetelino, "Acoustic wave biosensors," *Sensors Actuators A Phys.*, vol. 44, no. 3, pp. 167–176, Sep. 1994.
- [96] N. C. Fawcett, R. D. Craven, P. Zhang, and J. a Evans, "QCM Response to Solvated, Tethered Macromolecules," *Anal. Chem.*, vol. 70, no. 14, pp. 2876–2880, Jul. 1998.
- [97] M. a Cooper, F. N. Dultsev, T. Minson, V. P. Ostanin, C. Abell, and D. Klenerman, "No Title," *Nat. Biotechnol.*, vol. 19, no. 9, pp. 833–837, Sep. 2001.
- [98] M. A. Cooper and V. T. Singleton, "A survey of the 2001 to 2005 quartz crystal microbalance biosensor literature: applications of acoustic physics to the analysis of biomolecular interactions," *J. Mol. Recognit.*, vol. 20, no. 3, pp. 154–184, May 2007.
- [99] R. D. Vaughan, C. K. O'Sullivan, and G. G. Guilbault, "Development of a quartz crystal microbalance (QCM) immunosensor for the detection of *Listeria monocytogenes*," *Enzyme Microb. Technol.*, vol. 29, no. 10, pp. 635–638, 2001.
- [100] Y. J. Yuan, Q. Chen, and J. Li, "QCM-based immunosensor for determining immunoglobulin G," *RSC Adv.*, vol. 6, no. 46, pp. 40336–40342, 2016.
- [101] C. Larsson, M. Rodahl, and F. Höök, "Characterization of DNA Immobilization and Subsequent Hybridization on a 2D Arrangement of Streptavidin on a Biotin-Modified Lipid Bilayer Supported on SiO<sub>2</sub>," *Anal. Chem.*, vol. 75, no. 19, pp. 5080–5087, Oct. 2003.
- [102] G. Wang, A. H. Dewilde, J. Zhang, A. Pal, M. Vashist, D. Bello, K. A. Marx, S. J. Braunhut, and J. M. Therrien, "A living cell quartz crystal microbalance biosensor for continuous monitoring of cytotoxic responses of macrophages to single-walled carbon nanotubes," *Part. Fibre Toxicol.*, vol. 8, no. 1, p. 4, 2011.
- [103] C. A. Flory and R. L. Baer, "Surface Transverse Wave Mode Analysis and Coupling to Interdigital Transducers," in *IEEE 1987 Ultrasonics Symposium*, 1987, vol. 144, no. 5, pp. 313–318.
- [104] D. F. Thompson and B. a. Auld, "Surface Transverse Wave Propagation Under Metal Strip Gratings," in *IEEE 1986 Ultrasonics Symposium*, 1986, pp. 261–266.
- [105] R. L. Baer, C. a. Flory, M. Tom-Moy, and D. Solomon, "STW chemical sensors," in *IEEE 1992 Ultrasonics Symposium Proceedings*, 1992, pp. 293–298.
- [106] Y. Inoue, Y. Kato, and K. Sato, "Surface acoustic wave method for in situ determination of the amounts of enzyme–substrate complex formed on immobilized glucose oxidase during catalytic reaction," *J. Chem. Soc., Faraday Trans.*,

vol. 88, no. 3, pp. 449–454, 1992.

- [107] J. Kondoh, Y. Matsui, and S. Shiokawa, “New Biosensor Using Shear Horizontal Surface Acoustic Wave Device,” *Jpn. J. Appl. Phys.*, vol. 32, no. Part 1, No. 5B, pp. 2376–2379, May 1993.
- [108] E. Gizeli, N. J. Goddard, C. R. Lowe, and A. C. Stevenson, “A Love plate biosensor utilising a polymer layer,” *Sensors Actuators B Chem.*, vol. 6, no. 1–3, pp. 131–137, Jan. 1992.
- [109] E. Gizeli, A. C. Stevenson, N. J. Goddard, and C. R. Lowe, “A novel Love-plate acoustic sensor utilizing polymer overlayers,” *IEEE Trans. Ultrason. Ferroelectr. Freq. Control*, vol. 39, no. 5, pp. 657–659, Sep. 1992.
- [110] A. C. Stevenson, E. Gizeli, N. J. Goddard, and C. R. Lowe, “Acoustic Love plate sensors: a theoretical model for the optimization of the surface mass sensitivity,” *Sensors Actuators B Chem.*, vol. 14, no. 1–3, pp. 635–637, Jun. 1993.
- [111] M. Rapp, T. Wessa, and H. J. Ache, “Modification of commercially available low-loss SAW devices towards an immunosensor for in-situ measurements in water,” in *1995 IEEE Ultrasonics Symposium. Proceedings. An International Symposium, 1995*, vol. 1, pp. 433–436.
- [112] T. Wessa, N. Barié, M. Rapp, and H. . Ache, “Polyimide, a new shielding layer for sensor applications,” *Sensors Actuators B Chem.*, vol. 53, no. 1–2, pp. 63–68, Nov. 1998.
- [113] N. Barié, M. Rapp, H. Sigrist, and H. J. Ache, “Covalent photolinker-mediated immobilization of an intermediate dextran layer to polymer-coated surfaces for biosensing applications,” *Biosens. Bioelectron.*, vol. 13, no. 7–8, pp. 855–860, Oct. 1998.
- [114] N. Barié, H. Sigrist, and M. Rapp, “Development of immunosensors based on commercially available surface acoustic wave (SAW) devices,” *Analisis*, vol. 27, no. 7, pp. 622–629, Sep. 1999.
- [115] T. Wessa, M. Rapp, and H. J. Ache, “New immobilization method for SAW-biosensors: covalent attachment of antibodies via CNBr,” *Biosens. Bioelectron.*, vol. 14, no. 1, pp. 93–98, Jan. 1999.
- [116] T. Wessa, M. Rapp, and H. Sigrist, “Immunosensing of photoimmobilized proteins on surface acoustic wave sensors,” *Colloids Surfaces B Biointerfaces*, vol. 15, no. 2, pp. 139–146, Sep. 1999.
- [117] N. Barié and M. Rapp, “Covalent bound sensing layers on surface acoustic wave (SAW) biosensors,” *Biosens. Bioelectron.*, vol. 16, no. 9–12, pp. 979–987, Dec. 2001.
- [118] G. L. Harding, J. Du, P. R. Dencher, D. Barnett, and E. Howe, “Love wave acoustic immunosensor operating in liquid,” *Sensors Actuators A Phys.*, vol. 61, no. 1–3, pp. 279–286, Jun. 1997.
- [119] H.-L. Cai, Y. Yang, X. Chen, M. A. Mohammad, T.-X. Ye, C.-R. Guo, L.-T. Yi, C.-J. Zhou, J. Liu, and T.-L. Ren, “A third-order mode high frequency biosensor with atomic resolution,” *Biosens. Bioelectron.*, vol. 71, pp. 261–268, Sep. 2015.
- [120] F. Zhang, S. Li, K. Cao, P. Wang, Y. Su, X. Zhu, and Y. Wan, “A Microfluidic Love-Wave Biosensing Device for PSA Detection Based on an Aptamer Beacon Probe,”

*Sensors*, vol. 15, no. 6, pp. 13839–13850, Jun. 2015.

- [121] H. C. Hao and D. J. Yao, “Highly sensitive and rapid detection of shigella flexneri in liquid sample by an immunomagnetic assay with shear horizontal surface acoustic wave sensors,” in *2013 Transducers & Eurosensors XXVII: The 17th International Conference on Solid-State Sensors, Actuators and Microsystems (TRANSDUCERS & EUROSENSORS XXVII)*, 2013, no. June, pp. 2114–2117.
- [122] D. Matatagui, J. Fontecha, M. Fernández, I. Gràcia, C. Cané, J. Santos, and M. Horrillo, “Love-Wave Sensors Combined with Microfluidics for Fast Detection of Biological Warfare Agents,” *Sensors*, vol. 14, no. 7, pp. 12658–12669, Jul. 2014.
- [123] B. Liu, X. Chen, H. Cai, M. Mohammad Ali, X. Tian, L. Tao, Y. Yang, and T. Ren, “Surface acoustic wave devices for sensor applications,” *J. Semicond.*, vol. 37, no. 2, p. 21001, Feb. 2016.
- [124] S. Scarano, M. Mascini, A. P. F. Turner, and M. Minunni, “Surface plasmon resonance imaging for affinity-based biosensors,” *Biosens. Bioelectron.*, vol. 25, no. 5, pp. 957–966, Jan. 2010.
- [125] P. Singh, “SPR Biosensors: Historical Perspectives and Current Challenges,” *Sensors Actuators B Chem.*, vol. 229, pp. 110–130, Jun. 2016.
- [126] G. Zeder-Lutz, E. Zuber, J. Witz, and M. H. V. Van Regenmortel, “Thermodynamic Analysis of Antigen–Antibody Binding Using Biosensor Measurements at Different Temperatures,” *Anal. Biochem.*, vol. 246, no. 1, pp. 123–132, Mar. 1997.
- [127] P. Pattnaik, “Surface Plasmon Resonance: Applications in Understanding Receptor–Ligand Interaction,” *Appl. Biochem. Biotechnol.*, vol. 126, no. 2, pp. 079–092, 2005.
- [128] G. J. Wegner, A. W. Wark, H. J. Lee, E. Codner, T. Saeki, S. Fang, and R. M. Corn, “Real-Time Surface Plasmon Resonance Imaging Measurements for the Multiplexed Determination of Protein Adsorption/Desorption Kinetics and Surface Enzymatic Reactions on Peptide Microarrays,” *Anal. Chem.*, vol. 76, no. 19, pp. 5677–5684, Oct. 2004.
- [129] P. Sibille and A. D. Strosberg, “A FIV epitope defined by a phage peptide library screened with a monoclonal anti-FIV antibody,” *Immunol. Lett.*, vol. 59, no. 3, pp. 133–137, Dec. 1997.
- [130] A. J. Haes, L. Chang, W. L. Klein, and R. P. Van Duyne, “Detection of a Biomarker for Alzheimer’s Disease from Synthetic and Clinical Samples Using a Nanoscale Optical Biosensor,” *J. Am. Chem. Soc.*, vol. 127, no. 7, pp. 2264–2271, Feb. 2005.
- [131] A. P. Alivisatos, K. P. Johnsson, X. Peng, T. E. Wilson, C. J. Loweth, M. P. Bruchez, and P. G. Schultz, “Organization of ‘nanocrystal molecules’ using DNA,” *Nature*, vol. 382, no. 6592, pp. 609–611, Aug. 1996.
- [132] N. T. K. Thanh and Z. Rosenzweig, “Development of an Aggregation-Based Immunoassay for Anti-Protein A Using Gold Nanoparticles,” *Anal. Chem.*, vol. 74, no. 7, pp. 1624–1628, Apr. 2002.
- [133] S.-F. Cheng and L.-K. Chau, “Colloidal Gold-Modified Optical Fiber for Chemical

- and Biochemical Sensing," *Anal. Chem.*, vol. 75, no. 1, pp. 16–21, Jan. 2003.
- [134] K. Mitsui, Y. Handa, and K. Kajikawa, "Optical fiber affinity biosensor based on localized surface plasmon resonance," *Appl. Phys. Lett.*, vol. 85, no. 18, pp. 4231–4233, Nov. 2004.
- [135] J. Homola, "Present and future of surface plasmon resonance biosensors," *Anal. Bioanal. Chem.*, vol. 377, no. 3, pp. 528–539, Oct. 2003.
- [136] Biocompare, "Surface Plasmon Resonance Systems (SPR System)." [Online]. Available: <http://www.biocompare.com/Lab-Equipment/23222-Surface-Plasmon-Resonance-Systems-SPR-System/>. [Accessed: 17-Sep-2016].
- [137] A. Arnau, "A Review of Interface Electronic Systems for AT-cut Quartz Crystal Microbalance Applications in Liquids," *Sensors*, vol. 8, no. 1, pp. 370–411, Jan. 2008.
- [138] S. Roh, T. Chung, and B. Lee, "Overview of the Characteristics of Micro- and Nano-Structured Surface Plasmon Resonance Sensors," *Sensors*, vol. 11, no. 2, pp. 1565–1588, Jan. 2011.
- [139] M. Edvardsson, S. Svedhem, G. Wang, R. Richter, M. Rodahl, and B. Kasemo, "QCM-D and Reflectometry Instrument: Applications to Supported Lipid Structures and Their Biomolecular Interactions," *Anal. Chem.*, vol. 81, no. 1, pp. 349–361, Jan. 2009.
- [140] S. J. Martin, V. E. Granstaff, and G. C. Frye, "Characterization of a quartz crystal microbalance with simultaneous mass and liquid loading," *Anal. Chem.*, vol. 63, no. 20, pp. 2272–2281, Oct. 1991.
- [141] T. Ozeki, M. Morita, H. Yoshimine, H. Furusawa, and Y. Okahata, "Hydration and Energy Dissipation Measurements of Biomolecules on a Piezoelectric Quartz Oscillator by Admittance Analyses," *Anal. Chem.*, vol. 79, no. 1, pp. 79–88, Jan. 2007.
- [142] A. Tsortos, G. Papadakis, K. Mitsakakis, K. A. Melzak, and E. Gizeli, "Quantitative Determination of Size and Shape of Surface-Bound DNA Using an Acoustic Wave Sensor," *Biophys. J.*, vol. 94, no. 7, pp. 2706–2715, Apr. 2008.
- [143] E. Reimhult, C. Larsson, B. Kasemo, and F. Höök, "Simultaneous Surface Plasmon Resonance and Quartz Crystal Microbalance with Dissipation Monitoring Measurements of Biomolecular Adsorption Events Involving Structural Transformations and Variations in Coupled Water," *Anal. Chem.*, vol. 76, no. 24, pp. 7211–7220, Dec. 2004.
- [144] J. Rishpon, A. Redondo, C. Derouin, and S. Gottesfeld, "Simultaneous ellipsometric and microgravimetric measurements during the electrochemical growth of polyaniline," *J. Electroanal. Chem. Interfacial Electrochem.*, vol. 294, no. 1–2, pp. 73–85, Nov. 1990.
- [145] C. Kößlinger, E. Uttenthaler, S. Drost, F. Aberl, H. Wolf, G. Brink, A. Stanglmaier, and E. Sackmann, "Comparison of the QCM and the SPR method for surface studies and immunological applications," *Sensors Actuators B Chem.*, vol. 24, no. 1–3, pp. 107–112, Mar. 1995.
- [146] B. S. Lee, Y. S. Chi, K.-B. Lee, Y.-G. Kim, and I. S. Choi, "Functionalization of

- Poly(oligo(ethylene glycol) methacrylate) Films on Gold and Si/SiO<sub>2</sub> for Immobilization of Proteins and Cells: SPR and QCM Studies," *Biomacromolecules*, vol. 8, no. 12, pp. 3922–3929, Dec. 2007.
- [147] C. Zhou, J. Friedt, A. Angelova, K. Choi, W. Laureyn, F. Frederix, L. A. Francis, A. Campitelli, Y. Engelborghs, and G. Borghs, "Human Immunoglobulin Adsorption Investigated by Means of Quartz Crystal Microbalance Dissipation, Atomic Force Microscopy, Surface Acoustic Wave, and Surface Plasmon Resonance Techniques," *Langmuir*, vol. 20, no. 14, pp. 5870–5878, Jul. 2004.
- [148] A. Laschitsch, B. Menges, and D. Johannsmann, "Simultaneous determination of optical and acoustic thicknesses of protein layers using surface plasmon resonance spectroscopy and quartz crystal microweighing," *Appl. Phys. Lett.*, vol. 77, no. 14, pp. 2252–2254, Oct. 2000.
- [149] L. E. Bailey, D. Kambhampati, K. K. Kanazawa, W. Knoll, and C. W. Frank, "Using Surface Plasmon Resonance and the Quartz Crystal Microbalance to Monitor in Situ the Interfacial Behavior of Thin Organic Films," *Langmuir*, vol. 18, no. 2, pp. 479–489, Jan. 2002.
- [150] M. A. Plunkett, Z. Wang, M. W. Rutland, and D. Johannsmann, "Adsorption of pNIPAM Layers on Hydrophobic Gold Surfaces, Measured in Situ by QCM and SPR," *Langmuir*, vol. 19, no. 17, pp. 6837–6844, Aug. 2003.
- [151] a Bund, A. Baba, S. Berg, D. Johannsmann, J. Lübben, Z. Wang, and W. Knoll, "Combining Surface Plasmon Resonance and Quartz Crystal Microbalance for the in Situ Investigation of the Electropolymerization and Doping/Dedoping of Poly(pyrrole)," *J. Phys. Chem. B*, vol. 107, no. 28, pp. 6743–6747, Jul. 2003.
- [152] J. Kim, S. Kim, T. Ohashi, H. Muramatsu, S.-M. Chang, and W.-S. Kim, "Construction of simultaneous SPR and QCM sensing platform," *Bioprocess Biosyst. Eng.*, vol. 33, no. 1, pp. 39–45, Jan. 2010.
- [153] E. Reimhult, M. Zäch, F. Höök, and B. Kasemo, "A Multitechnique Study of Liposome Adsorption on Au and Lipid Bilayer Formation on SiO<sub>2</sub>," *Langmuir*, vol. 22, no. 7, pp. 3313–3319, Mar. 2006.
- [154] G. Stengel, F. Höök, and W. Knoll, "Viscoelastic Modeling of Template-Directed DNA Synthesis," *Anal. Chem.*, vol. 77, no. 11, pp. 3709–3714, Jun. 2005.
- [155] K. Shinbo, H. Ishikawa, A. Baba, Y. Ohdaira, K. Kato, and F. Kaneko, "Fabrication of a Quartz-Crystal-Microbalance/Surface-Plasmon-Resonance Hybrid Sensor and Its Use for Detection of Polymer Thin-Film Deposition and Evaluation of Moisture Sorption Phenomena," *Appl. Phys. Express*, vol. 5, no. 3, p. 36603, Mar. 2012.
- [156] J.-M. Friedt, L. Francis, G. Reekmans, R. De Palma, A. Campitelli, and U. B. Sleytr, "Simultaneous surface acoustic wave and surface plasmon resonance measurements: Electrodeposition and biological interactions monitoring," *J. Appl. Phys.*, vol. 95, no. 4, pp. 1677–1680, Feb. 2004.
- [157] M. P. Jonsson, P. Jönsson, and F. Höök, "Simultaneous Nanoplasmonic and Quartz Crystal Microbalance Sensing: Analysis of Biomolecular Conformational Changes and Quantification of the Bound Molecular Mass," *Anal. Chem.*, vol. 80, no. 21, pp.

7988–7995, Nov. 2008.

- [158] E. M. Larsson, M. E. M. Edvardsson, C. Langhammer, I. Zorić, and B. Kasemo, “A combined nanoplasmonic and electrodeless quartz crystal microbalance setup,” *Rev. Sci. Instrum.*, vol. 80, no. 12, p. 125105, Dec. 2009.
- [159] A. R. Ferhan, J. A. Jackman, and N. Cho, “Integration of Quartz Crystal Microbalance-Dissipation and Reflection-Mode Localized Surface Plasmon Resonance Sensors for Biomacromolecular Interaction Analysis,” *Anal. Chem.*, vol. 88, no. 24, pp. 12524–12531, Dec. 2016.
- [160] Kane Yee, “Numerical solution of initial boundary value problems involving maxwell’s equations in isotropic media,” *IEEE Trans. Antennas Propag.*, vol. 14, no. 3, pp. 302–307, May 1966.
- [161] M. Hussein and A. Sebak, “Application of the finite-difference time-domain method to the analysis of mobile antennas,” *IEEE Trans. Veh. Technol.*, vol. 45, no. 3, pp. 417–426, 1996.
- [162] Lumerical, “Lumerical Solutions, Inc.,” [Htpps://Www.Lumerical.Com](https://www.lumerical.com), 2016. [Online]. Available: <https://www.lumerical.com>. [Accessed: 12-Aug-2017].
- [163] JWNC, “James Watt Nanofabrication Centre,” <http://jwnc.eng.gla.ac.uk/>, 2011. [Online]. Available: <http://jwnc.eng.gla.ac.uk/>. [Accessed: 12-Aug-2017].
- [164] JWNC, “Sputter Coater for SEM Sample Prep,” 2017. [Online]. Available: [http://jwnc.eng.gla.ac.uk/index.php?module=equipment&cmd=view&equipment\\_id=71](http://jwnc.eng.gla.ac.uk/index.php?module=equipment&cmd=view&equipment_id=71). [Accessed: 21-Aug-2017].
- [165] S. MicroTec, “MA/BA6 Mask and Bond Aligner,” 2017. [Online]. Available: <https://www.suss.com/en/products-solutions/mask-aligner/ma-ba-6>. [Accessed: 13-Aug-2017].
- [166] Compugraphics, “Compugraphics,” 2015. [Online]. Available: <http://www.compugraphics-photomasks.com/>. [Accessed: 13-Aug-2017].
- [167] M. Stepanova and S. Dew, *Nanofabrication*. Vienna: Springer Vienna, 2012.
- [168] Y.-C. Chang, H.-C. Chung, S.-C. Lu, and T.-F. Guo, “A large-scale sub-100 nm Au nanodisk array fabricated using nanospherical-lens lithography: a low-cost localized surface plasmon resonance sensor,” *Nanotechnology*, vol. 24, no. 9, p. 95302, Mar. 2013.
- [169] A. L. Kipling and M. Thompson, “Network analysis method applied to liquid-phase acoustic wave sensors,” *Anal. Chem.*, vol. 62, no. 14, pp. 1514–1519, Jul. 1990.
- [170] S. Bruckenstein and M. Shay, “Experimental aspects of use of the quartz crystal microbalance in solution,” *Electrochim. Acta*, vol. 30, no. 10, pp. 1295–1300, Oct. 1985.
- [171] P. B. Johnson and R. W. Christy, “Optical Constants of the Noble Metals,” *Phys. Rev. B*, vol. 6, no. 12, pp. 4370–4379, Dec. 1972.
- [172] E. Palik, *Handbook of Optical Constants of Solids*, 1st ed. Academic Press, 1985.
- [173] M.-C. Estevez, M. A. Otte, B. Sepulveda, and L. M. Lechuga, “Trends and challenges of refractometric nanoplasmonic biosensors: A review,” *Anal. Chim. Acta*, vol. 806,

pp. 55–73, Jan. 2014.

- [174] A. Shakoor, B. C. Cheah, D. Hao, M. Al-Rawhani, B. Nagy, J. Grant, C. Dale, N. Keegan, C. McNeil, and D. R. S. Cumming, “Plasmonic Sensor Monolithically Integrated with a CMOS Photodiode,” *ACS Photonics*, vol. 3, no. 10, pp. 1926–1933, Oct. 2016.
- [175] C. L. Haynes, A. D. McFarland, L. Zhao, R. P. Van Duyne, G. C. Schatz, L. Gunnarsson, J. Prikulis, B. Kasemo, and M. Käll, “Nanoparticle Optics: The Importance of Radiative Dipole Coupling in Two-Dimensional Nanoparticle Arrays †,” *J. Phys. Chem. B*, vol. 107, no. 30, pp. 7337–7342, Jul. 2003.
- [176] B. Johansen, C. Uhrenfeldt, A. N. Larsen, T. G. Pedersen, H. U. Ulriksen, P. K. Kristensen, J. Jung, T. Søndergaard, and K. Pedersen, “Optical transmission through two-dimensional arrays of  $\beta$ -Sn nanoparticles,” *Phys. Rev. B*, vol. 84, no. 11, p. 113405, Sep. 2011.
- [177] K. Munechika, J. M. Smith, Y. Chen, and D. S. Ginger, “Plasmon Line Widths of Single Silver Nanoprisms as a Function of Particle Size and Plasmon Peak Position,” *J. Phys. Chem. C*, vol. 111, no. 51, pp. 18906–18911, Dec. 2007.
- [178] H. Chen, X. Kou, Z. Yang, W. Ni, and J. Wang, “Shape- and Size-Dependent Refractive Index Sensitivity of Gold Nanoparticles,” *Langmuir*, vol. 24, no. 10, pp. 5233–5237, May 2008.
- [179] L. F. Hoyt, “New Table of the Refractive Index of Pure Glycerol at 20°C,” *Ind. Eng. Chem.*, vol. 26, no. 3, pp. 329–332, Mar. 1934.
- [180] S. S. Aćimović, M. A. Ortega, V. Sanz, J. Berthelot, J. L. Garcia-Cordero, J. Renger, S. J. Maerkl, M. P. Kreuzer, and R. Quidant, “LSPR Chip for Parallel, Rapid, and Sensitive Detection of Cancer Markers in Serum,” *Nano Lett.*, vol. 14, no. 5, pp. 2636–2641, May 2014.
- [181] A. G. Brolo, “Plasmonics for future biosensors,” *Nat. Photonics*, vol. 6, no. 11, pp. 709–713, Nov. 2012.
- [182] A. Renaudin, V. Chabot, E. Grondin, V. Aimez, and P. G. Charette, “Integrated active mixing and biosensing using surface acoustic waves (SAW) and surface plasmon resonance (SPR) on a common substrate,” *Lab Chip*, vol. 10, no. 1, pp. 111–115, 2010.
- [183] J. N. Anker, W. P. Hall, O. Lyandres, N. C. Shah, J. Zhao, and R. P. Van Duyne, “Biosensing with plasmonic nanosensors,” *Nat. Mater.*, vol. 7, no. 6, pp. 442–453, Jun. 2008.
- [184] M. Nirschl, F. Reuter, and J. Vörös, “Review of Transducer Principles for Label-Free Biomolecular Interaction Analysis,” *Biosensors*, vol. 1, no. 3, pp. 70–92, Jul. 2011.
- [185] J. Vörös, “The Density and Refractive Index of Adsorbing Protein Layers,” *Biophys. J.*, vol. 87, no. 1, pp. 553–561, Jul. 2004.
- [186] K. Mitsakakis, A. Tsortos, and E. Gizeli, “Quantitative determination of protein molecular weight with an acoustic sensor; significance of specific versus non-specific binding,” *Analyst*, vol. 139, no. 16, pp. 3918–3925, Jun. 2014.

- [187] F. Bender, P. Roach, A. Tsortos, G. Papadakis, M. I. Newton, G. McHale, and E. Gizeli, "Development of a combined surface plasmon resonance/surface acoustic wave device for the characterization of biomolecules," *Meas. Sci. Technol.*, vol. 20, no. 12, p. 124011, Dec. 2009.
- [188] D. Hao, M. G. Kenney, and D. R. S. Cumming, "Plasmonic gold nanodiscs using piezoelectric substrate birefringence for liquid sensing," *Appl. Phys. Lett.*, vol. 108, no. 25, p. 251601, Jun. 2016.
- [189] S. Sanna and W. G. Schmidt, "Lithium niobate X-cut, Y-cut, and Z-cut surfaces from ab initio theory," *Phys. Rev. B*, vol. 81, no. 21, p. 214116, Jun. 2010.
- [190] R. S. Weis and T. K. Gaylord, "Lithium niobate: Summary of physical properties and crystal structure," *Appl. Phys. A Solids Surfaces*, vol. 37, no. 4, pp. 191–203, Aug. 1985.
- [191] Lumerical, "Unpolarized beam." [Online]. Available: [https://kb.lumerical.com/en/ref\\_sim\\_obj\\_fDTD\\_coherence\\_unpolarized\\_beam.html](https://kb.lumerical.com/en/ref_sim_obj_fDTD_coherence_unpolarized_beam.html). [Accessed: 06-Sep-2017].
- [192] S.-W. Lee, K.-S. Lee, J. Ahn, J.-J. Lee, M.-G. Kim, and Y.-B. Shin, "Highly Sensitive Biosensing Using Arrays of Plasmonic Au Nanodisks Realized by Nanoimprint Lithography," *ACS Nano*, vol. 5, no. 2, pp. 897–904, Feb. 2011.
- [193] K. Lodewijks, W. Van Roy, G. Borghs, L. Lagae, and P. Van Dorpe, "Boosting the Figure-Of-Merit of LSPR-Based Refractive Index Sensing by Phase-Sensitive Measurements," *Nano Lett.*, vol. 12, no. 3, pp. 1655–1659, Mar. 2012.
- [194] M. M. Miller and A. A. Lazarides, "Sensitivity of Metal Nanoparticle Surface Plasmon Resonance to the Dielectric Environment," *J. Phys. Chem. B*, vol. 109, no. 46, pp. 21556–21565, Nov. 2005.
- [195] J. Malmström, H. Agheli, P. Kingshott, and D. S. Sutherland, "Viscoelastic Modeling of Highly Hydrated Laminin Layers at Homogeneous and Nanostructured Surfaces: Quantification of Protein Layer Properties Using QCM-D and SPR," *Langmuir*, vol. 23, no. 19, pp. 9760–9768, Sep. 2007.
- [196] Y. J. Yuan and Kui Han, "Development of a real-time QCM bond-rupture system for POCT applications," in *2015 IEEE SENSORS*, 2015, vol. 16, no. 24, pp. 1–4.
- [197] J. B. Segur and H. E. Oberstar, "Viscosity of Glycerol and Its Aqueous Solutions," *Ind. Eng. Chem.*, vol. 43, no. 9, pp. 2117–2120, Sep. 1951.
- [198] J. Rabe, S. Buttgenbach, J. Schroder, and P. Hauptmann, "Monolithic miniaturized quartz microbalance array and its application to chemical sensor systems for liquids," *IEEE Sens. J.*, vol. 3, no. 4, pp. 361–368, Aug. 2003.
- [199] M. J. Oliver, J. Hernando-García, P. Pobedinskas, K. Haenen, A. Ríos, and J. L. Sánchez-Rojas, "Reusable chromium-coated quartz crystal microbalance for immunosensing," *Colloids Surfaces B Biointerfaces*, vol. 88, no. 1, pp. 191–195, Nov. 2011.
- [200] J. He, Y. Lu, J. Fang, and H. Ma, "The change in thickness of the solidified liquid layer rather than the immobilized mass determines the frequency response of a

- quartz crystal microbalance," *Sci. China Chem.*, vol. 55, no. 1, pp. 175–181, Jan. 2012.
- [201] F. Fernandez, O. Garcia-Lopez, E. Tellechea, A. C. Asensio, and I. Cornago, "LSPR Cuvette for Real-Time Biosensing by Using a Common Spectrophotometer," *IEEE Sens. J.*, vol. 16, no. 11, pp. 4158–4165, Jun. 2016.
- [202] Y. Liu, Q. Liu, S. Chen, F. Cheng, H. Wang, and W. Peng, "Surface Plasmon Resonance Biosensor Based on Smart Phone Platforms," *Sci. Rep.*, vol. 5, no. 1, p. 12864, Oct. 2015.
- [203] H. Takei, N. Bessho, A. Ishii, T. Okamoto, A. Beyer, H. Vieker, and A. Götzhäuser, "Enhanced Infrared LSPR Sensitivity of Cap-Shaped Gold Nanoparticles Coupled to a Metallic Film," *Langmuir*, vol. 30, no. 8, pp. 2297–2305, Mar. 2014.
- [204] P. Pallavicini, G. Chirico, M. Collini, G. Dacarro, A. Donà, L. D'Alfonso, A. Falqui, Y. Diaz-Fernandez, S. Freddi, B. Garofalo, A. Genovese, L. Sironi, and A. Taglietti, "Synthesis of branched Au nanoparticles with tunable near-infrared LSPR using a zwitterionic surfactant," *Chem. Commun.*, vol. 47, no. 4, pp. 1315–1317, 2011.
- [205] P. SK, "Observation of Optical Properties of Gold Thin Films Using Spectroscopic Ellipsometry," *J. Mater. Sci. Eng.*, vol. 5, no. 6, pp. 1–5, 2016.
- [206] E. Gizeli, F. Bender, A. Rasmusson, K. Saha, F. Josse, and R. Cernosek, "Sensitivity of the acoustic waveguide biosensor to protein binding as a function of the waveguide properties," *Biosens. Bioelectron.*, vol. 18, no. 11, pp. 1399–1406, Oct. 2003.
- [207] J. Chen, S. Shi, R. Su, W. Qi, R. Huang, M. Wang, L. Wang, and Z. He, "Optimization and Application of Reflective LSPR Optical Fiber Biosensors Based on Silver Nanoparticles," *Sensors*, vol. 15, no. 6, pp. 12205–12217, May 2015.

# Appendix

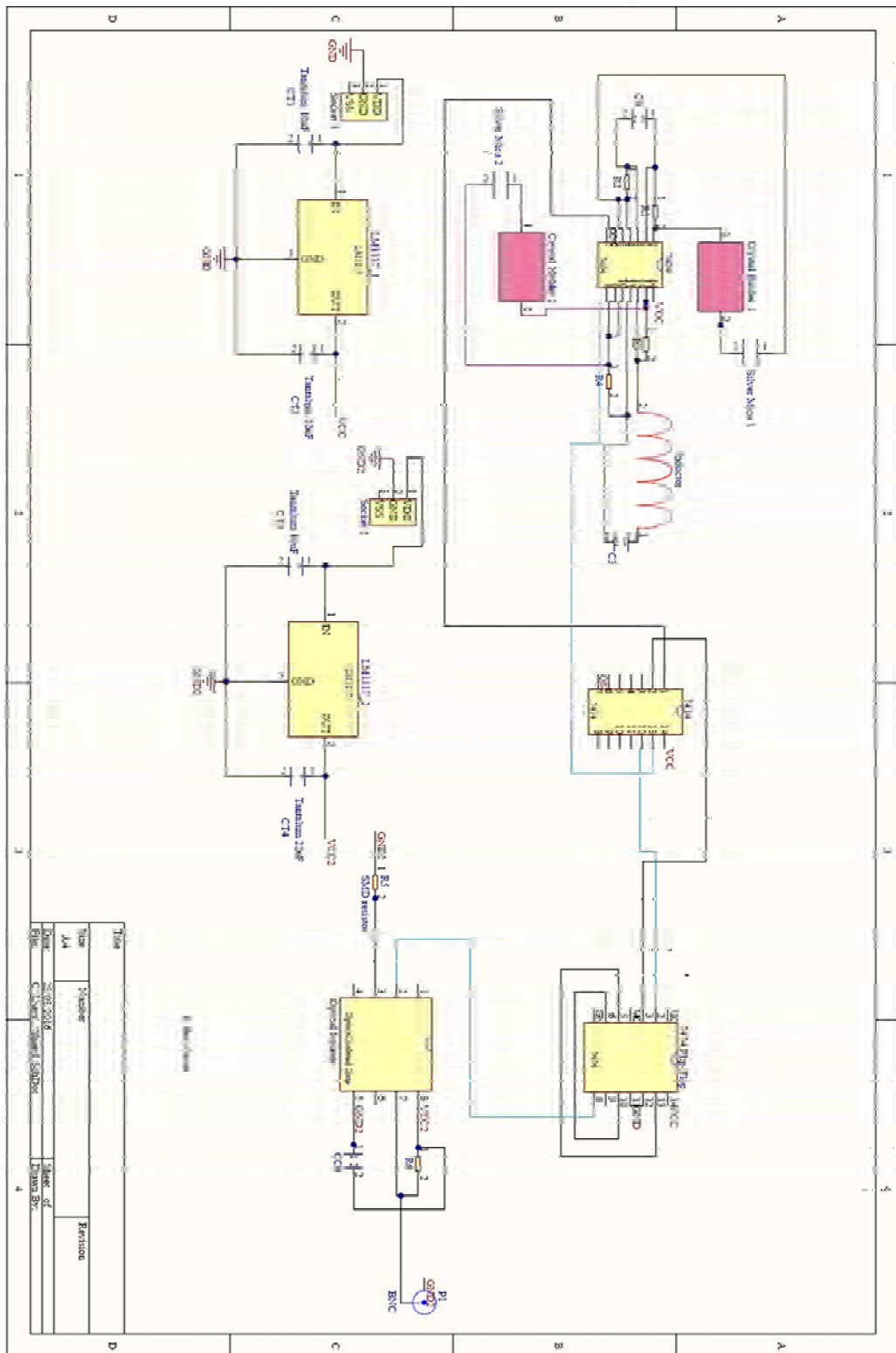


Figure A 1 Schematic of the PCB design

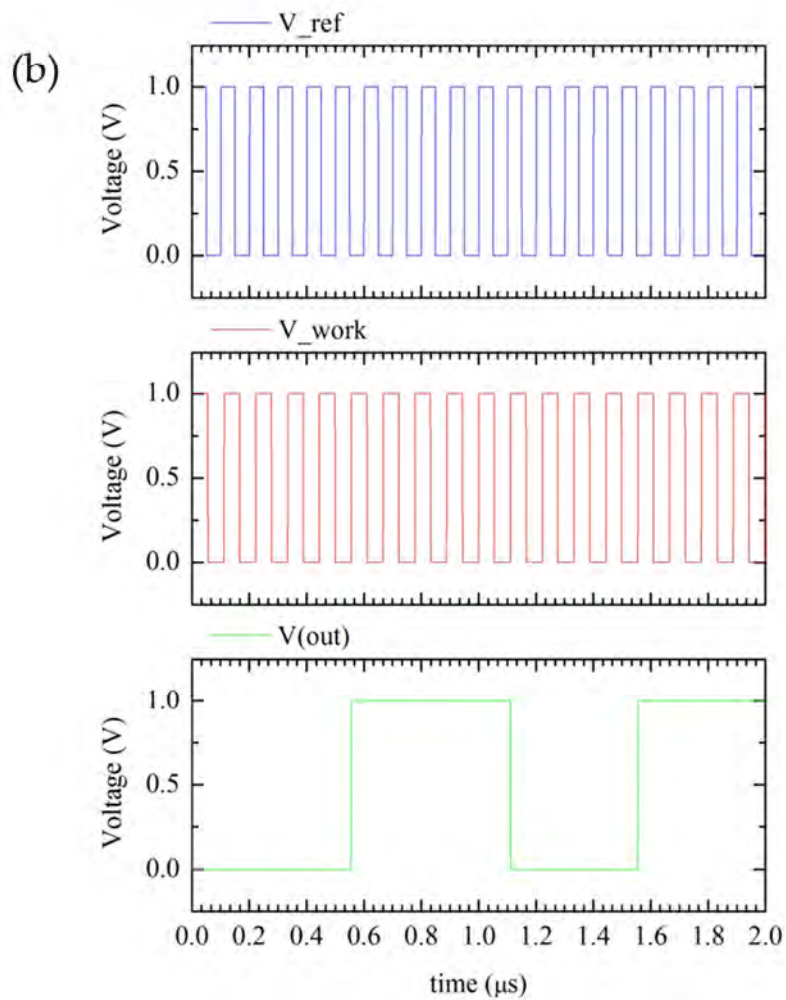
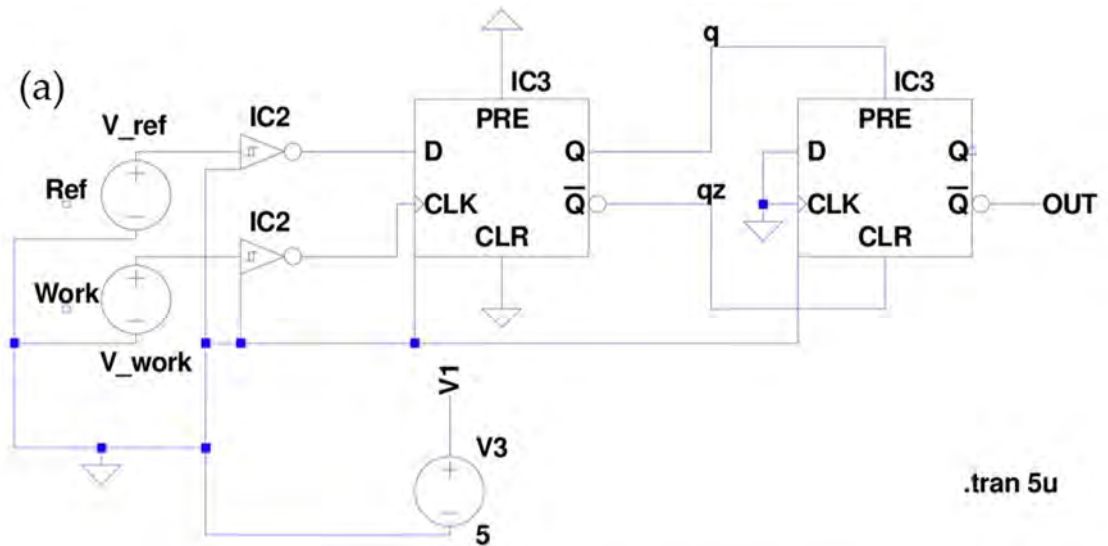


Figure A 2 (a) Circuit Schematic of the simulation of the frequency comparing circuit. Two QCMs have been replaced by two pulse voltage sources. (b) Simulation results.  $V_{ref}$  has a period of 100 ns and  $V_{work}$  has a period of 111 ns. The simulated  $V_{out}$  shows a period of 1  $\mu$ s.

Following is the script for running the orthogonal simulation which was described in Section 5.2.

```
run_sims=1;

# Do the 0 (P) degree polarization

switchtolayout;

setnamed("source1","polarization angle",0);

if (run_sims) {

    save("temp_0");

    run(1);

} else {

    load("temp_0");

}

T_0=transmission("transmission");

m="field";

x=getdata(m,"x");

z=getdata(m,"z");

E2_0=getelectric(m);

# Do the 90 (S) degree polarization

switchtolayout;

setnamed("source1","polarization angle",90);

if (run_sims) {

    save("temp_90");

    run(1);

} else {

    load("temp_90");
```

```

}

T_90=transmission("transmission");

m="field";

x=getdata(m,"x");

z=getdata(m,"z");

E2_90=getelectric(m);

# calculate the unpolarised transmission and field profile

T_unpol=0.5*(T_0+T_90);

E2_unpol=0.5*(E2_0+E2_90);

f = getdata("transmission","f");

lambda_1 = c/f;

lambda=lambda_1*1E9;

plot(lambda,T_unpol, "frequency (THz)","transmission");

legend("total","unpol");

# export data for excel import

filename = "0-coarsemesh.csv";

rm(filename); # delete if it already exists

for(i=1:length(lambda)) {

write(filename,num2str(lambda(i)) + "," + num2str(T_unpol(i)) + "," );

}

```